

# UC Merced

## UC Merced Electronic Theses and Dissertations

### Title

LINEAR AND NONLINEAR PROPERTIES OF MICROSTRUCTURE FIBERS AND THEIR APPLICATIONS IN PARAMETRIC DEVICES

### Permalink

<https://escholarship.org/uc/item/5zn5j7g1>

### Author

Sapkota, Deepak

### Publication Date

2021

Peer reviewed|Thesis/dissertation

UNIVERSITY OF CALIFORNIA, MERCED

LINEAR AND NONLINEAR PROPERTIES OF MICROSTRUCTURE FIBERS AND  
THEIR APPLICATIONS IN PARAMETRIC DEVICES

A dissertation submitted in partial fulfillment of the requirements  
for the degree Doctor of Philosophy

in

Materials and Biomaterials Science and Engineering

by

Deepak Sapkota

Committee in charge:

Professor Bin Liu, Chair

Professor Sarah Kurtz

Professor Venkatraman Ayyeswamy

2021

Copy right

Deepak Sapkota, 2021

Portions of Chapter 3 and 4 © 2021 Optics Express

Chapter 5 © 2014-2015 Leily Kaini, Thomson Lu

All rights reserved



Dedicated to

My late father Ek Narayan Sapkota, my mother Laxmi Devi Sapkota, my wife Seema A  
Sapkota, my daughter Ivana Sapkota, my parents-in-law (Badri Nath Adhikari and Sita  
Devi Adhikari) and Lord Shiva.

## ACKNOWLEDGEMENTS

At first, I would like to express my sincere gratitude to my graduate advisor, Professor Jay E. Sharping for providing me an opportunity to work in the field of nonlinear optics in his photonics laboratory. He was always supportive, and his valuable suggestions and guidance made it possible to achieve experimental success. He also sharpened my level of knowledge and understanding in generating new ideas and methods. I would also like to thank Professor Sarah Kurtz who always motivated me to be optimistic in life. I am also thankful to my dissertation committee members Prof. Bin Liu, Prof. Sarah Kurtz and Prof. Venkattraman Ayyeswamy for their constructive feedbacks and guidance during annual meetings in pursuing my degree.

I would like to show my appreciation to Leily Kaini and other who directly and indirectly offered me valuable suggestion and guidance. I am also grateful to Leily Kaini for her instructions and proper guidance for the experiments carried out in chapter 5. I am grateful to lab mates Alison Huff, Rodolfo Lopez, Jacob Pate, Nabin Raut, Jeffery Miller, Daniel Jonathan, Adrian Sanchez Magana, and Trevor Gammill who directly or indirectly helped me by offering their valuable advice and comments towards improving my research work. I would like to thank Prof. Ilan Boaz for his valuable feedback and Prof. Sayantani Ghosh for giving access to her lab to carry out some of my experiments. My sincere thank goes to Paul Robert, Director of Graduate Program, who helped me completing my PhD in time by offering right directions and suggestions throughout my PhD program. I would also like to thank my parents and parents-in-law for their love and motivation inspiring me to constantly focus on my research work. A special thank with due respect to my late father Ek Narayan Sapkota for his continuous support and inspiration throughout my life. I still remember his words and get motivated to do good and be good.

I would also like to thank School of Natural Sciences and School of Engineering for offering teaching assistantship throughout the program including the summer funding and travel grants to conference attendance.

Finally, and most importantly, I would like to thank with lots of love to my wife Seema Adhikari Sapkota for her understanding, supports and encouragement throughout my work. I would also convey my sincerest gratitude to her for her caring, her belief in me and my capacities and her strong support when I have downs in my PhD life. A special love and thank to my lovely daughter Ivana Sapkota for not disturbing me at home on my research during covid-19 pandemic.

**DEEPAK SAPKOTA**  
Merced, California  
(209) 261-7992 | dpksapkota1982@gmail.com

**PROFILE**

---

- Looking for an opportunity in the field of optics to utilize my research experiences and skills.
- Research experiences in fiber optics, fiber lasers, optical parametric oscillators and amplifiers, four wave mixing, Raman spectroscopy, quantum optics, linear optics and nonlinear optics.
- Extensive experience with pulsed laser ablation technique and thin film deposition.
- Effective team player with excellent written and communication skills.
- Self-driven, organized, curious, motivated and possess leadership capability.

**EDUCATION**

---

**PhD, Material and Biomaterial Science and Engineering** Expected Graduation: July 2021

University of California, Merced, California, USA

Cumulative GPA: 3.75

Research: Study of Linear and Nonlinear Properties of 3-Core Micro-Structure Fiber and Its Application in Parametric Devices.

**MS, Physics**

Graduation: May 2015

Department of Physics and Astronomy

University of Missouri, Kansas City, MO. USA

Cumulative GPA: 3.94

Research: Effect of applied electric fields on the laser ablation of tin and silicon in a liquid environment.

**MS, Physics**

Graduation: July 2007

Central Department of Physics

Tribhuvan University, Kathmandu, Nepal

**SKILLS**

---

- |   |                  |               |
|---|------------------|---------------|
| • Spectrometer  | • Laser          | • MATLAB      |
| • Pulsed laser ablation technique                         | • Fiber optics   | • LabView     |
| • Pulse characterization tools like auto-correlator, FROG | • Interferometry | • Mathematica |
|   | • Amplifier      | • COMSOL      |



- Optical parametric oscillator (OPO)
- Fiber OPO
- Experimental design
- Nano particle formation
- Igor Pro7
- Image J

## **EXPERIENCE**

---

### **Graduate Research Associate**

---

University of California, Merced August 2015-Present

- Created a single and multi-core fiber optic system for sample data acquisition to characterize the fiber.
- Characterized an optical multicore micro-structured fiber to study its linear and nonlinear properties.
- Demonstrated four wave mixing process in 3-core fiber and investigated its feasibility for parametric amplifiers and oscillators.
- Created a coherent light system and demonstrated high power measurement from a fiber optical parametric oscillator with co-developed polarization-based output coupling scheme.

University of Missouri, Kansas City August 2013-May 2015

- Utilized pulsed laser ablation technique in liquid environment to synthesis material's ablated nanoparticles and analyzed them using scanning electron microscope (SEM) and transmission electron microscope (TEM).
- Grown thin films of oxide materials on semiconductor wafer using pulsed laser deposition technology for nanoelectronics applications.

### **Graduate Teaching Associate**

---

University of California, Merced August 2015-Present

- Taught Physics and Mathematics and performed lab experiments for Undergraduates in the School of Natural Science for 6 years.

University of Missouri, Kansas City August 2013-July 2015

- Instructed lab experiments to Undergraduates as in the Department of Physics and Astronomy, UMKC for 2 years.

### **Other experiences**

- More than 10 years of experiences in teaching high school, college level and undergraduate level students in Nepal

## **Area of Interest**

---

- Quantum optics and optical devices
- Nonlinear fiber optics
- Fiber lasers and amplifiers
- Nano-material physics and nano-optics
- Material science
- Nano particles fabrication technique

## **Scholarships**

---

- Received the Material and Biomaterial Science and Engineering Summer Fellowship 2020 (and 2021) from School of Engineering, University of California Merced.
- Received the AY 2017-2018 Physics Graduate Student Summer Fellowship from School of Natural Science, University of California Merced.
- Received the James M. Phillips Scholarship award in recognition of high scholastic achievement in University of Missouri Kansas City, 2015.

## **Publications**

---

1. Deepak Sapkota, Yilu Li, Omar R. Musaev, Jerzy M Wrobel and Michael B Kruger, "Effect of electric fields on tin nanoparticles prepared by laser ablation in water", *Journal of laser applications*, Vol 29, No.1,2016
2. D. Sapkota and J. E. Sharping, "Four-wave mixing in a triple-core microstructure fiber," *Optics Express*, vol. 29, no. 9, pp. 13715-13721, 2021, doi: 10.1364/OE.421966.
3. Polarization-based Output Coupling Scheme for a Non-PM Microstructure Fiber Optical Parametric Oscillator (in progress)
4. Fiber Optical Parametric Oscillator using triple core microstructure fiber (in progress)

## **Conferences and Presentations:**

---

1. Deepak Sapkota, Thomson Lu and Jay Sharping, 'Single-core and dual-core fiber optical parametric oscillator', poster presented at the November 2017 APS Far West Section Annual Meeting, University of California Merced, California.
2. Attended CLEO conference, 2018 and 2020
3. Featured speaker at Optics and Laser 2021 conference on 'Four wave mixing in a triple core microstructure fiber for parametric devices', June 28-30, 2021.

**References:**

---

1. Sharping, Jay E., Professor, UC Merced, CA. (e-mail: jsharping@ucmerced.edu )
2. Kurtz, Sarah, Professor, UC Merced, CA (email: skurtz@ucmerced.edu)
3. Kruger, Michael, Professor and Dean of College of Science and Engineering, Texas Christian University (e-mail: michael.kruger@tcu.edu )
4. Bin Liu, Professor, UC Merced, CA (email: bliu27@ucmerced.edu)

# LINEAR AND NONLINEAR PROPERTIES OF MICROSTRUCTURE FIBERS AND THEIR APPLICATIONS IN PARAMETRIC DEVICES

Deepak Sapkota, Candidate for the Doctor of Philosophy Degree

University of California, Merced 2021

## ABSTRACT

Multicore microstructure fibers have emerged as promising components in ultrahigh capacity transmissions, biomedical imaging, quantum computing and signal-processing applications like wavelength conversion, and optical amplification. For long-haul transmission they are attractive due to low differential group delay [1] and nonlinear impairment reduction depending on the number of cores [2]. In this thesis we explore the linear-optical and nonlinear-optical properties of single and triple-core microstructure fibers with the goal of using them in parametric devices based on the four-wave mixing (FWM) nonlinearity. Although the presence of multiple cores in a fiber produces drawbacks as well as advantages, we experimentally demonstrate that FWM and parametric oscillation are possible in multicore microstructure fibers. One such advantage is the ability to increase the power conversion efficiency of a fiber optical parametric oscillator (FOPO). We also present results for a FOPO built using a single-core microstructure fiber and demonstrate a higher power extraction using a polarization-based output coupling method compared with a polarization-independent method.

We discuss measurements of the group velocity dispersion over a wavelength range from 1064-1600 nm. We study the mode coupling among the cores as a function of input power, polarization, wavelength, and spectral broadening. We demonstrate FWM in a triple core microstructure fiber at 1064 nm and study the transition between the case where FWM happens primarily in a single core and the case where FWM is distributed among multiple cores. We find that the effective nonlinear coefficient is reduced by a factor of 3 (the number of cores) when the coupling length is short compared with the nonlinear length, and that this leads to a three-fold reduction in the FWM bandwidth.

# TABLE OF CONTENTS

	Page
ACKNOWLEDGEMENTS .....	v
CURRICULUM VITAE.....	vii
ABSTRACTS .....	xi
TABLE OF CONTENTS.....	xii
LIST OF FIGURES .....	xv
LIST OF TABLES .....	xix
CHAPTER	
1. INTRODUCTION.....	1
1.1 Fiber optics.....	1
1.1.1 History of fiber optics .....	2
1.1.2 Fabrication of optical glass fiber.....	4
1.2 Optical parametric devices.....	8
1.3 Motivation and objective of the dissertation.....	9
1.4 Summary of dissertation .....	9
2. OPTICAL WAVEGUIDES .....	11
2.1 Step-index fiber.....	12
2.2 Maxwell's equations of wave propagation .....	13
2.3 Optical modes of cylindrical fiber .....	18
2.4 Multicore photonic crystal fiber.....	22
2.5 Modes in 3-core fiber.....	24
3. LINEAR PROPERTIES OF A TRIPLE CORE FIBER.....	26

3.1 Chromatic dispersion .....	26
3.1.1 Numerical aperture measurement .....	30
3.1.2 Dispersion measurement.....	32
3.2 Coupling between waveguides .....	35
3.2.1 Mode coupling in a triple core fiber .....	35
3.2.2 Mode coupling as a function of low power .....	37
3.2.3 Mode coupling as a function of wavelength .....	39
3.2.4 Mode coupling as a function of polarization .....	41
3.3 Coupling coefficient and coupling length.....	42
3.4 Coupling induced dispersion.....	45
3.5 Summary .....	46
4. NONLINEAR PROPERTIES OF A TRIPLE CORE FIBER .....	48
4.1 Origin of nonlinear effects .....	48
4.2 Self-phase modulation parameter .....	50
4.2.1 Determination of SPM value .....	50
4.3 Nonlinear effect for different fiber lengths .....	51
4.4 Mode coupling as a function of high power .....	54
4.5 Estimation of fiber parameters from FWM curve .....	57
4.6 Summary .....	62
5. OPTICAL PARAMETRIC OSCILLATOR USING NON-POLARIZATION MAINTAINING MICROSTRUCTURE FIBER.....	63
5.1 Historical review of FOPO .....	63
5.2 Four wave mixing process .....	64

5.3	Polarization in a birefringence fiber .....	65
5.4	Polarization-based scheme for FOPO .....	67
5.4.1	Experimental set-up .....	67
5.4.2	Result and discussion .....	68
5.5	Measurement of polarization state of fields in the FOPO cavity .....	71
5.6	Degree of polarization as a function of wavelength .....	74
5.7	Summary .....	75
6.	OPTICAL PARAMETRIC OSCILLATOR USING A TRIPLE CORE FIBER .....	77
6.1	Modified coupled mode theory .....	77
6.2	Degenerate four wave mixing in 3-core fiber .....	82
6.3	Polarization dependence of FWM gain .....	84
6.4	Three-core fiber optical parametric oscillator .....	86
6.5	Summary .....	89
7.	FUTURE DIRECTIONS .....	91
	BIBLIOGRAPHY .....	95

## LIST OF FIGURES

Figure	Page
1.1 (a) Cross-section view of an optic fiber (b) Light ray guided in fiber by total internal reflection occurring at the core-cladding interface when $n_1 > n_2$ .....	2
1.2 Timeline of the discoveries in the fiber optics in the golden era 1960-2000.....	4
1.3 MCVD process for the production of Ge-doped silica fiber preform.....	6
1.4 Fabrication method for photonic crystal fiber .....	6
1.5 Fiber drawing and jacket coating for photonic crystal fiber .....	7
1.6 Optical parametric devices. (a, d) generators (b, e) oscillators (c, f) amplifiers.....	8
2.1 Optical waveguides with different structures (a) planar (b) channel.....	11
2.2 Light ray guided in fiber by total internal reflection occurring at core-cladding interface .....	12
2.3 Plots of first three orders of Bessel functions of first (Fig. a) and modified second kinds (Fig. b).....	19
2.4 Three core fiber with cores in linear configuration (a) cross-section view (b) lengthwise view .....	23
2.5 SEM images of a 3-core microstructure fiber (a) a close-up of the linear arrangement of solid cores (b) hexagonal shape of the air-holes in triangular lattice configuration in the cladding region .....	24
2.6 Mode coupling between three waveguides .....	24
2.7 Fundamental modes in a 3-core optical fiber.....	25
3.1 Total dispersion of a triple core fiber.....	30
3.2 Plot of the beam radius as a function of propagating distance .....	31
3.3 Experimental set-up for the measurement of the fiber dispersion .....	32
3.4 Oscilloscope traces for the measurement of the time delay of the pulses .....	33
3.5 (a) Time delay measurement of individual cores of a 3-core fiber (b) for one	



of the side cores over a large range of wavelength .....	34
3.6 (a) Cross-section of a fiber with 3-cores of diameter 3.9 $\mu\text{m}$ in linear configuration arranged in a triangular lattice of air holes with a diameter of 1.08 $\mu\text{m}$ . (b) Intensity distribution for a long (52 m) piece where coupling among the cores is evident. (c) Intensity distribution for a short (35 cm) piece of fiber illuminated with 1064 nm light from an 8-ps pulsed laser. (d) A general structure of a 3-core showing different coupling coefficient between cores 1-2 and 2-3 .....	37
3.7 Experimental setup for the power measurement for individual cores .....	37
3.8 Measurement of the relative output across each core at low power when light is launched in (a) side core (b) central core (c) another side core .....	39
3.9 Normalized output power measurement as a function of wavelength across each core when each core is individually excited.....	40
3.10 Total output power measured as a function of wavelength when individual core is excited .....	41
3.11 Measurement of polarization dependance of mode-coupling in a fiber (a) change in the output power in each core as a function of half-wave plate angle when a constant input light was launched into core 2. (b) Total output power measurement at the fiber output end as a function of HWP angle at different input power. ....	42
3.12 Numerical calculation of the coupling coefficient value. ....	44
3.13 Numerical calculation of the coupling length for the side-core and central-core of a 3-core optical fiber.....	45
3.14 Numerical calculation of the coupling coefficient induced dispersion.....	46
4.1 Spectra showing self-phase modulation.....	51
4.2 Spectra showing pulse broadening at various high power for different fiber lengths.....	52
4.3 Spectra showing pulse broadening at a wavelength near 1120 nm. ....	53
4.4 Spectra showing pulse broadening at wavelength near 1460 and 1510 nm .....	54
4.5 Transfer of energy among cores in a 3-core fiber at intermediate power when light is launched into (a) side core (b) central core (c) another side core.....	55

4.6	Transfer of energy among cores at high power up to 650 W of peak power when light is launched into (a) side core (b) central core (c) another side core .....	57
4.7	FWM gain in short and long fiber lengths .....	58
4.8	Spectral broadening measurement as a function of input power when central core is excited .....	60
4.9	Spectral broadening measurement as a function of power for long and short fiber pieces showing the data range for finding spectral width and slope.....	61
5.1	Generation of two new frequencies in a degenerate FWM process from a pump Frequency. (a) FWM process (b) Energy level diagram (c) Phase matching diagram .....	65
5.2	Evolution of the polarization state of light along a uniform birefringence fiber for a linearly polarized light at $45^0$ with the slow axis. ....	66
5.3	Schematic of experimental set-up of a polarization-based schemed output power measurement from a FOPO system .....	68
5.4	Measurement of output power in the FOPO cavity as a function of HWP angle (a) for low loss case (b) for high power case. ....	69
5.5	Measurement of output power as a function of output coupler reflectivity in the cavity for low-loss and high-power conditions.....	70
5.6	Poincare spheres visualizing the polarization states of the fields in the cavity for linearly polarized input at two cases .....	72
5.7	Poincare spheres depicting the polarization states of the pump, idler, and signal when input is elliptically polarized for two cases .....	74
5.8	Measurement of the DOP of the fields in the low loss condition when the feedback mode is oscillating (a) idler wave (b) signal wave. ....	75
6.1	Parametric gain curve as a fuction of linear phase mismatch ( $\Delta\beta$ ) at $\gamma = 14 W^{-1}km^{-1}$ and $P_p = 100W$ (a) For gain coefficient $g_1$ , $g_2$ and $g_3$ at coupling coefficient $\kappa = \frac{1}{m}$ , (b) for the gain coefficient $g_3$ at different value of coupling coefficient $\kappa \left(\frac{1}{m}\right)$ .....	81
6.2	Parametric signal gain at various values of linear coupling coefficient at $\gamma = 14 W^{-1}km^{-1}$ and $P_p = 220W$ .....	81

6.3 Schematic of degenerate FWM process and experimentally observed FWM in 3-core fiber when central core is excited .....	83
6.4 FWM in all cores when they are individually excited .....	84
6.5 FWM gain spectra including pump when polarizing angle is changed at the input ...	86
6.6 Schematic of experimental setup for the triple core FOPO .....	87
6.7 Longer sideband power measurement when the input is at C2 .....	88
6.8 Longer sideband power measurement when light is launched at core C3 and the light is fed back into the same core.....	88
6.9 Longer sideband power measurement when light is launched at core C2 and the light is fed back in the cavity in (a) C3 (b) C2 (c) C1 .....	89
7.1 Schematic of experimental setup of 3-core FOPO with different arrangements For inter-mode coupling in the optical cavity.....	92
7.2 Schematic of the counting of photons generated by the SFWM in an optical fiber ..	93

## LIST OF TABLES

Table	page
2.1 Some linearly polarized modes and their formation .....	22
2.2 Fiber specification.....	24
3.1 Measurement of beam radius and calculation of NA.....	31
4.1 Value of SPM parameter.....	61

# CHAPTER 1

## INTRODUCTION

With the evolution of humans, people hunger for new inventions and discoveries to improve their lives. In different eras, people developed new technologies and novel devices for improving transportation, communication, health, etc. to improve their way of living based on their needs. In the past several decades, researchers and laser scientists have diversified their interests into many fields like medicine, biology, industry, and communication. One of the growing sectors in the 21<sup>st</sup> century is laser and fiber optics technology. The high power from the laser invented in 1960 enabled the study of the field of nonlinear optics [3]. Lasers are now being used in curing disease, welding, etching, cutting, printing, and various other fields [4]. In the communication and internet fields, optical fiber is a boon for the ultra-fast speed of signal transfer and ultra-high capacity of the system. Fiber optics is remarkably attractive in telecommunication for its relatively low attenuation at wavelengths around 1550 nm [5]. Moreover, fibers have gained attention in amplifiers like Raman amplifiers and optical parametric amplifiers. The fiber optical parametric amplification works based on a third-order nonlinear phenomenon called the four-wave mixing. The detail on the parametric amplification using fiber and the different processes that occur during this phenomenon is discussed in detail in chapter 5 and 6. Fiber optical parametric amplification (FOPA) has promising applications in wavelength conversion, nonlinear microscopy, quantum optics, and as a pump source for mid-infrared lasers [6, 7]. In this chapter, I will briefly describe the outlook of optical fiber technology and summarize the fiber manufacturing process. The history of discoveries and development of fiber technologies is summarized in section 1.1. Subsection 1.1.2 is the general short overview of the fabrication method of an optical glass standard fiber and a photonic crystal fiber. I give the fundamentals of optical parametric devices in section 1.2. The motivation behind my research work and the objective of this thesis are summarized in 1.3. Finally, section 1.4 summarizes the chapters of this dissertation.

### 1.1 Fiber optics

An optical fiber is a hair-like thin cylindrical dielectric waveguide to transmit light along its length. It consists of a transparent core embedded in a cladding and a jacket. The refractive index of the core region is slightly higher than that of the cladding region. The

light is guided in the core region by the total internal reflection which is an optical phenomenon that occurs when a light in the denser medium is incident with an angle greater than the critical angle. A general structure of optic fiber and a ray diagram for the guided light in the fiber are shown in figure 1.1.

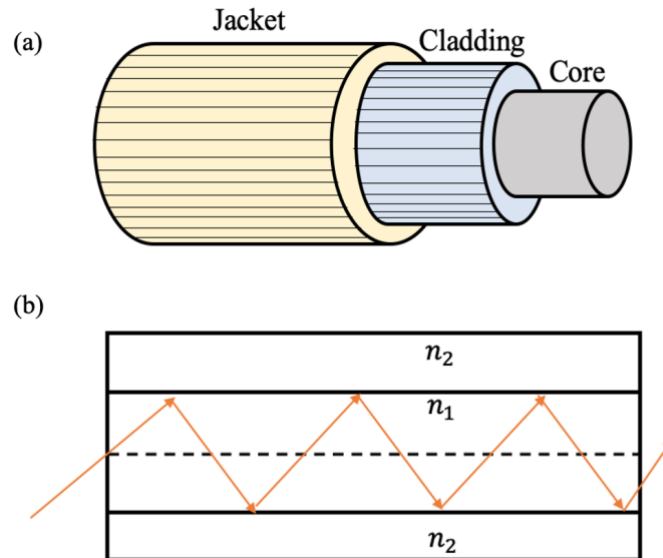


Fig. 1.1. (a) Cross-section view of an optic fiber (b) Light ray guided in fiber by total internal reflection occurring at the core-cladding interface when  $n_1 > n_2$ .  $n_1$  and  $n_2$  are the refractive indices of the core and cladding materials respectively.

A higher core refractive index can be achieved either by selecting suitable dopants like  $\text{GeO}_2$  for the core to increase the refractive index of the pure silica or the dopants like boron, fluorine, etc. for the cladding that decreases the refractive index of the cladding silica [8]. Depending on the refractive index of the core material, it can be sub-grouped into step-index and graded-index. Step-index fiber has the core region with a uniform refractive index, while the graded-index fiber has the core region with a refractive index gradually decreasing from the center to the core-cladding boundary.

### 1.1.1 History of fiber optics

Over the past few centuries, research in the photonics field transferred the means of communication from conventional methods to advanced technologies. The chronological inventions of newspaper (1641), typewriter (1714), telegraph (1837), fax machine (1843), telephone (1876), radio (1901), television (1926), computer (1937), transistor (1947), and

laser (1960) revolutionize the technology progress and further lead to the inventions of optical fiber and ethernet technology as the backbone of modern technology [9]. The demonstration of light guided along with a jet of water by Daniel Colladon in 1841 anticipated the concept of fiber optics [10]. Meanwhile, Jacques Babinet extended the principle to guiding light along bent glass rods [10]. However, at their time, the glass technology had limits and was not used for guiding light. It was in 1930 that Heinrich Lamm transmitted an image of a light bulb filament through a bundle of optic fibers [11]. Modern fiber optic technology grew rapidly through the research and development done in the past. Theodore Maiman invented the first laser using a synthetic pink ruby crystal in 1960 [12]. The same year, He-Ne laser was demonstrated [13]. The high power from the laser enabled the study of the nonlinear optics field and its effect on the light transmission in glass fiber. Eleas Snitzer theoretically described fibers supporting a single mode in a small core fiber in 1961 exhibiting high losses for communication applications [3]. Charles Kao and George Hockham of Standard Communication Laboratories in England in 1964, theoretically demonstrated that the loss in fiber can be reduced by removing impurities [14]. For this ground-breaking achievement in the transmission of light in fiber for optical communication, Charles Kao was awarded the Nobel prize in Physics in 2009. In 1970, F.P. Kapron et al. at Corning Glass Works reduced the attenuation losses in a single-mode fiber to less than 20 dB/km measured at a 632.8 nm wavelength [15]. This was achieved by doping fused silica glass with titanium. Two years later, they fabricated a germanium dioxide-doped silica fiber with an attenuation loss of only 4 dB/km. Further improvement in the fabrication process and more purity of the fused silica glass improved the performance of optical fiber in achieving low-attenuation and high bandwidths. Bell Laboratories developed a modified chemical vapor deposition process for the mass production of fiber optics in 1974 [9] and is still considered a standard process for fiber cabling manufacturing. In the 1980s, telephone companies started using fiber optics extensively in the communication field. Semiconductor InGaAsP lasers developed in the early 1980s were used to demonstrate the fiber loss below 1 dB/km at 1300 nm. However, the long-distance transmission became possible when low fiber attenuation (0.2 dB/km) was identified at wavelengths near 1550 nm using a single-mode semiconductor laser [16]. Long-distance communication became inexpensive only after the development of an erbium-doped fiber amplifier by David Payne and Emmanuel Desurvire in 1987 [17]. In 1991, the concept of photonic crystal fiber was proposed, which guided light by diffraction from a periodic structure [18] and it was first fabricated in 1996. The golden age for the development of the optical fiber and its accessories is considered the period of 1960-2000 [8, 17, 19-26]. The timeline of the development of optical fiber and discoveries of its associates before 2000 is mentioned below.

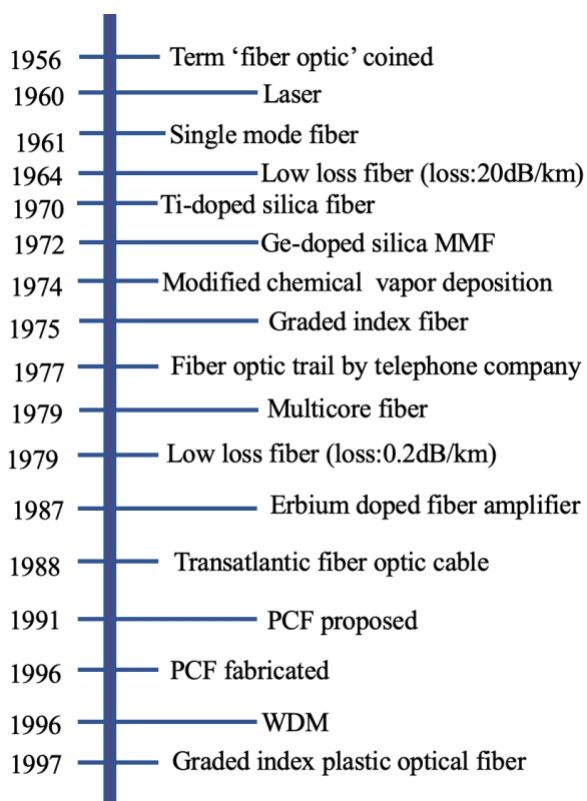
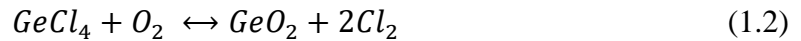
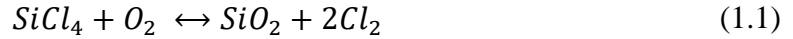


Fig. 1.2: Timeline of the discoveries in the optic fiber field in the golden era 1960-2000.

### 1.1.2 Fabrication of optical glass fiber

Mostly, optical fibers are made up of material like fused silica ( $SiO_2$ ). In a conventional optical fiber, the refractive index difference between core and cladding is made by doping some materials like Germanium ( $GeO_2$ ) or alumina ( $Al_2O_3$ ) in the core to increase the core refractive index. Dopants like boron oxide ( $Be_2O_3$ ) or fluorine are added to the cladding to lower the refractive index during the fabrication process. But the photonic crystal fibers are usually made up of single material like fused silica glass with micro-structured cladding. The optical fiber fabrication process generally involves two main stages, preform fabrication, and fiber drawing [8]. The first stage involves the production of the cylindrical preform with desired index profile and core-cladding dimensions. The production of the preform is commonly done with the modified chemical vapor deposition (MCVD) method as shown in Fig. 1.3 for step-index and graded-index fibers. In the process, the fused silica is obtained from the oxidation of  $SiCl_4$  at a temperature of 1800 K. For a Ge-doped silica preform, the formation of  $GeO_2$  is similar. The vapor phase reactions are





A pure silica tube is placed in a lathe and is rotated along the length. The gas flows through the tube forming soot which deposits on the inside of the silica tube. The burner transverses along outside of the tube. It is also moved back and forth across the tube length for the uniformity of the layer deposition. When the necessary layers are built up, more heat is added to the tube to collapse it into a solid rod called preform. It can be around 40-60 cm in length. It is then drawn into a fiber. It can be regarded as a large-scale optical fiber that has the same index profile and core-cladding dimension as the drawn optical fiber. Special care is taken during preform design for any contaminations in the lattice that may significantly increase the transmission loss. The MCVD method cannot be applied for the photonic crystal fibers as their preforms contain small holes throughout.

For the fabrication of multicore and micro-structured fiber, the stack and draw fiber technique is most widely used [27]. In this method, silica capillaries or rods are stacked and fused together into a macrostructure called multi-rod preform, as shown in Fig. 1.4, which is then slowly pulled through a high-temperature furnace (700-900°C) until desired structure and dimensions are achieved using a fiber drawing tower. The stacking is done in a definite lattice such as hexagonal and square and is thermally integrated preserving its shape over the whole length. Cores are created by removing one or more glass capillaries with glass rods. The fiber parameters such as airhole diameter, core diameter and hole-to-hole spacing (lattice constant) can be altered by varying the furnace temperature, preform feeding rate and the drawing speed.

The second stage is the drawing process performed on a draw tower. The preform is put in a draw furnace at the top of the tower. The tip of the preform is heated to melt and is continuously drawn using a precision feed mechanism as shown in Fig. 1.5. The preform is drawn down to the standard diameter of 125 microns producing many kilometers of fiber. The drawing process is similar for conventional fiber and photonic crystal fiber. A detailed fiber fabrication procedure has been described in [27, 28].

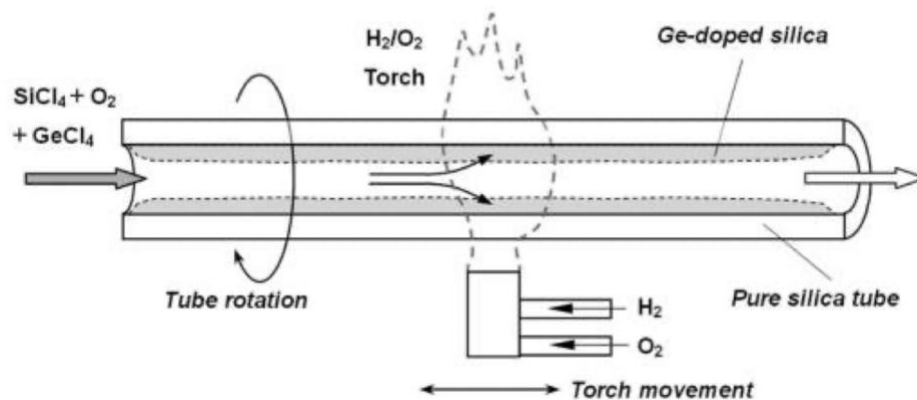


Fig. 1.3. MCVD process for the production of Ge-doped silica fiber preform. Reprinted from [29] with permission.

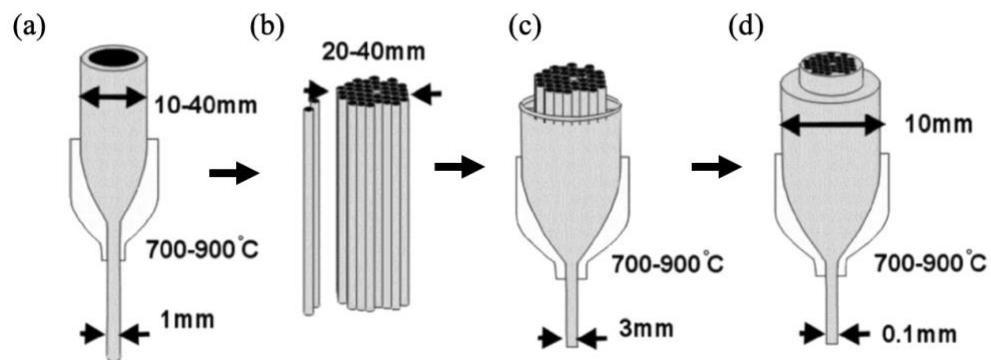


Fig. 1.4: Fabrication method for photonic crystal fiber. (a) individual glass capillary or rod formation (b) stacking of capillaries or glass rods for preform formation (c) drawing of the preform (d) final fiber drawing to the desired structure. [27]

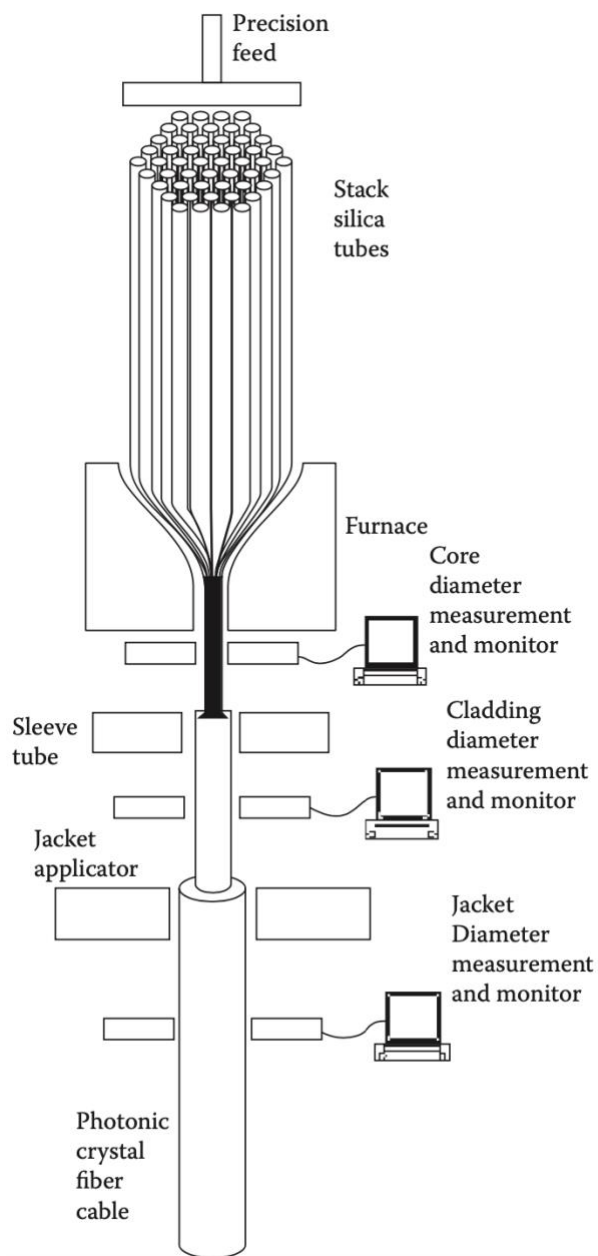


Fig. 1.5. Fiber drawing and jacket coating for a photonic crystal fiber. Reprinted from [30] with permission.

## 1.2 Optical parametric devices

A nonlinear medium pumped by an intense laser beam yields coherent light when certain conditions are met. Such a device is called an optical parametric device. With the advent of the laser, it was possible to send intense light through a nonlinear crystal in 1961 leading to second harmonic generation [31]. The demonstration of optical parametric devices leads to the generation of coherent tunable light in the visible and infrared regions. Research and development stimulated after the first demonstration established optical parametric generation as a promising tool for providing intense and robust pulses from nanoseconds to femtoseconds in duration in mode-locked operation. Similarly, optical parametric generation can also offer a single wavelength and continuous wave operation with excellent spatial and temporal beam properties. However, the performance of the optical parametric device depends on the quality of the pumping source and nonlinear materials being used [32]. Below are some of the parametric devices using 2<sup>nd</sup> order nonlinearity (such as crystal) and 3<sup>rd</sup> order nonlinearity (such as fiber).

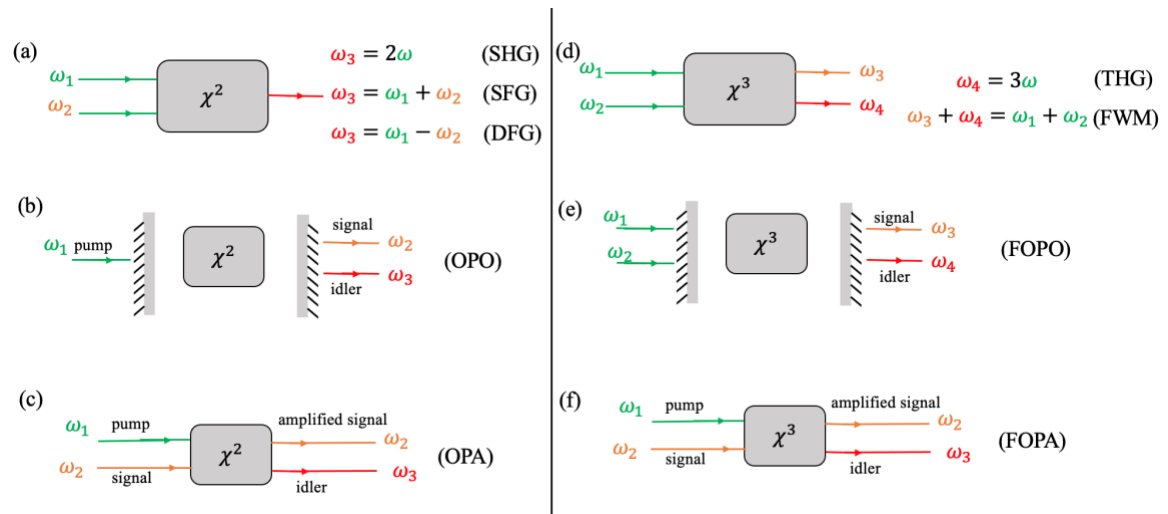


Fig. 1.6. Parametric devices. (a, d) generators (b, e) oscillators (c, f) amplifiers. SHG: Second Harmonic Generation, two identical photons combine to form new photons with twice the energy and half the wavelength of the initial photons.; SFG: Sum Frequency Generation, analogous to that of SHG, except that the two input photons are at different frequencies; DFG: Difference Frequency Generation, similar to SFG, but the frequency of the generated photons is the difference of those of the input photons; THG: Third Harmonic Generation, three identical photons combine to form new photons with thrice the energy of the initial photons; OPO: Optical Parametric Oscillator; FOPO: Fiber Optical Parametric Oscillator; OPA: Optical Parametric Amplifier; FOPA: Fiber Optical Parametric Amplifier. (a-c) and (d-f) are devices using 2<sup>nd</sup> order and 3<sup>rd</sup> order nonlinearity respectively.

### 1.3 Motivation and objective of the dissertation

In recent years, with the demands of high speed and high capacity optical systems, fibers with well-spaced multi-cores have emerged as an essential long-distance transmission medium for optical pulses [33]. Several recent research articles show that multicore fiber is emerging as a strong candidate for ultrahigh capacity transmission over a long-haul distance in future optical transmission systems [34–36]. The growing global demand of faster, secure, reliable and larger capacity of optical communication system and network motivated me to study the physics and applications of one new types of optical fiber, the multi-core microstructure fiber. Before implementing a fiber in practical use, it is crucial to understand how the signal gets affected when it propagates through the fiber. Moreover, Fiber optical parametric oscillator (FOPO) is a coherent source of light based on the four-wave mixing in optical fiber [4]. It is considered a promising alternative to solid-state lasers for its robustness and compactness. I am motivated to use a multicore fiber to develop a FOPO seeking an advantage of mode coupling on the output power.

The objective of this dissertation is to study the linear and nonlinear properties of a multicore fiber over a wide range of wavelengths that can be applied for a design of a parameter tailored fiber for its various applications including the fiber optical parametric oscillation. Moreover, we aim to investigate the role of mode coupling on the output power obtained from a FOPO under various conditions.

### 1.4 Summary of the dissertation

This dissertation mainly focuses on the various linear and nonlinear properties, including phase-matched four-wave mixing (FWM), in a 3-core micro-structure fiber for a wavelength of  $1.064 \mu m$ . This fiber's potential application in an optical parametric oscillator is also investigated. We also modeled a scheme based on the polarization of the fields to extract more coupled output power from a FOPO system. The remainder of this dissertation is organized in the following chapters.

Chapter 2 is the optical waveguide in which index guiding fiber is briefly discussed with Maxwell's equations that govern wave propagation in such fiber. This chapter consists of expressions of Maxwell's equation for the wave propagation in fiber in linear and nonlinear regimes. The optical modes of a cylindrical fiber are also discussed in detail. I introduce the multicore photonic crystal fiber and its novel features over a single core fiber with potential applications in different fields. Lastly, modes in a 3-core fiber are depicted using a coupled mode theory considering a small perturbation in fields in each core due to evanescent fields caused by the mode coupling.

Chapter 3 is the study of the linear properties of a 3-core microstructure fiber. I describe the chromatic dispersion in the fiber and discuss group velocity dispersion measurements

for our 3-core fiber along with their theoretical estimations over a wide range of wavelength 1100-1600 nm. I investigate mode coupling behavior in a multicore fiber as functions of wavelength, optical power, polarization of input light and spectral broadening establishing a clear understanding of their effects. At the same time, I also perform relevant numerical simulations to validate our experimental work. The study of mode coupling is crucial not only for the design of fibers but also for the signal transmission over a distance and for the construct of photonic devices like an optical switch, coupler, and sensors. I determine the coupling coefficient and coupling length.

Chapter 4 is the study of the nonlinear properties of a 3-core PCF. I observed the spectral broadening caused by the self-phase modulation (SPM) over a wide range of wavelengths. I discuss the origin of the nonlinear effect in the fiber and Kerr's nonlinearity mostly the SPM including its observance over a wavelength ranging from 1000-1600 nm. I also discuss the spectral broadening in different lengths of fiber over a wide range of input power. I observe a four-wave mixing at or near a wavelength of 1064 nm whose spectra are utilized to estimate the fiber's group velocity dispersion (GVD) and SPM parameter. These estimations are compared with the experimental measurements from chapters 3 and 4. The experimental observation of the four-wave mixing in the fiber is a milestone in building fiber optical parametric oscillator, which is a reliable source of coherent light.

Chapter 5 is the experimental study of the power measurement from a fiber optical parametric oscillator using a non-polarization maintaining microstructure fiber. A brief historical review of FOPO is presented at the beginning. A crucial phenomenon of wave mixing called FWM is also shortly described. A short description of polarization and its effect on pulse propagation through a birefringent fiber is included to understand its role for our fiber. I mention the previously performed experiment and the further research work I continue on the polarization-based scheme for the FOPO power extraction and discuss results based on the effect of polarization. I also explore the state of polarization of the fields in the cavity of the FOPO, and its experimental measurements.

Chapter 6 is the study of the application of a multicore fiber in fiber parametric devices. I develop a modified coupled mode theory for the pulse propagation in a 3-core fiber to try to understand how mode coupling impacts FOPO performance. The modified coupled mode theory applied to FWM in a 3-core fiber gives eigenvalues for the parametric gain coefficient for a FOPO. This comprehensive theory can be used to understand the coupling modes in fiber that affect the gain obtained from a multicore FOPO. The experimental observation of degenerate FWM is given. I also discuss the polarization dependence of FWM spectra in the 3-core fiber.

Chapter 7 is the discussion on the future directions of this work including the study of the modes in the oscillator's cavity at various ways of controlling modes, its potential applications in photon pair generation for quantum optics applications and in devising sensors.

## CHAPTER 2

### OPTIAL WAVEGUIDES

An optical waveguide is a dielectric cylindrical or planar structure to guide an electromagnetic wave along its longitudinal direction. Waveguides are classified into planar waveguides and channel waveguides. In a planar waveguide the core is sandwiched between cladding layers and the light is confined in only one transverse direction. The core is sometimes called the film while the upper and lower cladding layers are called the cover and the substrate. In a channel waveguide, such as an optical fiber, the core with a slightly higher refractive index is surrounded by the lower refractive index cladding region and the light is confined in two transverse directions. Figure 2.1 shows the core and cladding designs for the planar and channel waveguides. The light is guided in the core region by the total internal reflection which is an optical phenomenon that occurs when a light in the denser medium is incident with an angle greater than the critical angle. Higher core refractive index can be achieved either by selecting suitable dopants like  $\text{GeO}_2$  for the core to increase the refractive index of the pure silica or the dopants like boron, fluorine etc. for the cladding that decrease the refractive index of the cladding silica. Depending on the profile of the refractive index of the core material, the fibers can be sub-grouped into step index and graded index varieties. This chapter provides the fundamental background knowledge required to understand the concept of light propagation in an optical fiber. Section 2.1 describes the index guiding fiber. The propagation of an electromagnetic wave in an optical waveguide can be well understood by Maxwell's equations which are explained in section 2.2. Section 2.3 describes optical modes in fiber and section 2.4 contains multicore photonic crystal fiber.

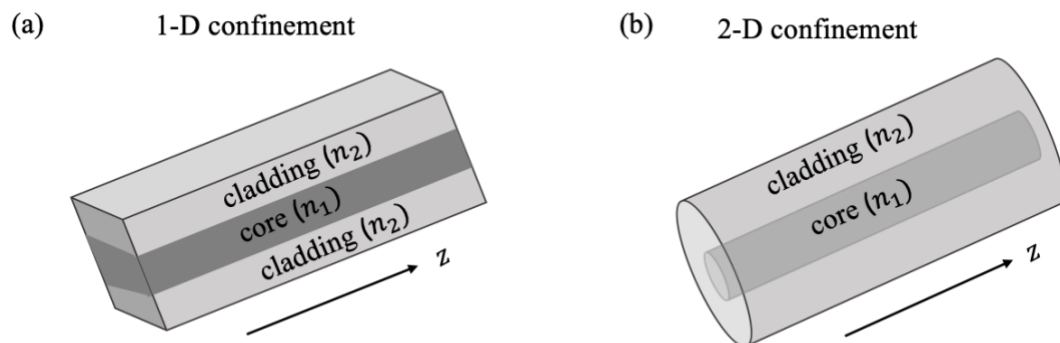


Fig. 2.1. Optical waveguides with different structures (a) planar (b) channel [37]

## 2.1 Step-index fiber

If the core of a fiber has constant refractive index, the fiber is called a step-index fiber. The refractive index profile  $n(r)$  is defined as

$$n(r) = \begin{cases} n_1 & \text{for } 0 \leq r \leq a \text{ (core region)} \\ n_2 & \text{for } r > a \text{ (cladding region)} \end{cases} \quad (2.1)$$

where  $a$  is the core radius. Light is confined in the core by the total internal reflection phenomenon at the core-cladding boundary for  $n_1 > n_2$ . The ray diagram for the guided light in the fiber is shown in figure 2.2 in which the total internal reflection occurs at the core-cladding interface when  $n_1 > n_2$ .

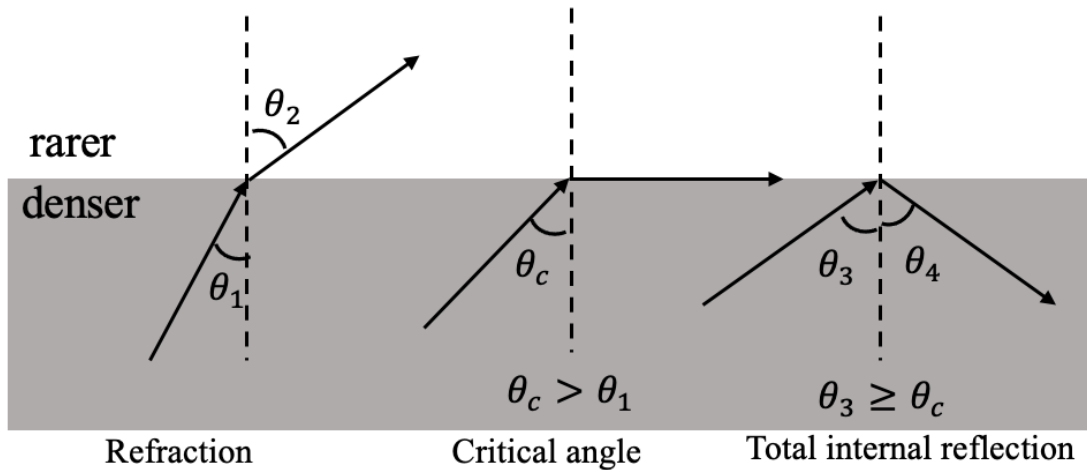


Fig. 2.2. Light ray guided in fiber by total internal reflection occurring at core-cladding interface.

A fiber is, in general, characterized by the relative core-cladding index difference and the dimensionless parameter V-number given by

$$\Delta = \frac{n_1 - n_2}{n_1} \quad (2.1a)$$

$$V = k_0 a \sqrt{n_1^2 - n_2^2} \quad (2.1b)$$

where  $k_0 = \frac{2\pi}{\lambda}$  and  $\lambda$  is the wavelength of the light in vacuum. Light propagates inside a fiber in the form of modes. The V-number determines the number of modes supported by a fiber. Based on the modes, a step index fiber can be categorized into single mode and



multimode step index fiber. If  $V < 2.405$ , a step index fiber supports only one mode and if  $V > 2.405$ , the fiber supports multiple modes. The core radius  $a$  is typically  $< 5 \mu\text{m}$  for single mode and  $> 25 \mu\text{m}$  for multimode fibers.

## 2.2 Maxwell's equation of wave propagation

In this section, the fundamental principles governing the propagation of light in an optical fiber are described. The propagation of fields in optical fibers is governed by well-known Maxwell's equations [8] which are expressed as

$$\nabla \cdot \mathbf{D} = \rho_f = 0 \quad (2.2)$$

$$\nabla \cdot \mathbf{B} = 0 \quad (2.3)$$

$$\nabla \times \mathbf{E} = -\frac{\partial \mathbf{B}}{\partial t} \quad (2.4)$$

$$\nabla \times \mathbf{H} = \mathbf{J} + \frac{\partial \mathbf{D}}{\partial t} = \frac{\partial \mathbf{D}}{\partial t} \quad (2.5)$$

where,  $\mathbf{D} = \varepsilon_0 \mathbf{E} + \mathbf{P}$  and  $\mathbf{B} = \mu_0 \mathbf{H}$ ,  $\varepsilon_0$  and  $\mu_0$  being the vacuum permittivity and permeability respectively and  $\mathbf{E}$ ,  $\mathbf{H}$ , and  $\mathbf{P}$  are the electric field, magnetic field and induced electric polarization respectively.  $\mathbf{J} = 0$  &  $\rho_f = 0$  for an optical fiber as there are no free charges present in it.

The curl of electric field vector in equation (2.4) can be written as

$$\nabla \times \nabla \times \mathbf{E} = -\frac{1}{c^2} \frac{\partial^2 \mathbf{E}}{\partial t^2} - \mu_0 \frac{\partial^2 \mathbf{P}}{\partial t^2} \quad (2.6)$$

where,  $c$  is the speed of light and  $\mu_0 \varepsilon_0 = 1/c^2$ . Using the cross-product rule, we may write

$$\nabla \times \nabla \times \mathbf{E} = \nabla(\nabla \cdot \mathbf{E}) - \nabla^2 \mathbf{E} = -\nabla^2 \mathbf{E}. \quad (2.7)$$

The total polarization  $\mathbf{P}(\mathbf{r}, t)$  induced by electric dipoles is given by

$$\mathbf{P}(\mathbf{r}, t) = \varepsilon_0 \sum_{i=1}^{\infty} \chi^i \mathbf{E}(\mathbf{r}, t)^i \quad (2.8)$$

where  $\chi^i$  are the tensors of rank  $(i+1)$  representing material susceptibility. For an optical fiber, the second-order nonlinearity is zero due to inversion symmetry and we include only

up to the third order nonlinearity governed by  $\chi^{(3)}$  ignoring higher order nonlinear effects. We express the induced polarization as a combination of linear and nonlinear part as

$$\mathbf{P}(\mathbf{r}, t) = \mathbf{P}_L(\mathbf{r}, t) + \mathbf{P}_{NL}(\mathbf{r}, t) \quad (2.10)$$

where,  $\mathbf{P}_L(\mathbf{r}, t) = \varepsilon_0 \chi^1 \cdot \mathbf{E}$  and  $\mathbf{P}_{NL}(\mathbf{r}, t) = \varepsilon_0 \chi^3 : \mathbf{E}\mathbf{E}\mathbf{E}$ .

Therefore, we get,

$$\nabla^2 \mathbf{E} - \frac{1}{c^2} \frac{\partial^2 \mathbf{E}}{\partial t^2} = \mu_0 \frac{\partial^2 \mathbf{P}_L}{\partial t^2} + \mu_0 \frac{\partial^2 \mathbf{P}_{NL}}{\partial t^2}. \quad (2.11)$$

This wave equation governs the light propagation in a medium. For a low-power light propagation,  $\mathbf{P}_{NL}$  is small and can be ignored. However, for a high-power light propagation, we must include the nonlinear induced polarization. The following two cases explore low-power linear propagation and high-power nonlinear propagation.

### Case I: Linear pulse propagation

To determine the solution of linear part, we ignore nonlinear effect in a silica fiber by setting  $\mathbf{P}_{NL}=0$ . We can rewrite equation (2.11) as

$$\nabla^2 \mathbf{E} - \frac{1}{c^2} \frac{\partial^2 \mathbf{E}}{\partial t^2} = \mu_0 \frac{\partial^2 \mathbf{P}_L}{\partial t^2}. \quad (2.12)$$

The equation 2.12 is linear in  $\mathbf{E}$ . We may express above equation in the form of the Helmholtz equation expressed in the frequency domain

$$\nabla^2 \mathbf{E} + n^2(\omega) \frac{\omega^2}{c^2} \mathbf{E} = 0. \quad (2.13)$$

Equation (2.13) is solved for the cylindrical symmetry of fibers in the section 2.3 to obtain the optical modes.

### Case II: Nonlinear pulse propagation

For short pulses ( $T_o < 10 \text{ ns}$ ) propagating through an optical fiber, the nonlinear effects cannot be ignored. Both group velocity dispersion (GVD) and fiber nonlinear response must be considered. Because of the complexity, several assumptions have been made to

simplify the equation. The induced nonlinear polarization is assumed as a small perturbation to the linear part of induced polarization as in equation (2.10). This is due to the fact that nonlinear induced polarization is much smaller than the linear induced polarization. Secondly, the field is assumed to be a slowly varying envelope and the dipole approximation is valid. The electric field can be written in the form

$$\mathbf{E}(\mathbf{r}, t) = \frac{1}{2} \hat{\mathbf{x}} \mathbf{E} e^{-i\omega_o t} + c. c. \quad (2.14)$$

where  $\hat{\mathbf{x}}$  is the polarization unit vector,  $E_x(\mathbf{r}, t)$  is the slowly varying field along  $x$  direction and  $\omega_o$  is the central frequency. The polarization components  $\mathbf{P}_L(\mathbf{r}, t)$  and  $\mathbf{P}_{NL}(\mathbf{r}, t)$  can also be expressed in the similar way as

$$\mathbf{P}_L(\mathbf{r}, t) = \frac{1}{2} \hat{\mathbf{x}} P_L(\mathbf{r}, t) e^{-i\omega_o t} + c. c. \quad (2.15)$$

$$\mathbf{P}_{NL}(\mathbf{r}, t) = \frac{1}{2} \hat{\mathbf{x}} P_{NL}(\mathbf{r}, t) e^{-i\omega_o t} + c. c. \quad (2.16)$$

The linear part can be expressed in the frequency domain. Therefore, we can write them in terms of material susceptibility as

$$\mathbf{P}_L(\mathbf{r}, t) = \varepsilon_0 \chi^1 \cdot \mathbf{E}(\mathbf{r}, t) = \frac{\varepsilon_0}{2\pi} \chi^1 \cdot \mathbf{E}(\mathbf{r}, \omega - \omega_o). \quad (2.17)$$

The nonlinear part is

$$\mathbf{P}_{NL}(\mathbf{r}, t) = \varepsilon_0 \chi^3 : \mathbf{E}(\mathbf{r}, t) \mathbf{E}(\mathbf{r}, t) \mathbf{E}(\mathbf{r}, t). \quad (2.18)$$

Substitution of equation (2.14) in equation (2.18) implies that  $\mathbf{P}_{NL}(\mathbf{r}, t)$  oscillates at  $\omega_o$  and  $3\omega_o$ . Oscillation at third harmonic frequency  $3\omega_o$  can be ignored as it rarely satisfies the phase-matching condition required for the significant contribution.

From equation 2.16 and 2.18, we may have

$$P_{NL}(\mathbf{r}, t) \approx \varepsilon_0 \varepsilon_{NL} E(\mathbf{r}, t) \quad (2.19)$$

where  $\varepsilon_{NL}$  is the nonlinear contribution to the dielectric constant and is defined by

$$\varepsilon_{NL} = \frac{3}{4} \chi_{xxxx}^3 |E(\mathbf{r}, t)|^2. \quad (2.20)$$

The Helmholtz equation in the frequency domain from equation (2.13) is rewritten as

$$\nabla^2 \tilde{\mathbf{E}} + n^2(\omega)k_o^2 \tilde{\mathbf{E}} = 0. \quad (2.21)$$

This equation can be solved by using the method of separation of variables. Assuming that the solution is of the form

$$\tilde{\mathbf{E}}(r, \varphi) = F(r)\tilde{A}(z, \omega - \omega_o)e^{im\varphi}e^{i\beta_o z} \quad (2.22)$$

where  $(r, \varphi, z)$  are the cylindrical coordinates,  $\tilde{A}(z, \omega)$  is the amplitude of the slowly varying field along  $z$  direction,  $\beta_o$  is the propagation constant and  $F(r)$  is the transverse distribution of the field which remains same for both polarization components.

Substituting equation (2.22) in equation (2.21), we obtain following two equations.

$$\frac{\partial^2 F}{\partial r^2} + \frac{1}{r} \frac{\partial F}{\partial r} + \left( k_o^2 n^2 - \tilde{\beta}^2 - \frac{m^2}{r^2} \right) F = 0 \quad (2.23)$$

$$\frac{\partial^2 \tilde{A}}{\partial z^2} + 2i\beta_o \frac{\partial \tilde{A}}{\partial z} + (\tilde{\beta}^2 - \beta_o^2) \tilde{A} = 0 \quad (2.24)$$

These equations can be further simplified in a similar way as done in section (2.3) to obtain eigenvalue equations, solution of which gives the value of  $\tilde{\beta}$ . Including the first order perturbation,  $\tilde{\beta}$  can be expressed as

$$\tilde{\beta}(\omega) = \beta(\omega) + \Delta\beta(\omega) \quad (2.25)$$

where, an expression for  $\Delta\beta(\omega)$  is defined by the first order perturbation theory as

$$\Delta\beta(\omega) = \frac{nk_o^2}{\beta(\omega)} \left[ \frac{\int \int_{-\infty}^{\infty} \Delta n(\omega) |F(x, y)|^2 dx dy}{\int \int_{-\infty}^{\infty} |F(x, y)|^2 dx dy} \right] \quad (2.26)$$

where,

$$\Delta n(\omega) = n_2 |E|^2 + \frac{i\alpha}{2k_o} \quad (2.27)$$

with  $n_2$  being the nonlinear coefficient,  $\alpha$  being the absorption coefficient (loss) and  $k_o = \frac{\omega_o}{c}$  is the wave vector. Using equations (2.26) and (2.27) in equation (2.25), we get

$$\Delta\beta(\omega) = \gamma |A|^2 + \frac{i\alpha}{2} \quad (2.28)$$

where,  $\gamma$  is the nonlinear coefficient of the optical fiber defined by

$$\gamma = \frac{n_2 k_o}{A_{eff}} \quad (2.29)$$

and the  $A_{eff}$  is the effective mode area given by

$$A_{eff} = \left[ \frac{(\int \int_{-\infty}^{\infty} |F(x, y)|^2 dx dy)^2}{\int \int_{-\infty}^{\infty} |F(x, y)|^4 dx dy} \right]. \quad (2.30)$$

Since  $\tilde{A}(z, \omega)$  is considered to be slowly varying field along  $z$  direction, the first term on the LHS of equation (2.24) can be ignored. Approximating  $\tilde{\beta}^2 - \beta_o^2$  as  $2\beta_o(\tilde{\beta} - \beta_o)$  and using equation (2.25) in equation (2.24), we get

$$\frac{\partial \tilde{A}}{\partial z} = i[\beta(\omega) + \Delta\beta(\omega) - \beta_o] \tilde{A} \quad (2.31)$$

This equation can be transformed back to the time domain by taking the inverse Fourier transform to obtain the propagation constant for the slowly varying field. The frequency dependence of  $\beta(\omega)$  and  $\Delta\beta(\omega)$  can be approximated by expanding them using Taylor series expansion around the carrier frequency  $\omega_o$ .

$$\beta(\omega) = \beta_o + (\omega - \omega_o)\beta_1 + \frac{1}{2}(\omega - \omega_o)^2\beta_2 + \dots \quad (2.32)$$

$$\Delta\beta(\omega) = \Delta\beta_o + (\omega - \omega_o)\Delta\beta_1 + \frac{1}{2}(\omega - \omega_o)^2\Delta\beta_2 + \dots \quad (2.33)$$

where,  $\beta_o = \beta(\omega_o)$  and higher orders are defined by  $\beta_m = \left( \frac{d^m \beta}{d\omega^m} \right)_{\omega=\omega_o} \cdot \Delta\beta_o$  and  $\Delta\beta_m$  can be defined in the similar way.

Equation (2.31) can be transformed to time domain by taking the inverse Fourier transform using

$$A(z, t) = \frac{1}{2\pi} \int_{-\infty}^{\infty} \tilde{A}(z, \omega - \omega_o) e^{-i(\omega - \omega_o)t} d\omega. \quad (2.34)$$

Therefore, we get

$$\frac{\partial A}{\partial z} + \beta_1 \frac{\partial A}{\partial t} + \frac{i\beta_2}{2} \frac{\partial^2 A}{\partial t^2} = i\Delta\beta_o A \quad (2.35)$$

Substituting the value of  $\Delta\beta_o$  from equation (2.28) in equation (2.35), we get

$$\frac{\partial A}{\partial z} + \beta_1 \frac{\partial A}{\partial t} + \frac{i\beta_2}{2} \frac{\partial^2 A}{\partial t^2} + \frac{\alpha}{2} A = i\gamma |A|^2 A \quad (2.36)$$

If we neglect the absorption loss coefficient, then the above equation takes the usual form of nonlinear Schrodinger equation which governs the propagation of a pulse in a nonlinear dispersive fiber. The higher order effects in both linear and nonlinear phenomena are ignored. The effects of stimulated inelastic scattering such as stimulated Raman scattering (SRS) and stimulated Brillouin scattering (SBS) are not included in above equation (2.36). However, above equation can be modified to include them depending on the experimental conditions.

### 2.3 Optical modes of cylindrical fiber

An optical fiber is a long cylindrical dielectric waveguide. For a light passing through such waveguide, we may represent the electric field and the magnetic field as

$$\mathbf{E} = E_o e^{i(\omega t - \beta z)} \text{ and } \mathbf{H} = H_o e^{i(\omega t - \beta z)}. \quad (2.41)$$

In cylindrical coordinate system, the Helmholtz equation in (2.13) can be written as

$$\frac{\partial^2 \mathbf{E}}{\partial r^2} + \frac{1}{r} \frac{\partial \mathbf{E}}{\partial r} + \frac{1}{r^2} \frac{\partial^2 \mathbf{E}}{\partial \varphi^2} + \frac{\partial^2 \mathbf{E}}{\partial z^2} + n^2 k_o^2 \mathbf{E} = 0. \quad (2.42)$$

where,  $\mathbf{E}$  is the electric field vector and  $\mathbf{k}_o = \frac{\omega}{c} = \frac{2\pi}{\lambda}$  is a wave vector.

We are interested in the solutions that take the form of wave traveling in z direction with a propagation constant  $\beta$ . To find the solution of equation (2.42) for the axial component of the field, we apply the method of separation of variable of the form [8]

$$E_z(r, \varphi) = A(\omega) R(r) e^{-im\varphi} e^{-i\beta z}. \quad (2.43)$$

We then get,

$$\frac{\partial^2 R}{\partial r^2} + \frac{1}{r} \frac{\partial R}{\partial r} + \left( k_o^2 n^2 - \beta^2 - \frac{m^2}{r^2} \right) R = 0 \quad (2.44)$$

where,  $m$  is an integer and  $n = n_1$  for  $r \leq a$  ( $a$  being fiber radius) and  $n = n_2$  for  $r \geq a$ . For a guided wave in a fiber, the propagation constant of each transverse mode must satisfy

$$k_o n_2 < \beta < k_o n_1 \quad (2.45)$$

Equation (2.44) is the second order differential equation whose solutions are the Bessel's function. The general solutions look like

$$\begin{aligned} R(r) &= CJ_m\left(\frac{ur}{a}\right) + DY_m\left(\frac{ur}{a}\right) \quad \text{for } r \leq a \\ &= FK_m\left(\frac{wr}{a}\right) + GI_m\left(\frac{wr}{a}\right) \quad \text{for } r > a \end{aligned} \quad (2.46)$$

where,  $J_m\left(\frac{ur}{a}\right)$ ,  $Y_m\left(\frac{ur}{a}\right)$  are the Bessel function of 1<sup>st</sup> and 2<sup>nd</sup> kind and  $I_m\left(\frac{wr}{a}\right)$ ,  $K_m\left(\frac{wr}{a}\right)$  are the modified Bessel's function of 1<sup>st</sup> and 2<sup>nd</sup> kind respectively.  $u = a(k_o^2 n_1^2 - \beta^2)^{\frac{1}{2}}$  is the and  $w = a(\beta^2 - k_o^2 n_1^2)^{\frac{1}{2}}$ .

In the core region of step index fiber, the solution is  $J_m\left(\frac{ur}{a}\right)$  (gradually damped oscillatory function w.r.t.  $r$ ).  $Y_m\left(\frac{ur}{a}\right)$  vanishes as  $\frac{r}{a} \rightarrow 0$  (shown in fig. 2.3 (a)). The field decays exponentially outside the core. In the cladding region, the solution is  $K_m\left(\frac{wr}{a}\right)$ , (modified function decays exponentially w.r.t.  $r$ ).  $I_m\left(\frac{wr}{a}\right)$  vanishes as  $\frac{r}{a} \rightarrow \infty$  (shown in fig. 2.3 (b)).

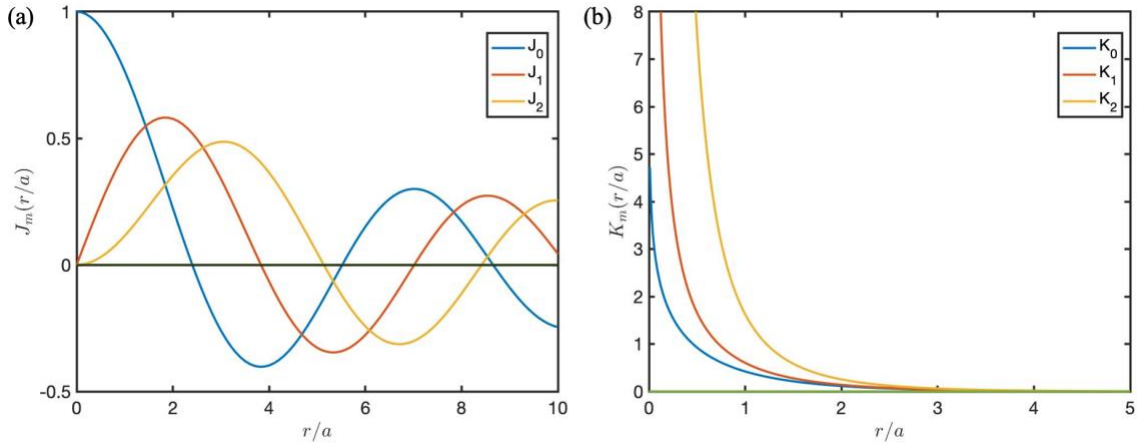


Fig. 2.3. Plots of first three orders of Bessel functions of (a) first and (b) modified second kinds.

Therefore,

$$R(r) \propto \begin{cases} J_m\left(\frac{ur}{a}\right), & r \leq a. \quad (\text{core}) \\ K_m\left(\frac{wr}{a}\right), & r > a \quad (\text{cladding}) \end{cases} \quad (2.47)$$

Plugging the value of  $R(r)$  from equation (2.47) in equation (2.43), we get

$$\begin{aligned} E_z(r, \varphi) &= A_1(\omega) J_m\left(\frac{ur}{a}\right) e^{-im\varphi} e^{-i\beta z} \quad \text{for } r \leq a \\ E_z(r, \varphi) &= A_2(\omega) K_m\left(\frac{wr}{a}\right) e^{-im\varphi} e^{-i\beta z} \quad \text{for } r > a. \end{aligned} \quad (2.48)$$

The expressions for the azimuthal solutions of electric field are

$$\begin{aligned} E_\varphi(r, \varphi) &= B_1(\omega) J_m\left(\frac{ur}{a}\right) \sin m\varphi \quad \text{for } r \leq a \\ E_\varphi(r, \varphi) &= B_2(\omega) K_m\left(\frac{wr}{a}\right) \sin m\varphi \quad \text{for } r > a. \end{aligned} \quad (2.49)$$

The equations for magnetic field component  $H_z$  and  $H_\varphi$  can be similarly found.

$$\begin{aligned} H_z(r, \varphi) &= C_1(\omega) J_m\left(\frac{ur}{a}\right) e^{-im\varphi} e^{-i\beta z} \quad \text{for } r \leq a \\ H_z(r, \varphi) &= C_2(\omega) K_m\left(\frac{wr}{a}\right) e^{-im\varphi} e^{-i\beta z} \quad \text{for } r > a \\ H_\varphi(r, \varphi) &= D_1(\omega) J_m\left(\frac{ur}{a}\right) \sin m\varphi \quad \text{for } r \leq a \\ H_\varphi(r, \varphi) &= D_2(\omega) K_m\left(\frac{wr}{a}\right) \sin m\varphi \quad \text{for } r > a \end{aligned} \quad (2.50)$$

The fields are continuous at the boundary between core and cladding, so applying the boundary conditions at the core-cladding interface,

$$\begin{aligned} E_z^{core}|_{r=a} &= E_z^{cladding}|_{r=a}; \quad n_1^2 E_z^{core}|_{r=a} = n_2^2 E_z^{cladding}|_{r=a} \\ E_\varphi^{core}|_{r=a} &= E_\varphi^{cladding}|_{r=a}; \end{aligned} \quad (2.51)$$

We arrive at

$$\begin{aligned} \left[ \frac{J'_m(u)}{uJ_m(u)} + \frac{K'_m(w)}{wK_m(w)} \right] & \left[ \frac{n_1^2 J'_m(u)}{n_2^2 uJ_m(u)} + \frac{K'_m(w)}{wK_m(w)} \right] \\ &= m^2 \left( \frac{1}{u^2} + \frac{1}{w^2} \right) \left( \frac{n_1^2}{n_2^2} \frac{1}{u^2} + \frac{1}{w^2} \right). \end{aligned} \quad (2.52)$$



This eigenvalue equation can be utilized to understand and analyze the guided mode profile in an optical fiber. For known values of fiber parameters, above equation can be solved to determine the propagation constant  $\beta$ . Corresponding to each value of  $m$ , there are multiple solutions for optical modes in fiber. The supported modes in the fiber are hybrid modes denoted by  $HE_{mn}$  and  $EH_{mn}$  for which  $m \geq 1$ . The modes with strong electric field are EH modes and with strong magnetic fields are HE modes. In the special case of  $m = 0$  for which modes become radially symmetric,  $HE_{0n}$  and  $EH_{0n}$  are also denoted as  $TE_{0n}$  and  $TM_{0n}$  respectively.

In a weakly guiding approximation, we may assume  $n_1^2 \approx n_2^2 \approx n^2$ . The above equation reduces to the form

$$\left[ \frac{J'_m(u)}{uJ_m(u)} + \frac{K'_m(w)}{wK_m(w)} \right] = \pm m \left( \frac{1}{u^2} + \frac{1}{w^2} \right). \quad (2.53)$$

For HE modes, use  $-m$  while for EH modes, use  $+m$ . For TM or TE modes for which  $m = 0$ , the eigen value equation is

$$\left[ \frac{J'_m(u)}{uJ_m(u)} + \frac{K'_m(w)}{wK_m(w)} \right] = 0. \quad (2.54)$$

Customarily, the bracketed term in the RHS of the equation (2.53) is also written in terms of dimensionless parameter  $V$  such that

$$u^2 + w^2 = V^2. \quad (2.55)$$

This  $V$  is alternatively defined in terms of fiber parameter as

$$V = \frac{2\pi}{\lambda} a \sqrt{n_1^2 - n_2^2} \quad (2.56)$$

where  $\lambda$  is the wavelength of the light.

Modes are practically defined in terms of linearly polarized (LP) modes which are actually the combination of TE, TM, HE and EH modes. The following table shows the various combinations of modes to obtain LP modes.

Table 2.1: Some linearly polarized modes and their formation

Linearly Polarized Mode	Combination of TE, TM, HE, EH
$LP_{01}$	$HE_{11}$
$LP_{11}$	$HE_{21} + TE_{01} + TM_{01}$
$LP_{02}$	$HE_{12}$
$LP_{12}$	$HE_{22} + TE_{02} + TM_{02}$
$LP_{03}$	$HE_{13}$
$LP_{13}$	$HE_{23} + TE_{03} + TM_{03}$

## 2.4 Multicore photonic crystal fiber

Photonic crystal fiber (PCF) is different from conventional fiber in terms of micro-structured cladding with air holes surrounding the core. The micro-structured cladding influences the guidance properties of a fiber. It was first proposed in 1991 by P. Russel and was commercially available in 1996 [38]. PCFs are composed of a periodic array of air holes embedded in the glass (usually fused silica). They can have solid core or hollow core, based on the mechanism for guiding light. The fiber with solid core confines light by total internal reflection as the micro-structured cladding has lower index than the solid core. Fibers with hollow core guides light based on a photonic bandgap created by the micro-structured cladding. The size, shape and placement of air holes influence the propagation of light through a PCF. This is because the electric field overlaps with the air holes differently depending on the configuration. For example, increasing the nonlinearity depends on a large electric field confined within the glass regions of the fiber. The amount of pulse broadening due to dispersion depends on how the field is distributed between the air and glass regions as well. Designing the PCF provides some additional control over the fiber dispersion and nonlinearity compared with a solid fiber.

A multicore fiber (MCF) is an optical waveguide that has multiple cores in a common cladding. The array of waveguide channels may be coupled or uncoupled to one another depending on its design and uses. Uncoupled MCF works as a channel of multiple waveguides to transfer the energy undistorted over a distance reducing space occupancy. Coupled MCF has waveguide channels (cores) placed close to one another such that there occurs transfer of energy from one core to another and can be sub-grouped into weakly coupled and strongly coupled based on the distance of separation between cores. The former has relatively large core-to-core separation to minimize the mode coupling while the later has small core-to-core separation. One of the major advantages of MCF is the output power from each of multicore fiber that can be summed up to obtain higher output

power up to kilowatts which is not possible by conventional fiber. Use of MCF in laser scales up the power which can be further raised by increasing the numbers of cores [39, 40]. It has also potential applications in the high temperature applications [41]. Fig 2.4 is the cross section and the lengthwise view of a multicore fiber with solid cores formed by missing air holes in cladding in a linear arrangement.

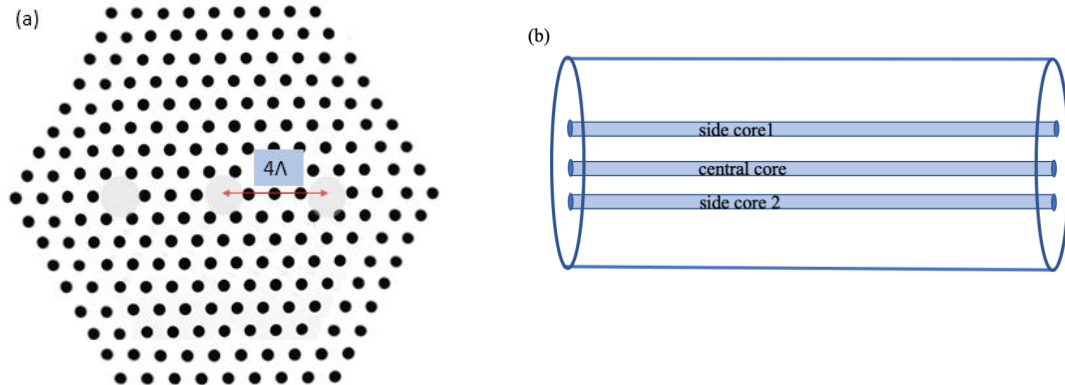


Fig. 2.4. 3-core fiber with cores in linear configuration (a) cross-section view (b) lengthwise view.

Fig. 2.5 is the Scanning electron microscope (SEM) images of a 3-core microstructure fiber. We obtained the core-core separation, hole-hole separation (pitch) and core diameter ( equals  $2 \times \text{pitch} - \text{airhole diameter}$ ) by analyzing these images using MS Paint software however, there are some errors in measurement due to lack of exact point location. We found that core-core separation =  $4 \times \text{Pitch} = 10.076 \pm 0.15 \mu\text{m}$ . Figure 2.5 (b) reveals that the cladding shape is hexagonal with air-holes arranged in triangular lattice. The fiber has a linear arrangement of cores created by a defect (air-hole missing) in the cladding. A detail of the specification of the fiber is tabulated as follows.

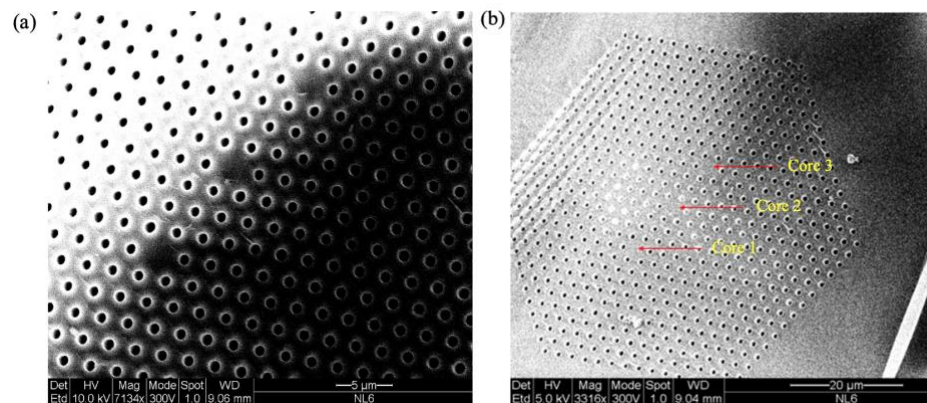


Fig. 2.5. SEM images of a 3-core fiber (a) a close-up of the liner arrangement of solid cores (b) Hexagonal shape of the air-holes in triangular lattice configuration in the cladding region.

Table 2.2: Fiber specification

Fiber parameter	Specification ( $\mu m$ )	Measured
Cladding diameter	$130 \pm 20$	$133 \pm 10$
Coating diameter	$260 \pm 20$	$248 \pm 20$
Core diameter	$3.9 \pm 0.2$	$4.08 \pm 0.3$
Air-hole diameter	$1.1 \pm 0.1$	$0.96 \pm 0.1$
Hole-hole pitch	2.52	$2.519 \pm 0.03$
Core separation	10.08	$10.076 \pm 0.15$
NA		0.19
ZDW		1060 nm

## 2.5 Modes in 3-core fiber

In a triple core fiber with cores in linear configuration as shown in figure 2.6, the mode coupling occurs only between the adjacent waveguides as the field decays exponentially outside the core region. The field from one of the side cores reaches indirectly to another side cores though the direct coupling is neglected between them. Figure 2.6 illustrates the mode coupling between cores in a triple core fiber. The modes are determined using coupled mode theory.

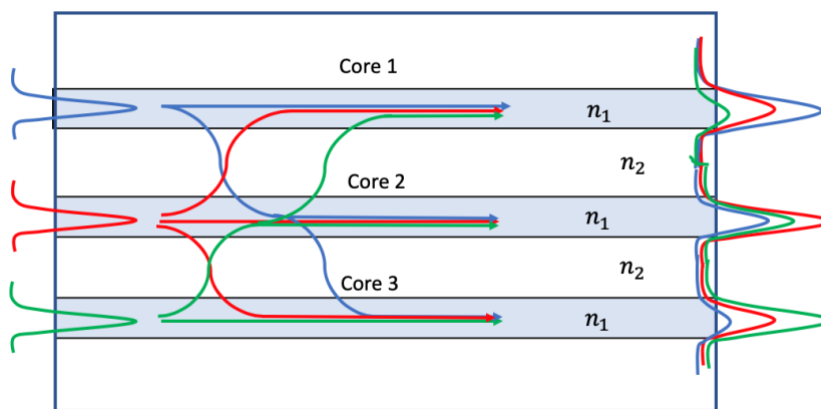


Fig. 2.6. Modes coupling between three waveguides.

In a couple mode theory, each core is treated as an independent waveguide with its own unperturbed modes. and introducing a perturbation theory, each core can be considered as perturbed by evanescent fields due to the coupling. So,  $\beta_j = \beta_0 \pm \kappa$  where  $j=1,2,3$  refers

to the core, 2 being the central core. The interaction between the modes of the three cores can be described in the matrix form [42, 43] as

$$i \frac{dA}{dz} + \bar{M}A = 0 \quad (2.57)$$

where,  $A = [A_1 \ A_2 \ A_3]^T$  and

$$\bar{M} = \begin{bmatrix} \beta_0 & \kappa & 0 \\ \kappa & \beta_0 & \kappa \\ 0 & \kappa & \beta_0 \end{bmatrix}. \quad (2.58)$$

The above equation can be solved by diagonalizing the coupled matrix  $Q^{-1}\bar{M}Q = \Lambda$  where,

$$\Lambda = \begin{bmatrix} \beta_1 & 0 & 0 \\ 0 & \beta_2 & 0 \\ 0 & 0 & \beta_3 \end{bmatrix} \quad (2.59)$$

where  $\beta_j (j = 1,2,3)$  are the propagation constants of the three super modes supported by a triple-core fiber. The solutions are

$$\begin{aligned} \beta_1 &= \beta_0 + \sqrt{2}\kappa \\ \beta_2 &= \beta_0 \\ \beta_3 &= \beta_0 - \sqrt{2}\kappa. \end{aligned} \quad (2.60)$$

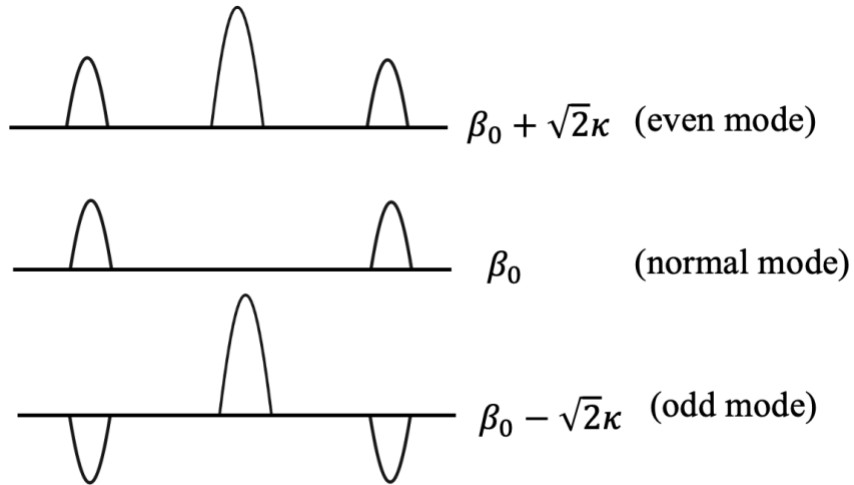


Fig. 2.7. The fundamental modes in a 3-core fiber

## CHAPTER 3

### LINEAR PROPERTIES OF A TRIPLE CORE FIBER

For the last few decades, scientists and engineers have studied nonlinear optical phenomena in photonic crystal fibers (PCFs) because of the ability to manipulate the core area and total dispersion. The propagation of an optical pulse in a standard fiber has been thoroughly investigated to study the effects of polarization, dispersion and Kerr nonlinearity [8]. Fibers with a single core are extensively used in the telecommunication and industrial sectors [7, 44-46]. However, in recent years, with the demands of high speed and high capacity optical systems, fibers with well-spaced multi-cores have emerged as the essential transmission medium for optical pulses [33]. It has been shown that multicore fibers offer an advantage of higher output compared with single core fiber with sharp switching characteristics and greater sensitivity to the input state [47, 48]. Multicore fibers have potential applications in spatial division multiplexing (SDM) technique by providing parallel channels for individual signals and thus improving the system capacity [49]. Each of the generated super-modes in multi-core fiber acts as one spatial channel. Linear optics in fiber relates to the intensity-independent process. The optical transmission dynamics of the fiber are affected by the linear and nonlinear effects associated with the fiber materials and pulse parameters. In this chapter, we report on the linear properties of a 3-core micro-structure fiber with the hexagonal matrix of air-filled holes for the wavelength ranging from 1 – 1.6  $\mu\text{m}$  and for the peak power ranging up to 1 kW. For the design and performance analysis of triple core fibers, their responses to interacting co-propagating modes in three cores must be well studied. Linear coupling in 3-core fiber is a periodic transfer of optical power among cores. For a given length of a fiber, the pulse energy may be partially or fully transferred to the neighboring cores before returning to the original core. Non-linear properties of a fiber will be discussed in the next chapter.

#### 3.1 Chromatic dispersion

Fiber dispersion is one of the important linear phenomena for the performance and transmission capacity of an optical communication system. When a light pulse propagates

in an optical fiber, it experiences dispersion due to the wavelength dependency of the refractive index of the core material. As a result, waves of different frequencies propagate at different speeds yielding the pulse broadening. The variation of the refractive index with respect to frequency is approximated by the Sellmeier equation given by

$$n^2 = 1 + \sum_{j=1}^m \frac{B_j \omega_j^2}{\omega_j^2 - \omega^2}. \quad (3.1)$$

where  $\omega_j$  is the resonance frequency and  $B_j$  is the strength of  $j^{\text{th}}$  resonance. This equation implies that the different spectral components propagating through a fiber will experience different indices of refraction and travel at different speeds resulting in the temporal broadening of the pulse [8]. In fact, the pulse envelope, centered at frequency  $\omega_0$ , propagates at the group velocity given by

$$v_g = \left( \frac{d\beta}{d\omega} \right)_{\omega=\omega_0}^{-1}. \quad (3.2)$$

where  $\beta = \frac{n(\omega)\omega}{c}$  is the propagation constant of a mode. Mathematically, the effect of fiber dispersion can be seen by a Taylor expansion of mode-propagation constant  $\beta$  about a central frequency  $\omega_0$  such that

$$\begin{aligned} \beta(\omega) = \beta(\omega_0) + (\omega - \omega_0) \frac{d\beta}{d\omega} + \frac{1}{2} (\omega - \omega_0)^2 \frac{d^2\beta}{d\omega^2} + \dots = \beta(\omega_0) + \\ (\omega - \omega_0)\beta_1 + \frac{1}{2} (\omega - \omega_0)^2 \beta_2 + \dots \end{aligned} \quad (3.3)$$

where, the dispersion coefficients are given by

$$\beta_m = \left( \frac{d^m \beta}{d\omega^m} \right)_{\omega=\omega_0}. \quad (3.4)$$

The first parameter  $\beta_1$  is simply a reciprocal of the group velocity of the pulse  $\beta_1 = v_g^{-1}$  and  $\beta_2$  is the group velocity dispersion (GVD) parameter which is an important factor for the pulse broadening.

The dispersion of a fiber is sometimes also given by

$$D = -\frac{2\pi c}{\lambda^2} \beta_2. \quad (3.5)$$

The dispersion causes temporal broadening of the pulses propagating in a fiber leading to the degradation of the output signal. The zero-dispersion wavelength (ZDW) for the silica

fiber is at 1312 nm [7]. However, the higher order dispersion may persist at  $\lambda = \lambda_D$  which can significantly distort the ultrashort pulses. The minimum attenuation for silica fiber occurs at 1550 nm [7]. The ZDW  $\lambda_D$  can be shifted in the vicinity of minimum loss wavelength. Such fiber is known as dispersion shifted fiber. The ZDW can be shifted into the visible regime by micro-structuring the fiber [50]. The interaction of dispersion with the fiber nonlinearity may result in soliton formation, the undistorted wave along the fiber length over a long distance [51]. The dominance of linear versus nonlinear effects during pulse propagation through a fiber is determined by comparing the fiber's physical length, dispersion length and nonlinear length. The dispersion length and nonlinear length are given by

$$L_D = \frac{T_o^2}{|\beta_2|} \quad (3.6)$$

$$L_{NL} = \frac{1}{\gamma P_o} \quad (3.7)$$

where,  $T_o$  and  $P_o$  are the time width and peak power of the input pulse respectively. For a given fiber length, the pulse propagation in a fiber depends on the relative magnitude of  $L_D$  and  $L_{NL}$ . The role of the fiber nonlinearity depends on the sign of the group velocity dispersion parameter ( $\beta_2$ ). If  $\beta_2 > 0$ , it is called normal dispersion regime where component with longer wavelength (red component) travels faster than the short wavelength component (blue component). While the red shifted components of pulse travel slower in anomalous dispersion regime if  $\beta_2 < 0$ .

Chromatic dispersion consists of material and waveguide dispersions. Material dispersion is caused by the wavelength dependence of the refractive index of the fiber core material while the waveguide dispersion is caused by the dependence of the mode propagation constant on the physical structure of fiber. It is one of the critical parameters that affects the propagating pulses. There are various factors like fiber parameters, propagating modes, medium, polarization states of modes, etc. that contribute to the dispersion.

**Material dispersion** is caused by the wavelength dependence of the refractive index of the fiber. Except the vacuum, all media are dispersive in nature. An electromagnetic field propagating through a medium is influenced by its dispersive behavior resulting the distortion in the signals. However, it can be manipulated by changing the refractive index profile. It is numerically calculated by taking the second derivative of the index of refraction of the medium with respect to wavelength as given by

$$D = -\frac{\lambda d^2 n}{c d\lambda^2}. \quad (3.8)$$



The material dispersion of a triple core fiber under test is estimated over a wavelength range 1-2  $\mu m$  using above equation (3.8) and is shown in figure (3.1). It increases with increase in wavelength.

**Waveguide dispersion** is caused by the dependence of mode on the fiber geometry. It depends on the normalized core-cladding index difference ( $\Delta$ ) given by equation (2.1a) and the core size. A general expression to determine the waveguide dispersion can be written as [46]

$$D(\lambda) = -\frac{n_2(\lambda)\Delta}{c\lambda} V \frac{d^2(Vb)}{dV^2} \quad (3.9)$$

where,  $b$  is the normalized propagation constant and is defined as

$$b = \frac{n_{eff}^2 - n_2^2}{n_1^2 - n_2^2} \quad (3.10)$$

where,  $n_1$  and  $n_2$  are the refractive indices of core and cladding regions respectively.  $n_{eff} = \beta/k$  is the effective refractive index of the guided mode. In an optical fiber, the effective refractive index experienced by a guided mode is different from core and cladding refractive indices.  $\beta$  and  $k$  are the propagation constant and the wave vector.

The geometrical term in equation (3.9) can be approximated as

$$V \frac{d^2(Vb)}{dV^2} = 0.08 + 0.549(2.834 - V)^2. \quad (3.11)$$

Equation (3.9) can be then expressed as

$$D(\lambda) = -\frac{n_2(\lambda)\Delta}{c\lambda} [0.08 + 0.549(2.834 - V)^2]. \quad (3.12)$$

Waveguide dispersion is negative in the entire wavelength range of 1-2  $\mu m$  and increases with the increase in wavelength. It reduces the value of material dispersion above the zero-dispersion wavelength. It is possible to design the fiber in such a way that the zero-dispersion wavelength can be shifted in the vicinity of operating wavelength. The waveguide dispersion of a triple core fiber is estimated by plotting above equation (3.12) and is shown in figure (3.1). Figure (3.1) is the plot of total dispersion along with the individual material and waveguide dispersion of the triple core fiber under test. It is estimated that the fiber has a total dispersion of approx. 38  $ps/nm-km$  and 1.7  $ps/nm-km$  at a wavelength of 1.30  $\mu m$  and 1.064  $\mu m$  respectively with the zero-dispersion wavelength

at approx.  $1.053 \mu\text{m}$ . Higher order dispersion coefficients  $\beta_m$  for  $m > 2$  are important for ultrashort pulses and can be neglected for picosecond pulses.

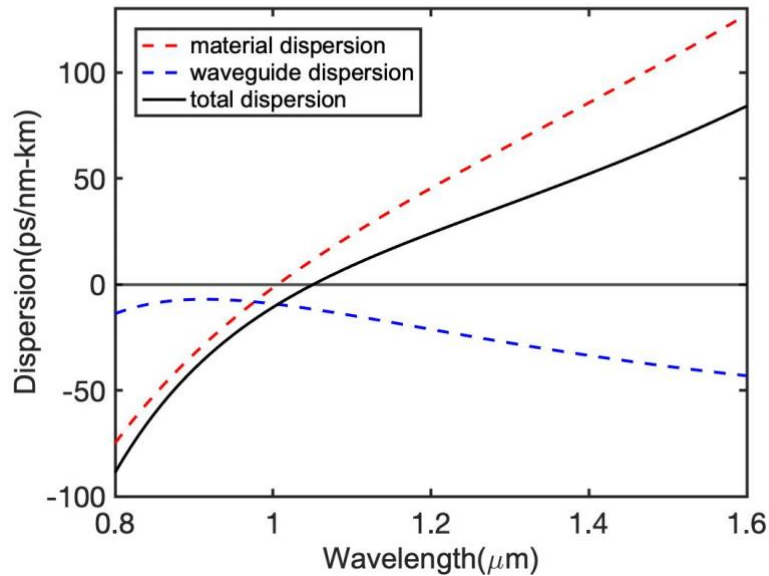


Figure 3.1. Total dispersion of a triple core fiber. Total dispersion is the sum of material and waveguide dispersions. It indicates that the fiber has a zero-dispersion wavelength at approx. 1053 nm below which is the normal regime with negative dispersion value and above which is the anomalous dispersion regime.

### 3.1.1 Numerical Aperture Measurement

We measured the numerical aperture using a knife edge method. The beam emerging out of the fiber was focused by a lens and was progressively covered by a knife edge (blade) along the position of the waist and transmitted powers were measured for 80%-20% intensity method. We assume that the input pulse is Gaussian, and its shape profile does not change as it propagates through the fiber. The numerical aperture is determined using  $NA = n \sin\theta$  where  $n = 1$  for air and  $\theta$  is the beam divergence angle and is given by

$$\theta = \frac{\lambda/n}{\pi w_o} \quad (3.13)$$

where,  $w_o$  is the beam waist radius at which the intensity is  $1/e^2$  times the maximum value. The value of  $w_o$  is determined from the relation

$$w(z) = w_0 \sqrt{1 + \left(\frac{\lambda z}{n\pi w_0^2}\right)^2} \quad (3.14)$$

where,  $w(z)$  is the position dependent beam radius which is determined experimentally at different distances along propagation ( $z$ ) as shown in table 3.1. The evolution of the beam radius as a function of propagation distance is plotted in figure (3.2). The straight line (black) is the linear fit to the data points.

Table 3.1: Measurement of beam radius and calculation of NA

Z-position	$\Delta X$	$w(z)$	$z$	$w_0$	NA
18	0.155	0.18414	0.983	0.001808	0.186
17.5	0.24	0.28512	1.483	0.001762	0.191
17	0.315	0.37422	1.983	0.001795	0.188
16	0.515	0.61182	2.983	0.001651	0.20
15	0.63	0.74844	3.983	0.001802	0.187
10	1.395	1.65726	8.983	0.001836	0.183
9	1.569	1.863972	9.983	0.001814	0.186
8	1.72	2.04336	10.983	0.00182	0.185

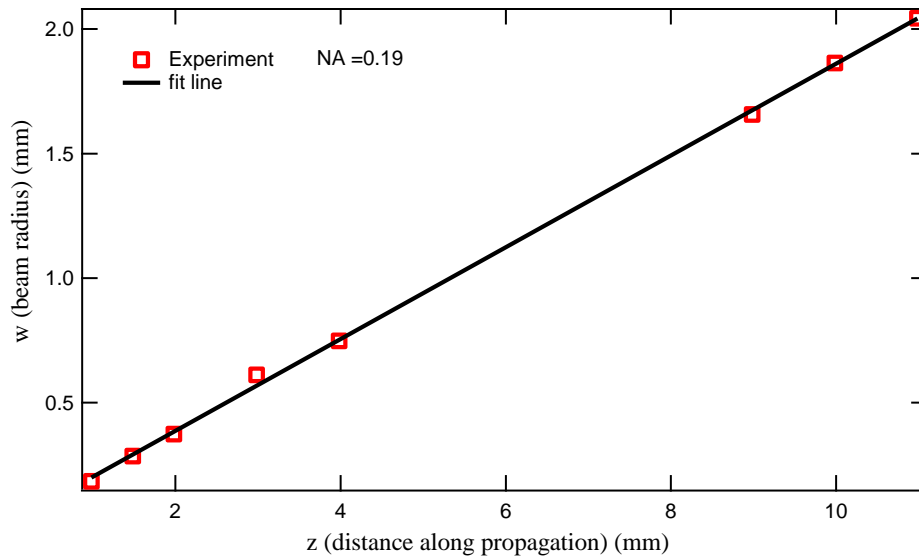


Fig. 3.2. Plot of the beam radius as a function of propagating distance.

We calculated the numerical aperture of the fiber to be 0.19 at a wavelength of 1064 nm. The V-number is then calculated using equation (2.1b) to be 2.19 at the wavelength of interest 1064 nm. The fiber supports single mode along all cores.

### 3.1.2 Dispersion measurement

To measure the dispersion of the fiber, we employed the time-of-flight method. We launch a  $\sim 200$  fs pulse from a tunable optical parametric oscillator (OPO) pumped by a mode-locked Ti-Sapphire laser as a wavelength-tunable source and record the variation in pulse arrival time as a function of wavelength using a 40 GHz oscilloscope as shown in Fig. 3.3, the schematic of dispersion measurement setup. The absolute propagation time cannot be determined from these measurements, but we can obtain the dispersion parameter,  $D$ , from the slope of those measurements.

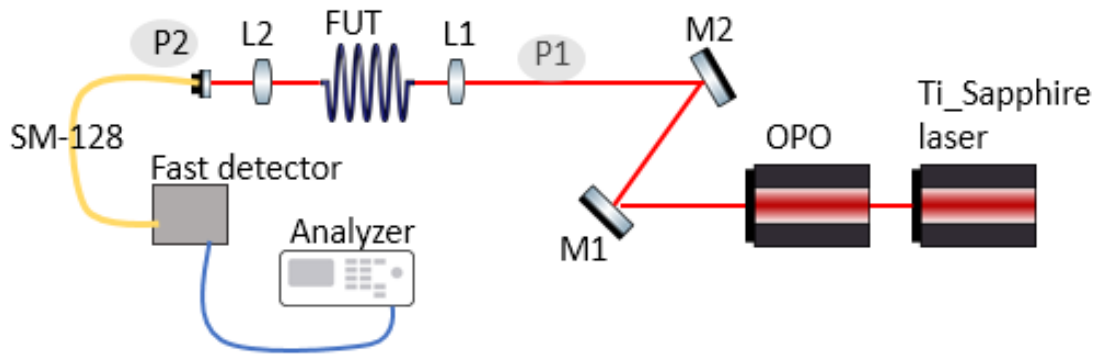


Fig. 3.3. Set up for the measurement of the fiber dispersion. Two mirrors M1 and M2 are used for better light coupling into fiber.

To measure the time delay of the pulses propagating through a 3-core fiber under test (FUT), pulses are detected by the fast detector transmitted by a patch cord (SM-128) and are then recorded by 40 GHz sampling oscilloscope. In the diagram, P1 and P2 are the measurement positions without and with fiber under test respectively. Due to the dispersion of the fiber and patch chord, the spectral peaks for the different wavelengths are located at the different positions. We record each spectral peak location in the oscilloscope trace for different wavelengths. The dispersion is calculated by the delay-wavelength differential relation

$$D = \left( \frac{d\tau}{d\lambda} \right) \left( \frac{1}{L} \right) \quad (3.15)$$

where,  $L$  is the length of the fiber. Measurement at P1 corresponds to the dispersion measurement due to the patch chord and measurement at P2 corresponds to the dispersion measurement due to both patch chord and the fiber under test. The dispersion only due to fiber is then calculated by subtracting the measurements at P1 from P2. Time delay measurements are performed over a wide range of wavelengths. Figure 3.4 are the two data graphs which can be used to calculate the dispersion of the patch cord. Here,  $\Delta\lambda = 19.5 \text{ nm}$ ;  $\Delta\tau = 1.2 \text{ ps}$  and therefore,

$$D = \left(\frac{1.2}{19.5}\right) \left(\frac{1}{0.003}\right) = 20.51 \left(\frac{\text{ps}}{\text{nm} - \text{km}}\right). \quad (3.16)$$

For a wavelength  $1.55 \text{ }\mu\text{m}$ , we found the average dispersion of the patch cord is  $20.50 \text{ ps/nm-km}$  which is very close to the specified value of  $20 \text{ ps/nm-km}$ .

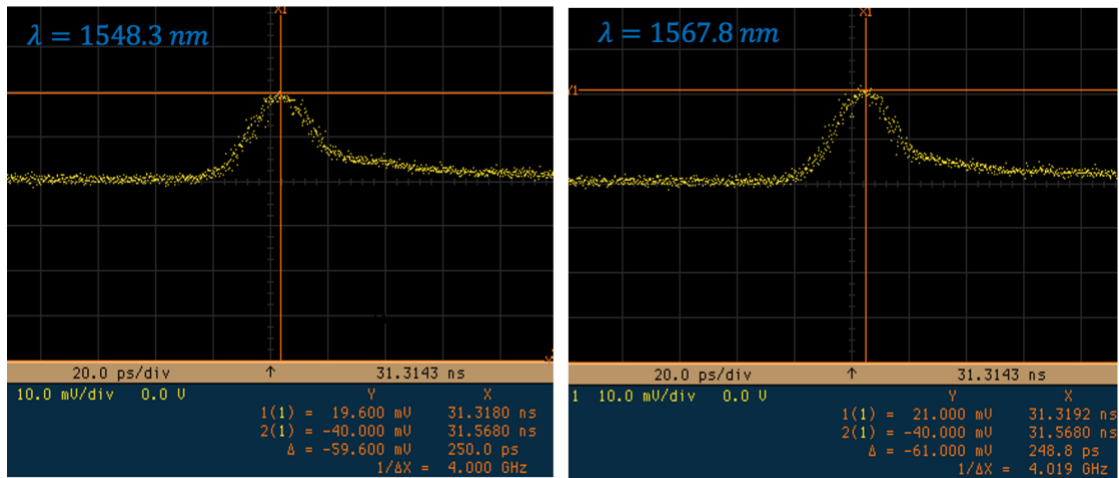


Fig 3.4. Oscilloscope traces for the measurement of time delay of the pulses at two different wavelengths.

To measure the dispersion of the triple core fiber, we measured the time delay of the pulses through each of the individual cores. Group velocity dispersion (GVD) measurements over a wavelength range from  $1064 \text{ nm}$ - $1600 \text{ nm}$  are shown in figure 3.5(a-b). We determined the dispersion of the 3-core fiber to be  $D = 36 \pm 5 \text{ ps/nm-km}$  at a wavelength of  $1.55 \text{ }\mu\text{m}$  regardless of which core is initially excited. However, the measured value may not be precisely accurate as it is difficult to accurately determine the pulse peak arrival time as TOF method needs a long piece of fiber to have significant difference in arrival time of pulses at different wavelengths. Figure 3.5(b) is a composite of time-of-flight measurements revealing a change from normal to anomalous group velocity dispersion in the vicinity of  $1064 \text{ nm}$ . The spectral gaps in the data of Fig. 3.5(b) are due to the fact that atmospheric absorption in those wavelength bands destabilizes our source. The GVD measurements presented in Fig. 3.5 indicate that we should be able to obtain phase-matched

parametric gain over a range of wavelengths near zero dispersion wavelength ( $\sim 1064$  nm) while the energy is distributed among the fiber cores.

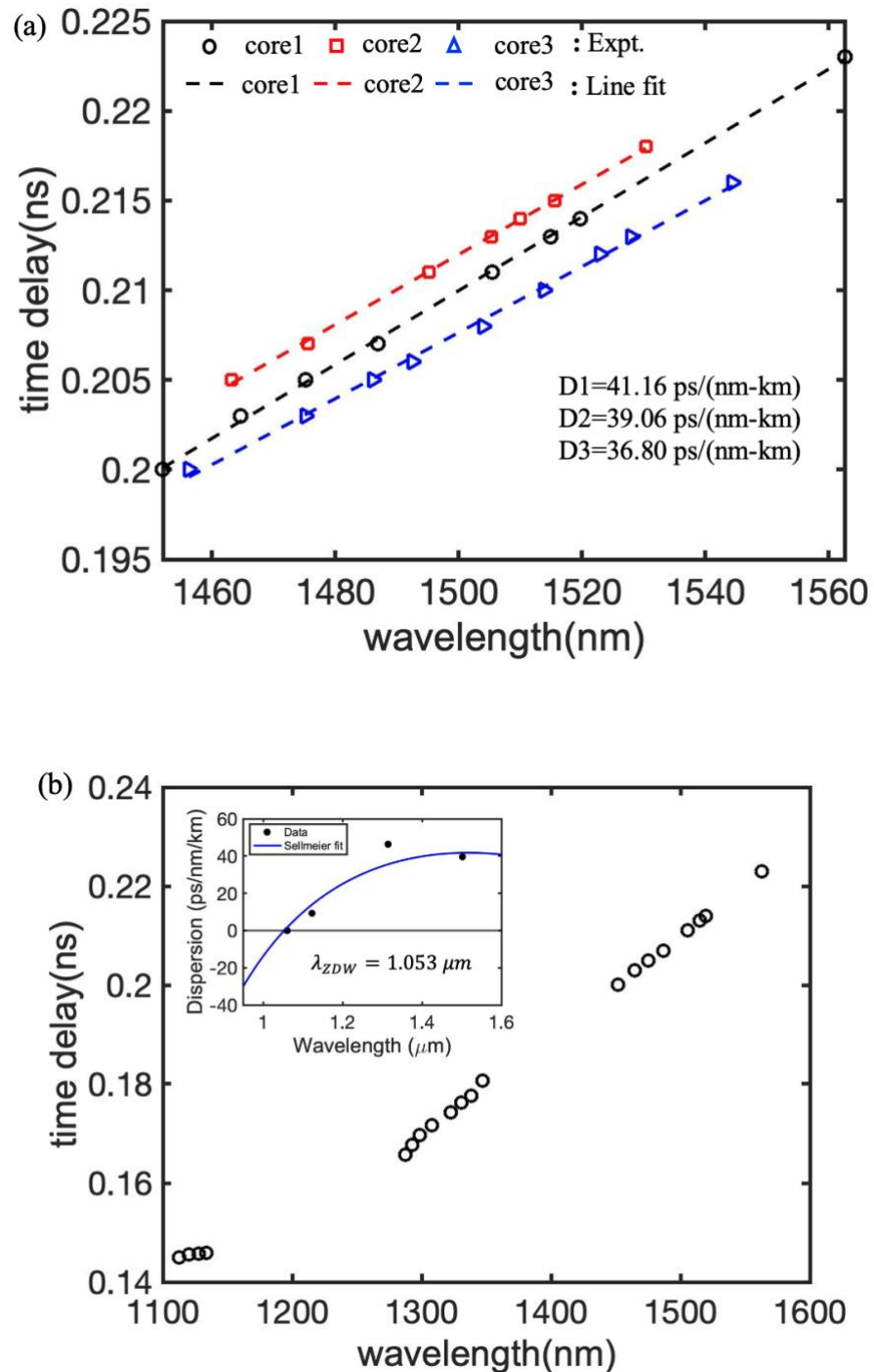


Fig. 3.5. (a) Time delay measurement for individual core of 3-core fiber and (b) for one of the side cores over a large range of wavelengths. The inset is the plot of the dispersion of the fiber at different wavelengths showing that the fiber has a zero-dispersion wavelength

at  $1060 \pm 20$  nm. The fiber has a maximum dispersion of  $43 \pm 10$  ps/nm/km at  $1310 \pm 20$  nm.

The dominance of linear vs. nonlinear effects during pulse propagation through a fiber is determined by comparing the fiber's physical length,  $L$ , dispersion length,  $L_D = \frac{T_0^2}{|\beta_2|} = \frac{2\pi c T_0^2}{\lambda^2 |D|}$ , and nonlinear length,  $L_{NL} = \frac{1}{\gamma P}$ , where  $T_0$  is the input pulse duration,  $\lambda$  is the wavelength, and  $\beta_2$  or  $D$  quantifies the group velocity dispersion. The value of  $D$  is  $2.70 \frac{ps}{nm km}$  and  $36 \frac{ps}{nm km}$  at wavelength  $1.064 \mu m$  and  $1.55 \mu m$  respectively. For our pulses of  $\lambda = 1.064 \mu m$  and  $T_0 = 8 ps$ , the dispersion length is  $8 \pm 1 km$ , and so dispersive pulse broadening plays a negligible role at a wavelength of  $1.064 \mu m$  as the optical fiber we used for our measurements has a maximum length of  $52 m$ . While, for our pulses of  $\lambda = 1550 nm$  and  $T_0 = 0.2 ps$ , the dispersion length of this fiber is  $1.0 \pm 0.1 m$  and both GVD and nonlinear effect can be seen on the pulse propagation.

## 3.2 Coupling between waveguides

One of the attractive linear phenomena is that the evanescent fields couple between the adjacent cores in a multicore fiber. The mode coupling allows the light energy to be transferred between the cores back and forth periodically. The coupling mechanism can be utilized to realize the novel applications like reducing nonlinearity impairment [52] and reducing group delay between modes [3,4] to improve the system performance. At the same time, the modes in different cores might have different group velocities giving rise to intermodal dispersion which may distort the evanescent fields while coupling back and forth between cores degrading the pulse shaping and output signals. It can break up the ultrashort pulses and thus degrades the switching characteristics [7,8]. Moreover, linear mode coupling may also be caused by the fiber imperfection which is avoidable during the fiber fabrication by choosing proper fiber design. But the mode coupling due to the presence of other channels in coupled multicore fiber is unavoidable. It is, therefore, important to establish an understanding of fundamentals and their impacts on the mode characteristics before practical implementation of fiber.

### 3.2.1 Mode Coupling in 3-core fiber

There occurs coupling of modes in different waveguides if they are placed close to each other. We conducted tests with short (35 cm), medium (5 m) and long (52 m) pieces of a triple core PCF and found coupling of light between adjacent waveguides for the long PCF. This helps to determine the coupling length, one of the important characteristic parameters of the coupled system. It is the shortest length for which the maximum power transfer

occurs between cores. For a fiber with three non-identical cores distributed linearly in the cladding region, the coupling length is given by

$$L_c = \frac{\pi}{2\sqrt{k_{12}^2 + k_{23}^2}} \quad (3.17)$$

when light is incident at central core and is observed to be wavelength dependent, where  $k_{12}$  and  $k_{23}$  are the coupling coefficients between cores 1-2 and 2-3 respectively. Fig. 3.6 (a, d) shows the microstructure and linear 3-core configuration for the fiber under test. We observe, however that the coupling coefficients between the central core and each of the side cores (as depicted in Fig. 3.6(d)) are not equivalent,  $\kappa_{12} \neq \kappa_{23}$ . We measured the core-to-core coupling by launching 8-ps pulses from a 1064-nm laser into a single side core (not the center) and viewing the output using a CCD camera. In Fig. 3.6 (b), the laser energy is distributed among the 3 cores in a manner consistent with propagation over a distance greater than the fiber's coupling length,  $L_c$ , for 1064 nm. In this case the energy is roughly equally distributed among the three cores regardless of the core into which the light was initially launched. The mode shape emerging from each core is robust to movements and bending of the fiber although the energy in each core does vary slightly. Measurements of the core-to-core coupling using a 200 fs-pulsed, 1550 nm laser exhibit the similar stability and coupling behavior. Measurements on a 35-cm long fiber (Fig. 3.6(c)) show that its physical length is less than  $L_c$ . The mode shape and relative intensity emerging from each core are robust to movements of the fiber and independent of the launched power. From these measurements we estimate  $L_c = 20$  m at 1064 nm, and 10 cm at 1550 nm. Observations of the coupling between cores for fiber lengths of 35 cm, 4.9 m, and 47 m are consistent with  $L_c = 20$  m at 1064 nm. A 5X microscope objective is used to image the end-face of the fiber on an IR camera to measure the intensity profile from each core. The camera is connected to the lab computer for image display. The instrumentation is controlled using LabVIEW®. Data analysis and simulations are done using MATLAB® 2017.



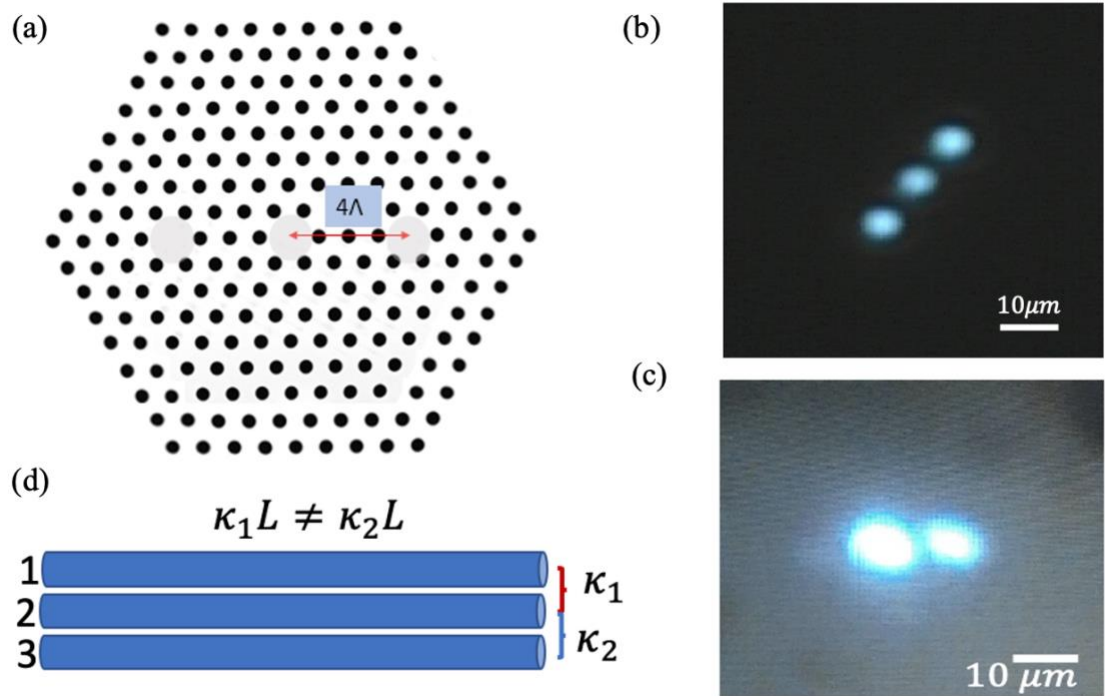


Fig. 3.6. (a) The cross-section of the fiber with 3-cores of diameter  $3.90\ \mu\text{m}$  in linear configuration arranged in a triangular lattice of air holes with a diameter of  $1.08\ \mu\text{m}$ . The hole to hole spacing ( $\Lambda$ ) is  $2.52\ \mu\text{m}$  and the distance of separation between the cores is  $4\ \Lambda$ . (b) Intensity distribution for a long (52 m) piece where coupling among the cores is evident. (c) Intensity distribution for a short (35 cm) piece of fiber illuminated with 1064 nm light from an 8-ps pulsed laser. (d) A general structure of a 3-core fiber showing different coupling coefficients between cores 1-2 and 2-3.

### 3.2.2 Mode coupling as a function of low power

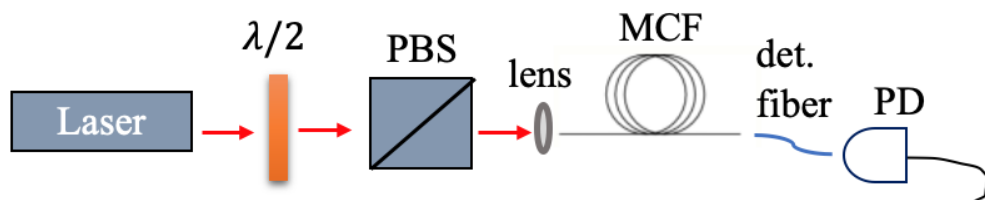


Fig.3.7. Experimental setup for the power measurement from individual cores. A combination of wave plate and beam splitting cube works as an attenuator that controls

amount of light at the fiber input end. The light beam is coupled in and out of fiber using lenses.

To investigate the mode coupling at the low power excitation (linear approximation), a CW beam from a tunable diode laser (DL Pro of Toptica) at a wavelength of 1064 nm is collimated and is focused onto the fiber under test using an objective lens that yields the beam spot size approximately equal to the core size. Laser light is launched into one of the cores by careful alignment of a 3-axis translation stage and the outputs from each core are characterized. The output from each core can be observed with a CCD camera (see Fig. 3.6(b)) or individually selected using a standard single-mode fiber (detecting fiber) aligned with a single core for power or spectral measurements. A combination of half wave plate and beam splitting cube is introduced in front of the fiber end to control the power of the input beam. The beam emerging out from the detecting fiber is then connected to optical spectrum analyzer (OSA) using a power detecting sensor.

When low power light is launched into one of the side cores (Fig. 3.8(a)), we observe that more than 60% of the power emerges from a side core, most likely the same core into which the light was launched. About 30% of the energy is coupled to the center core and less than 10% emerges from the remaining side core. Launching light in another side core yields more than 75% of the energy from the same core and remaining energy couples to other cores indicating that the coupling coefficients between the central core and each of the side cores are not equivalent. Whereas, exciting the central core yields only about 40% of the energy from that core and almost 40% of light is coupled to one of the side cores while almost half from another side core indicating that the coupling of central core with the side cores are not equivalent as shown in Fig. 3.8(b). The relative output power across each core remains constant and does not change with the input power. This suggests that low power has no effect in mode coupling and coupling happens only with the adjacent core. However, uncertainties arise because experimental measurements were manually done. The other important sources of error may be bad fiber cleave and bad coupling. To minimize the error in measurement, we well-tested the fiber cleave at both ends and automated the measurement system for the intermediate and high-power measurements which is discussed in chapter 4.

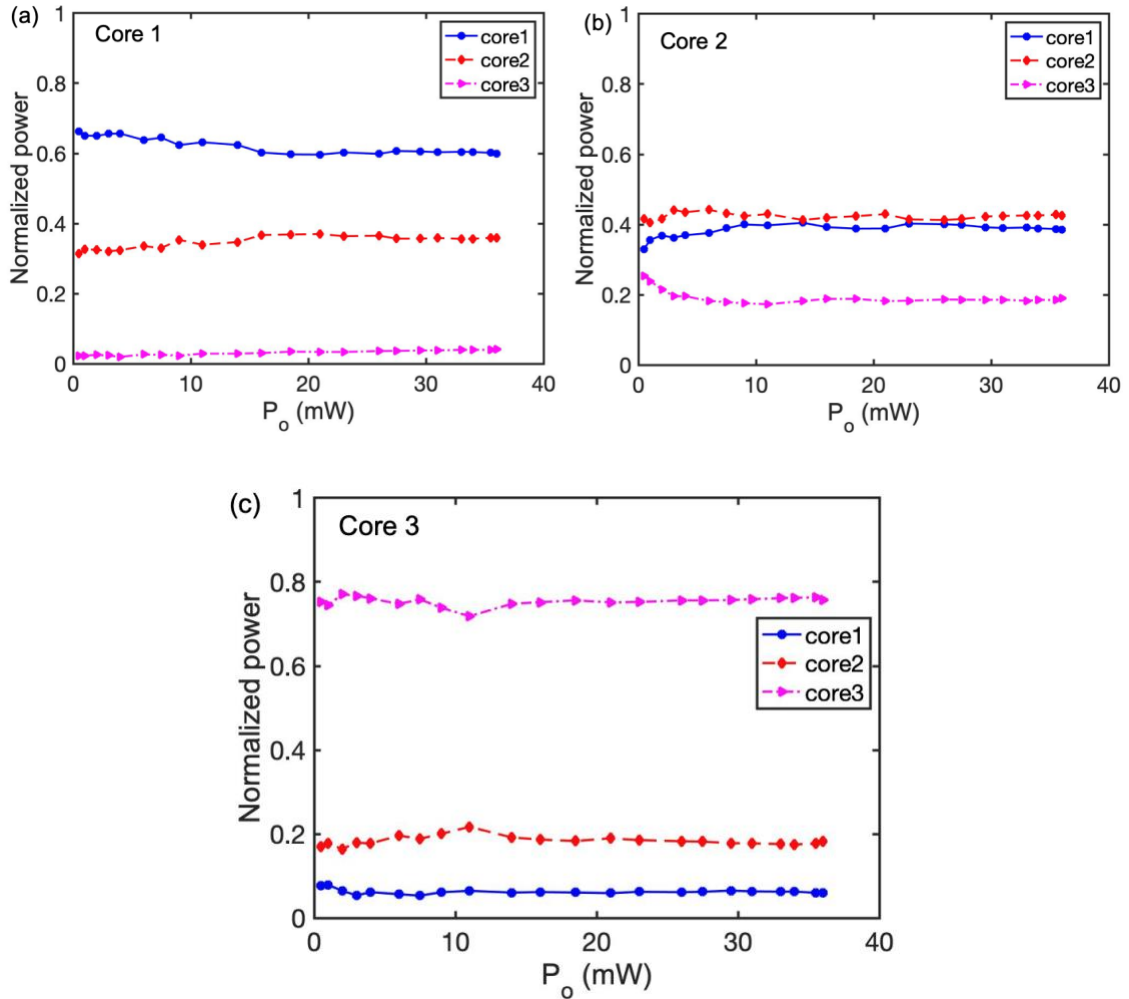


Fig. 3.8. Measurement of the relative output power across each core at low power when light is launched in (a) side core (b) central core (c) another side core.

### 3.2.3 Mode coupling as a function of wavelength

Measurements on figure 3.9 (a-c) were performed to establish the relation of mode coupling with the change in wavelength at low power. We excited different cores and scanned the total output power as a function of wavelength over a span of 20 nm centered at 1060 nm. The input power was kept constant at 16 mW from a CW tunable laser. The wavelength was tuned using an optical spectrum analyzer and the output power was recorded using power detector as in Fig. 3.7. The coupling of the light in a fiber is affected by the change in the wavelength as shown in Fig. 3.9(b) in which the light is launched in the central core and output measured from each core. It also shows that the effect of the change in wavelength on the adjacent core coupling is different for core 1-2 and for core

2-3 revealing that the coupling coefficient value for core 1-2 and core 2-3 configurations is different. Fig. 3.9 also verifies the measurements made in Fig. 3.8 for the low power in which for a wavelength of 1064 nm, excitation of one of the side core (core 1) yields approx. 65% of the light emergence while another side core (core 3) excitation yields almost 80% of total light and central core excitation yields almost 45% of the light. It also shows that the effect of the change in wavelength on the adjacent core coupling is different for core 1-2 and for core 2-3 revealing that the coupling coefficient value for core 1-2 and core 2-3 configurations are different.

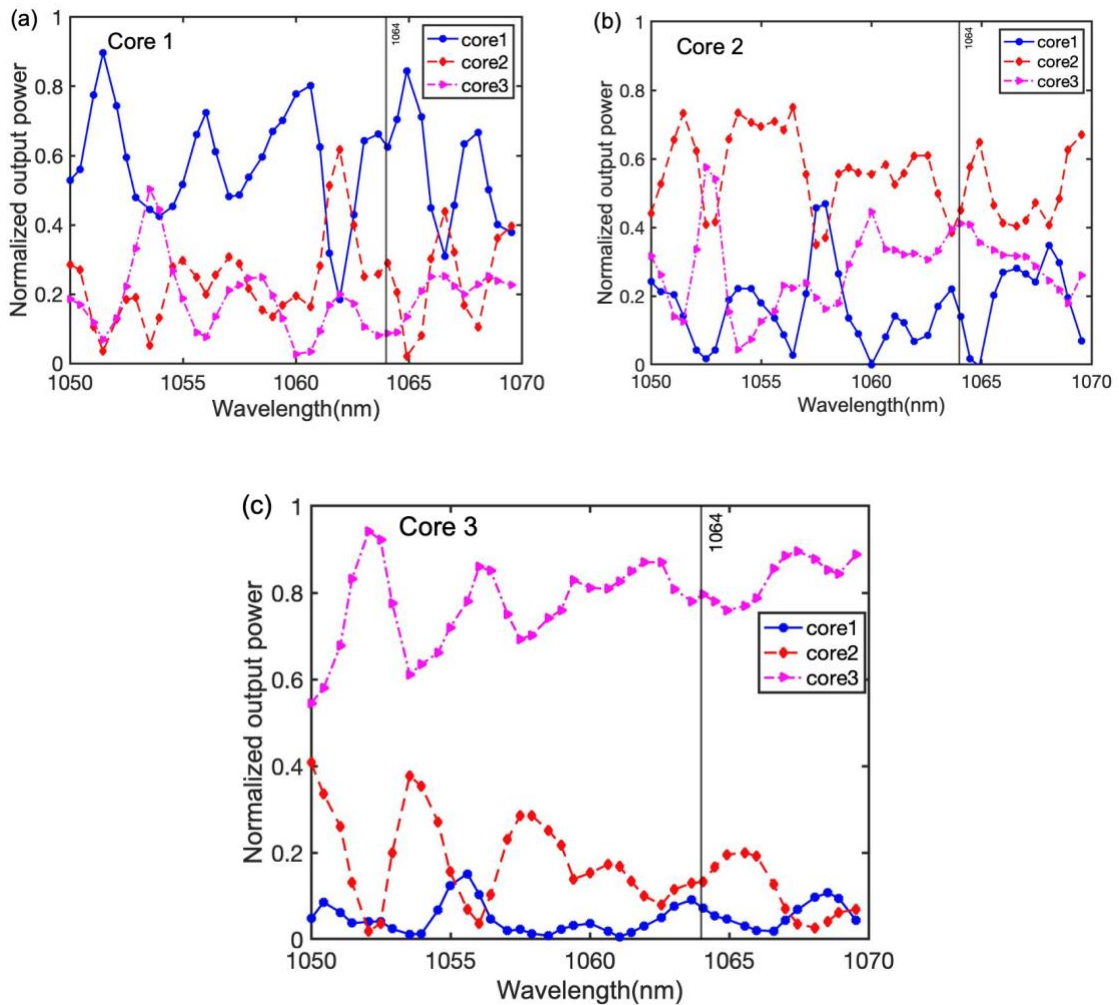


Fig. 3.9. Normalized output power measurement as a function of wavelength across each core when each core is individually excited.

The figure 3.10 is the total power measurement at the fiber output end when each of the cores is individually excited. Here the total power implies the sum of the power measured

out of all cores. Figure 3.10(a-b) both reveal that the output power is the wavelength dependent. In 3.10(a), output power measurement as a function of wavelength is compared to the input power of the laser source measured at different wavelength emission. At a wavelength of 1064 nm, it does not make much difference in total output power when measurement is made at any core as shown in figure 3.10(b). However, exciting each core might provide different total output power at other wavelengths as shown in figure 3.10(b).

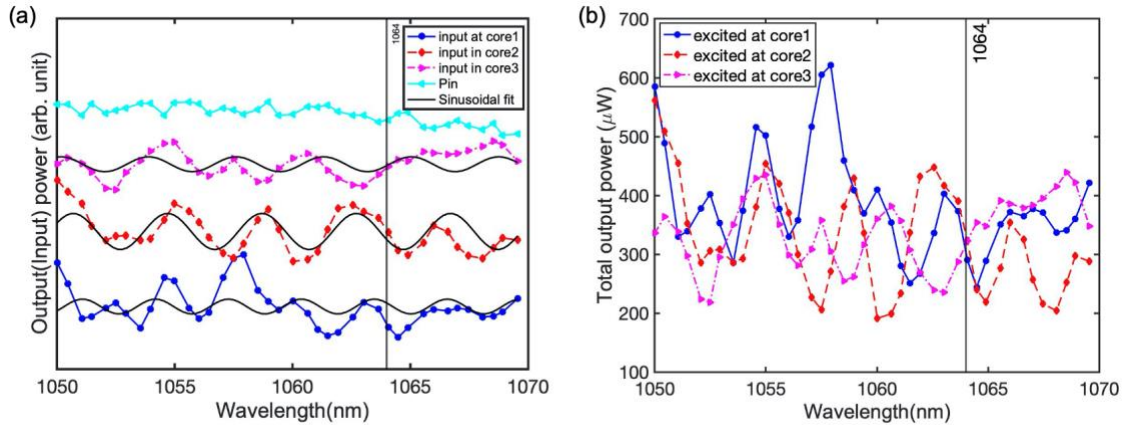


Fig. 3.10: Total output power measurement as a function of wavelength when individual core is excited. (a) Power measurement at the fiber output end showing the nature of sinusoidal wave compared to the nature of laser source emission at different wavelength. (b) Total output power measurement when each core is excited showing how coupling is affected with the wavelength. It shows that for a wavelength 1064 nm, the output power emerging out of each core remains almost same, however, for other wavelength around it, coupling seems to be changing.

### 3.2.4 Mode coupling as a function of polarization

In an optical fiber, the light travels in the form of modes. There is always presence of inter-modal coupling in a coupled multicore fiber. The wavelength-dependent nature of refractive index might also affect the inter-modal coupling when light propagates through the fiber. To investigate the effect of polarization on the mode coupling, we launch 8-ps pulses from a mode-locked laser (Time bandwidth Nd-Vanadate) at a wavelength of 1064 nm into 2<sup>nd</sup> core of a 5-m long 3-core fiber. We placed a combination of HWP and PBS cube after the isolator at the input end and a HWP was inserted just in front of fiber input. The rotation of HWP changes the polarization of the input light. In Fig. 3.11(a), we observe that the power emerging out of each core changes with the rotation of HWP at the fiber

input end. It also indicates that the change is different for the different cores with different amount of power.

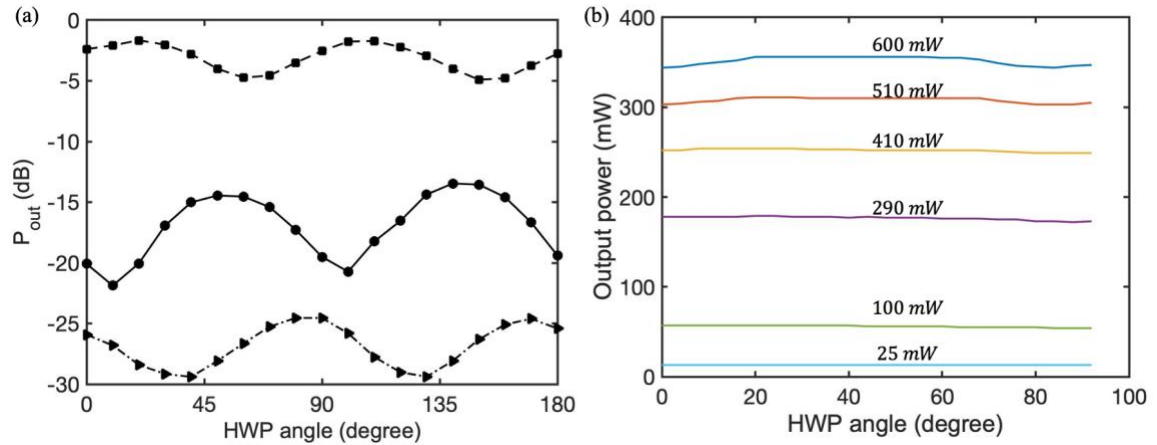


Fig. 3.11. Measurement of polarization dependence of mode-coupling in a fiber. (a) Change in the output power in each core as a function of half-wave plate angle when a constant input light was launched into core 2. (b) Total output power measurement at the fiber output end as a function of HWP angle at different input power.

In Fig. 3.11(b), we measured the total output power at the fiber end with respect to change in polarizing angle at different input power. We observe that the change in output power is more at higher input power. There might be some other factors like fiber nonlinearity which might be dominant at higher power affecting the mode coupling. We present polarization-dependent of the mode coupling in a 3-core microstructure fiber.

### 3.3 Coupling coefficient and coupling length

There occurs a periodic transfer of optical power among cores due to the overlap of evanescent fields in each core in a coupled multicore fiber. For a given length of fiber, the pulse energy may be partially or fully transferred to the neighboring cores and finally, come back to its original core. The overlap of the evanescent fields in the core is referred as the coupling coefficient. It depends on the area of overlap of the individual core modes. Small mode overlap leads a small coupling coefficient and vice-versa. It also varies along the length of fiber due to imperfections in the fiber, which we neglect assuming that the degree of imperfection is very low. For the linear characteristics, we assume the propagation in a low intensity field. The coupling coefficient depends mainly on the fiber parameters and the operating wavelength. The coupling length, the fiber length for which the transfer of energy from one core to another occurs completely, depends on the coupling coefficient given by re-writing from equation 3.17 assuming identical coupling coefficient as

$$L_c = \frac{\pi}{2k} \text{ for bi-coupler} \quad (3.18)$$

$$L_c = \frac{\pi}{2\sqrt{2}k} \text{ for identical tri-coupler} \quad (3.19)$$

where,  $k$  is the coupling coefficient between cores in a bi-coupler or tri-coupler. For a fiber with triple cores in a linear configuration, when light is launched into a side core, the coupling length is given by equation (3.18) and when the light is launched into the central core, it is given by equation (3.19). These indicate that the coupling lengths for central core is slightly shorter than for the side-cores. As a result, the central core has slightly higher coupling coefficient than the side cores. This may have adverse effect on the pulse propagation in a multicore fiber. However, the possible distortions which may be caused by the coupling effects in multicore fiber can be reduced by considering appropriate fiber parameter during its fabrication and suitable dispersion compensation in fiber.

The coupling coefficient in a step-index single mode fiber can be estimated using empirical expression as mentioned in [53, 54],

$$\kappa = \frac{\pi V}{2k_0 n r^2} \exp[-(A_1 + A_2 \bar{d} + A_3 \bar{d}^2)] \quad (3.20)$$

where,  $k_0 = \frac{2\pi}{\lambda}$  is the wave vector,  $A_1 = 5.2789 - 3.663V + 0.3841V^2$ ;  $A_2 = -0.7769 + 1.2252V - 0.012V^2$ ;  $A_3 = -0.0175 - 0.0064V - 0.0009V^2$ ;  $\bar{d} = \frac{d}{r}$  is normalized distance for  $d$  being the distance of separation of two cores,  $r$  is the core radius and  $V = k_0 r \sqrt{n_1^2 - n_2^2}$  is normalized frequency (V-number).

Furthermore, the coupling coefficient can also be measured as the overlap of modes in two adjacent cores as we determined in chapter (2). It is given by [54]

$$\kappa = \sqrt{2\Delta} \frac{u^2}{aV^3} \frac{K_0\left(\frac{wd}{a}\right)}{K_1^2(w)}. \quad (3.21)$$

$u$  is the solution of the following characteristics equation which is solved in chapter 2.

$$\frac{uJ_1(u)}{J_0(u)} = \frac{wK_1(w)}{K_0(w)} \quad (3.22)$$

where,  $J_0$  and  $J_1$  are the zero and first order of Bessel function of the second kind and  $K_0$  and  $K_1$  are zero and first order of modified Bessel functions of second kind. These equations cannot be solved analytically so we used numerical approach to calculate the coupling coefficient. We used Sellmeier equation (3.1) to determine the refractive index of

the background material, which is wavelength dependent. The accuracy of the coupling coefficient calculation depends on the refractive index profile and the core size.

We estimated the coupling coefficient of the fiber by solving optical modes in step-index fiber using equation (3.21) and the empirical relation (3.20) and their plots are shown in figure 3.12. The discrepancies in the two calculations will be less than 1% if the values of  $V$  and  $\bar{d}$  lie at  $1.5 \leq V \leq 2.5$  and  $2.0 \leq \bar{d} \leq 4.5$ . In Fig. 3.12, we see a big difference in calculation of coupling coefficient which is due to the fact that we choose the  $V \geq 2.5$  and  $\bar{d} = 5.17$  for our fiber and therefore, the empirical relation underestimates the value of coupling coefficient of the optical fiber.

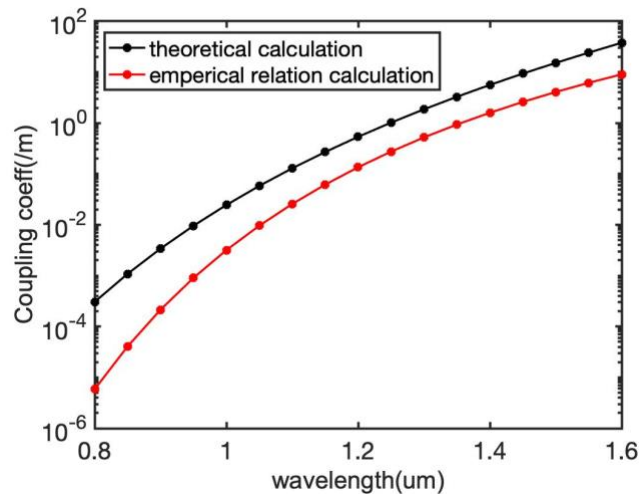


Fig. 3.12. Numerical calculation of the coupling coefficient value using the theoretical approach (black) and empirical relationship (red) in equations 3.21 and 3.20 respectively. The empirical relation for the determination of coupling coefficient underestimates the value compared to the theoretical approach.

The graph reveals that the fiber has a coupling coefficient of around 0.058/m that corresponds to the coupling length of 20 m at the operating wavelength of 1064 nm. The coupling coefficient increases with the increase in the wavelength. Depending on its use in parametric devices where we need weak or strong coupling, we can always use different operating wavelengths for which coupling is weak or strong. Moreover, mode coupling depends on the distance of separation between cores. Closer the cores are, more the coupling coefficient is. So, the desired gain can also be achievable by fixing core's distance with the same air filling fraction during its fabrication.



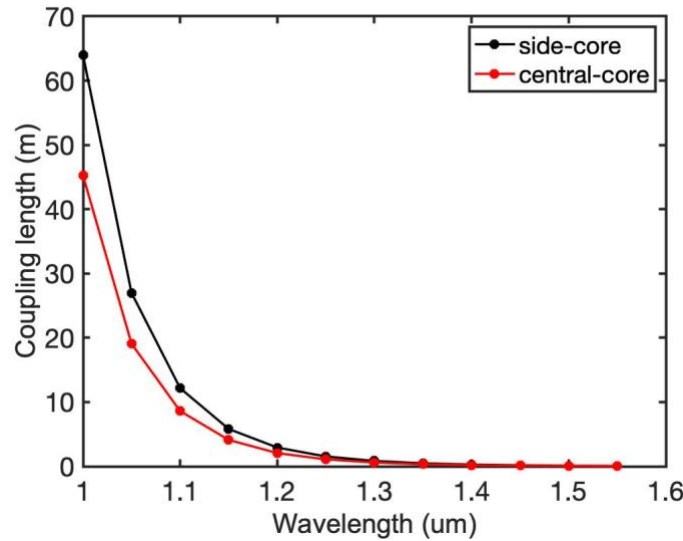


Fig. 3.13. Numerical calculation of the coupling length for side-core and central-core of a 3-core optical fiber using the theoretical approach of mode solution in an optical fiber.

Figure 3.13 is the plot of equations 3.18 (black) and 3.19 (red) for side-core and central core of a 3-core fiber. The coupling length for the central core is comparatively less than that of side core as the modes in central core are coupled to both side cores while in case of side core, it is only coupled to the adjacent core (central core). The coupling length is approximately 20 m and 29 m for central core and side cores at a wavelength of 1064 nm respectively.

### 3.4 Coupling induced dispersion

Besides the chromatic dispersion, a coupled-multicore fiber may have significant dispersion arose due to the time delay of modes of different cores via the evanescent fields. In a coupled multi-core fiber, the neighboring cores are sufficiently close for the overlap of evanescent field of each core. This leads to the power transfer between the modes of cores and its neighbor periodically. In the triple core fiber of interest, we consider the overlap of wavefunctions between only the nearest neighbor cores. The overlap of the pulse in cores is defined in terms of coupling coefficient and is considered frequency dependent. Its expansion using Taylor series is

$$\kappa(\omega) = \kappa_0 + (\omega - \omega_0)\kappa_1 + \frac{1}{2}(\omega - \omega_0)^2\kappa_2 + \dots \quad (3.23)$$

where,  $\kappa_1 = \frac{d\kappa}{d\omega}$  is first order coupling coefficient dispersion term and we neglect 2<sup>nd</sup> or higher order effects as they are very small compared with the first order coupling term. As a fact, the pulse gets broadened due to coupling induced dispersion. Figure 3.14 is the plot of the coupling coefficient induced dispersion as a function of wavelength. It increases with the wavelength. The coupling coefficient dispersion degrades the transfer of energy among cores. The fiber does not have significant amount of coupling induced dispersion for the wavelength around 1.06  $\mu\text{m}$  but, it can be significant for the longer wavelength. However, this can be minimized by choosing appropriate fiber parameters or V-number where mode delay due to coupling disappears. These results can be useful for the design and fabrication of a multicore fibers for directional couplers or other purposes.

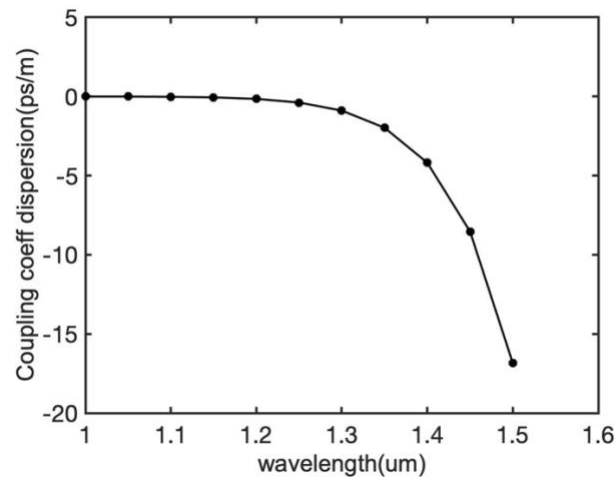


Fig. 3.14. Numerical calculation of the coupling coefficient induced dispersion.

### 3.5 Summary

In this chapter, we described our experimental works performed to characterize the dispersive and nonlinear properties of a triple core micro-structured fiber along with the necessary fundamentals required to understand our work. We determined the group velocity dispersion over a wavelength range from 1064 nm - 1600 nm and found that the zero-dispersion wavelength lies close to 1060 nm. We use a time-of-flight technique wherein we launch  $\sim 200$  fs pulses from a tunable optical parametric oscillator and record the variation in pulse arrival time as a function of wavelength using a 40 GHz sampling oscilloscope. We investigated the coupling characteristics of a 3-core fiber in a linear approximation using CW beam. We also observed the mode coupling at low power and found that mode coupling is not affected by low powered light. We observed that the core-

to-core coupling coefficients between the central core and each of the side cores are not equivalent ( $\kappa_{12} \neq \kappa_{23}$ ). We noticed that the coupling is wavelength-dependent leading to intermodal dispersion which is not studied here. The broadening is more for the side core excitation compared to the central core excitation for the same input power. This is due to the mode coupling of the central core with the two side cores. We then determined the dispersion length ( $8 \pm 1 \text{ km}$ ) for our pulses of  $\lambda = 1.064 \mu\text{m}$  and  $T_0 = 8 \text{ ps}$ , and so dispersive pulse broadening plays a negligible role here. To understand the mode coupling better, we also investigated the core-to-core coupling as a function of polarization and found that the coupling varies by about 50% as a function of the polarization of the launched light. In our linearly aligned 3-core fiber, we found that the coupling coefficients were not equal, but microstructure fibers provide large design space. For example, one can fine tune the core-to-core spacing to achieve balanced coupling or change the design to introduce more coupled cores. We also numerically calculated the coupling induced dispersion to investigate its effect and pulse broadening and we found that for a wavelength of  $1.064 \mu\text{m}$ , it has negligible effect while for the wavelength of  $1.3 \mu\text{m}$  or higher, it may have significant effect on the pulse broadening. Studying the limitations and opportunities offered by the fiber linearity and nonlinearity help in optimizing fiber parameters during its fabrication to extract maximum possible gain from a system. We anticipate that our findings help to mitigate the linear and nonlinear effects while implementing a multicore fiber for practical use.

## CHAPTER 4

### NONLINEAR PROPERTIES OF A TRIPLE CORE FIBER

Non-linear optics in fiber correspond to intensity-dependent processes. A third order nonlinear process is always associated with a fiber. The nonlinear response of the fiber is important as it may influence the shape and propagation of a pulse [55, 56]. With the change in the intensity of light, there arises a modulation in the refractive index of the material of the fiber. This is referred as Kerr's effect. This gives rise to the nonlinear effects like self-phase modulation (SPM) (pulse changes its own phase), cross phase modulation (XPM) (a pulse affects the phase of other pulses) and four wave mixing (pulses with different frequencies interact to produce a new frequency). The nonlinear behavior also arises due to the interaction of a pulse with phonons (acoustic or molecular vibration) in the fiber such as stimulated Brillouin scattering (SBS) and stimulated Raman scattering (SRS). These nonlinearities may affect the pulse shape, decrease signal to noise ratio (SNR), increase crosstalk between channels etc. On the other hand, they can be used for switching, wavelength conversion, amplification of signals, etc. Generation of optical solitons makes transmission of optical pulses possible over a large distance without degradation. Studying the limitations and opportunities offered by the fiber linearity and nonlinearity helps in optimizing fiber parameters during fabrication to extract maximum possible gain from a system. The linear optics in the fiber has been discussed in detail in chapter 3. In this chapter, we study the origin of the fiber nonlinearity and its effect in the pulse propagation. We also analyze the effect of the fiber nonlinearity on the output spectrum and determine the nonlinear parameter of a triple core fiber.

#### 4.1 Origin of nonlinear effects

The non-linear effect that we are concerned with in the fiber is the Kerr non-linearity which is the intensity dependence of the refractive index. The refractive index, in general, can be written as  $n(\omega, I) = n_l(\omega) + n_{nl}I$  where  $n_l(\omega)$  is the linear part which is the largest component, and  $n_{nl}$  is the non-linear index coefficient. The non-linear response is related

to the anharmonic motion of bound electrons under the influence of an applied field. The total polarization  $\mathbf{P}$  induced by electric dipoles satisfies the relation [8]

$$\mathbf{P} = \varepsilon_0(\chi^1 \cdot \mathbf{E} + \chi^2 : \mathbf{E}\mathbf{E} + \chi^3 : \mathbf{E}\mathbf{E}\mathbf{E} + \dots) \quad (4.1)$$

where,  $\mathbf{E}$  is the electric field and  $\varepsilon_0$  is the permittivity of free space. For an isotropic medium,  $\mathbf{P}$  is always in the direction of  $\mathbf{E}$ . Assuming  $\mathbf{E} = E_0 \cos(\omega t - kz)$ , and neglecting the effect of  $\chi^2$  for fiber, we obtain

$$P = \varepsilon_0 \chi^1 E_0 \cos(\omega t - kz) + \frac{3}{4} \varepsilon_0 \chi^3 E_0^3 \cos(\omega t - kz) + \frac{1}{4} \varepsilon_0 \chi^3 E_0^3 \cos 3(\omega t - kz). \quad (4.2)$$

Higher orders are neglected. 3<sup>rd</sup> term in equation (4.2) can also be neglected because of phase lack between frequencies  $\omega$  and  $3\omega$ . Defining the intensity of the light in the form

$$I = \frac{1}{2} c \varepsilon_0 n_l E_0^2, \quad (4.3)$$

we get the polarization to be

$$P = \varepsilon_0 \chi^1 E_0 \cos(\omega t - kz) + \frac{3}{2} \frac{\chi^3}{c \varepsilon_0 n_l} I E_0 \cos(\omega t - kz). \quad (4.4)$$

Therefore, effective susceptibility and effective refractive index can be written as

$$\chi_{eff} = \frac{P}{\varepsilon_0 E} = \chi^1 + \frac{3}{2} \frac{\chi^3}{c \varepsilon_0 n_l} I \quad (4.5)$$

$$n_{eff} = (1 + \chi_{eff})^{\frac{1}{2}} = n_l + n_{nl} I \quad (4.6)$$

where,  $n_l = (1 + \chi^1)^{\frac{1}{2}}$  is linear refractive index of a medium and  $n_{nl} = \frac{3}{2} \frac{\chi^3}{c \varepsilon_0 n_l}$  is nonlinear refractive index. Linear part is always dominant. Although nonlinear term is small, over a large length of fiber, it may become significant and may therefore, be responsible for soliton formation. For silica fiber,  $n_l(\omega) \cong 1.5$  and  $n_{nl} \cong 10^{-20} \text{ W/m}^2$  [7]. This huge difference in  $n_l(\omega)$  and  $n_{nl}$  indicates that large intensities are required for non-linear effects to play a significant role. The nonlinear refractive index gives rise to the nonlinear parameter given by

$$\gamma = \frac{n_{nl}\omega}{cA_{eff}} \quad (4.7)$$

where,  $c$  is the speed of light and  $A_{eff}$  is the effective mode area and is defined as

$$A_{eff} = \frac{(\iint_{-\infty}^{\infty} |F(x, y)|^2 dx dy)^2}{\iint_{-\infty}^{\infty} |F(x, y)|^4 dx dy} \quad (4.8)$$

where,  $F(x, y)$  is the modal distribution and is determined in chapter-3 for the fundamental fiber mode.

## 4.2 Self-phase modulation (SPM) parameter

The refractive index of a nonlinear medium depends on the optical intensity (called Kerr's effect) through an equation

$$n(\omega, I) = n_0(\omega) + n_2 I(t). \quad (4.9)$$

This intensity dependence generates nonlinear phase shift and therefore, an optical field modifies its own phase. This is called self-phase modulation. Because of SPM, the spectrum changes when an intense optical field propagates through the fiber. Different parts of the pulse undergo different phase shift because of intensity dependence of phase fluctuations. This produces spectral broadening and an effect often called “chirp” of the pulse while the temporal shape remains unaltered. The SPM effects dominate in systems with high transmitted power as the chirping effect is proportional to the transmitted signal power. One of the applications of SPM is the formation of solitons. SPM leads to chirping with lower frequencies in the leading edge and higher frequencies in the trailing edge. This chirping effect is opposite to the chirping caused by linear dispersion. So, one effect can be compensated with the other with a proper choice of shape (a hyperbolic secant shape) and the power carried by the pulse. The new pulse propagates undistorted over a long distance by mutual compensation of dispersion and SPM. Such a pulse is called a soliton which does not broaden during its propagation.

### 4.2.1 Determination of SPM value

We measured the optical nonlinearity,  $\gamma$ , of the fiber by recording optical spectra and quantifying the amount of SPM as a function of power, wavelength, and fiber length.

Figure 4.1 shows a sample of such measurements for 8-ps pulses at a wavelength of 1064 nm for light launched into one of the side cores. The physical length of this fiber is 5 m. As the average power is increased from 4 mW to 12 mW, SPM leads to an increasing number of peaks in the spectrum. The number of peaks in the spectrum increases linearly with the value of maximum nonlinear phase shift  $(\phi_{NL})_{max}$ . We calculate the corresponding  $(\phi_{NL})_{max}$  using a relation  $(\phi_{NL})_{max} = \left(M - \frac{1}{2}\right)\pi$  where M is the number of peaks. Substituting the value of the slope from graph in equation  $\gamma = \frac{\text{slope}}{L_{eff}}$  gives a value of  $13 \pm 3 W^{-1}km^{-1}$ .

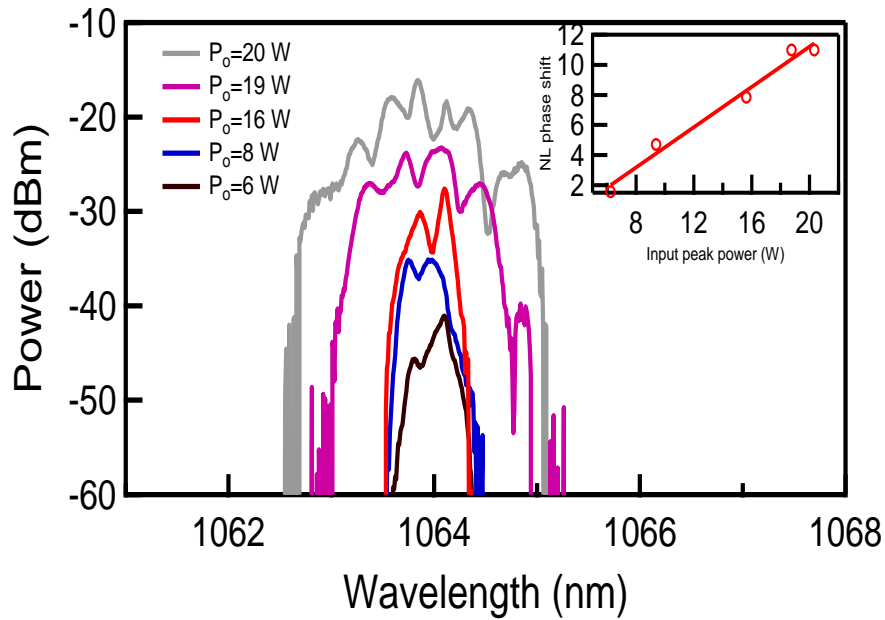


Fig. 4.1. Spectra showing self-phase modulation. Inset is the plot of  $(\phi_{NL})_{max}$  as a function of peak power for a 3-core fiber of length 5 m and the slope of the linear regression fit gives a value for the ratio  $\frac{(\phi_{NL})_{max}}{P_0}$ , where  $P_0$  is peak power for wavelength 1064 nm.

### 4.3 Nonlinear effect for different fiber lengths

The nonlinear-optical response of the fiber is shown in Fig. 4.2 where we present the spectrum emerging from the center core when the pump is launched into the center core. We observed a FWM happening near a wavelength of 1064 nm for 5-m and 47-m long fiber at suitable different powers. The spectra emerging from the side cores under the same launch conditions are similar in width and shape. The spectra for both the short (5 m in Fig. 4.2(a)) and long (47 m in Fig. 4.2(b)) show the broadening of the spectrum of the pulse train due to self-phase modulation and phase matched FWM. In both cases the overall

width of the spectrum increases dramatically as a function of power, but we easily recognize the growth of FWM peaks at about 1049 nm and 1079 nm in the 5-m case. Cascaded FWM peaks arise as the peak power exceeds 220 W, and a continuum follows for higher powers. In Fig. 4.2 (b) it is difficult to discern the FWM peaks for the 47-m long fiber but broadening into a continuum is readily observed. We observed the similar broadening for the light emerging out of other side cores when light is launched in central core in case of both short and long pieces of fiber. Since the dispersion length is about  $8 \pm 1$  km, the GVD has no significant role in pulse broadening.

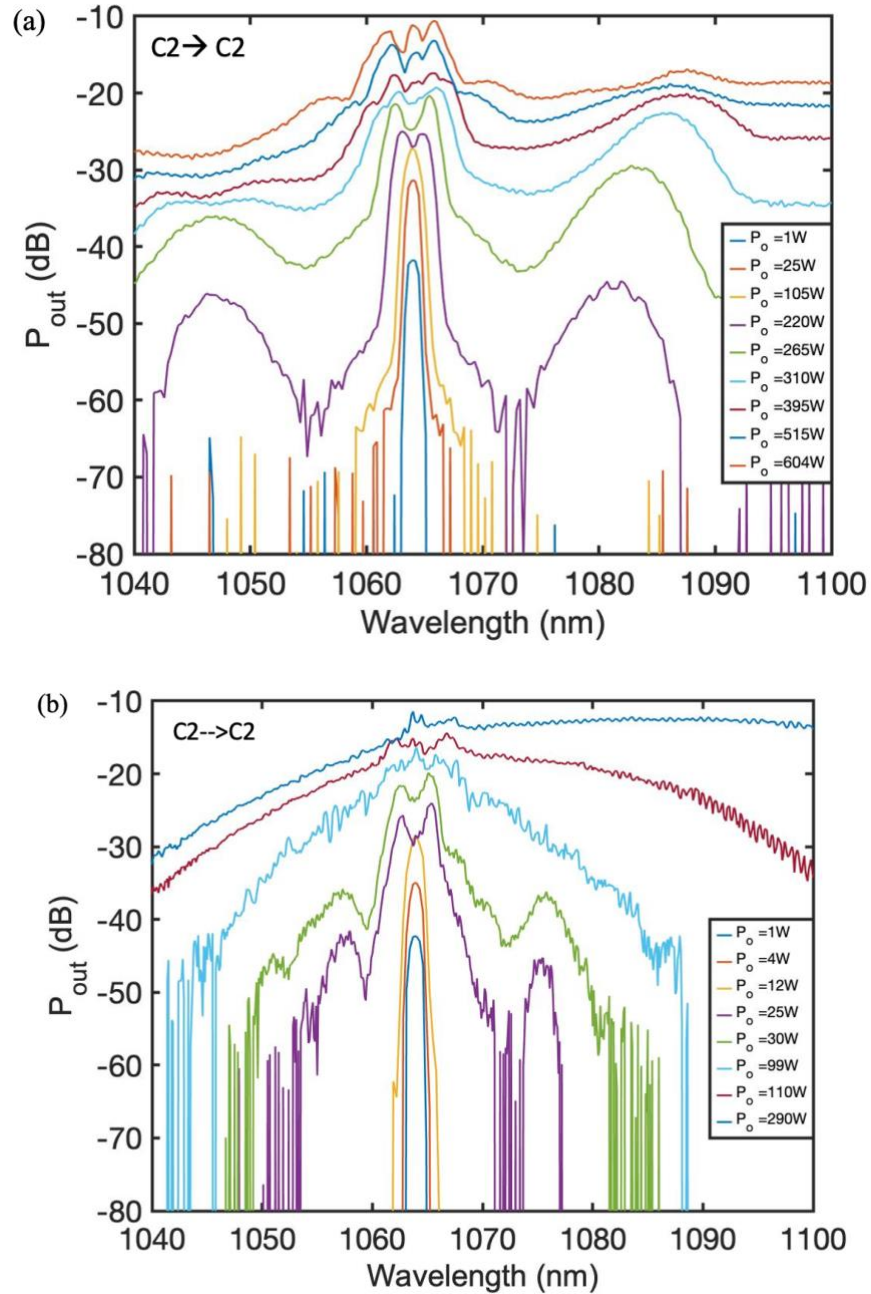




Fig. 4.2. Spectra showing the pulse broadening at various high power for different fiber length (a) short length (5m) and (b) long length (47m) [2]. The effect of fiber nonlinearity is more on the longer fiber piece. Spectra are shifted up by some units to make them look distinct in both (a) and (b). In (a) Spectra show spontaneous FWM in the 5-m long fiber where the phase-matched peaks arise at 1049 nm and 1079 nm and (b) shows the same measurement for a 47-m long fiber. The first-order FWM peaks are located at 1061 nm and 1067 nm which are not distinct in (b). FWM peaks are clearly observed when OSA resolution was increased.

We observe substantial pulse broadening as a function of power for wavelengths ranging from 1064 nm up to 1550 nm and which scales the same as that for a single core standard fiber as explained in [8]. Nonlinear coupling is not evident in our experiment.

A similar analysis can be applied to the measurements recorded near 1120 nm for the fiber length of 5-m and 1460 and 1520 nm for the fiber length of 52 m. In contrary to the broadening at 1064 nm, spectral measurement at longer wavelengths using a femto-second pulse has significant effect of GVD since the dispersion length is much less than the fiber's physical length. The observed pulse broadening in Figs. 4.3 and 4.4 is the effect of SPM.

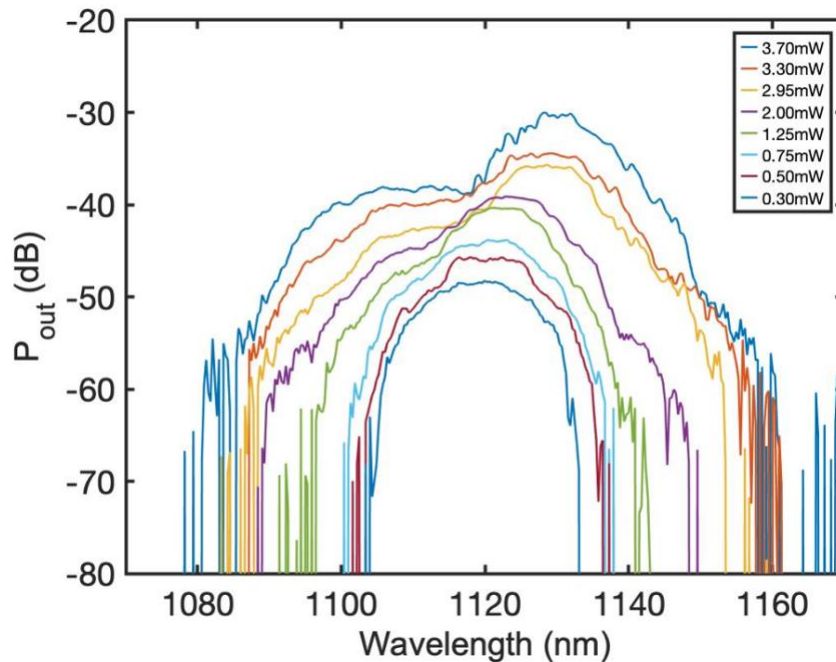


Fig. 4.3. Spectra showing the broadening of the pulses at wavelengths near 1120 nm when input power is increased. Legend is the average power measured at the fiber output end. The corresponding input peak powers are 230W, 205W, 185W, 125W, 75W, 50W, 30W, and 20W. Light is incident in one of the side cores for a 5-m long fiber piece.

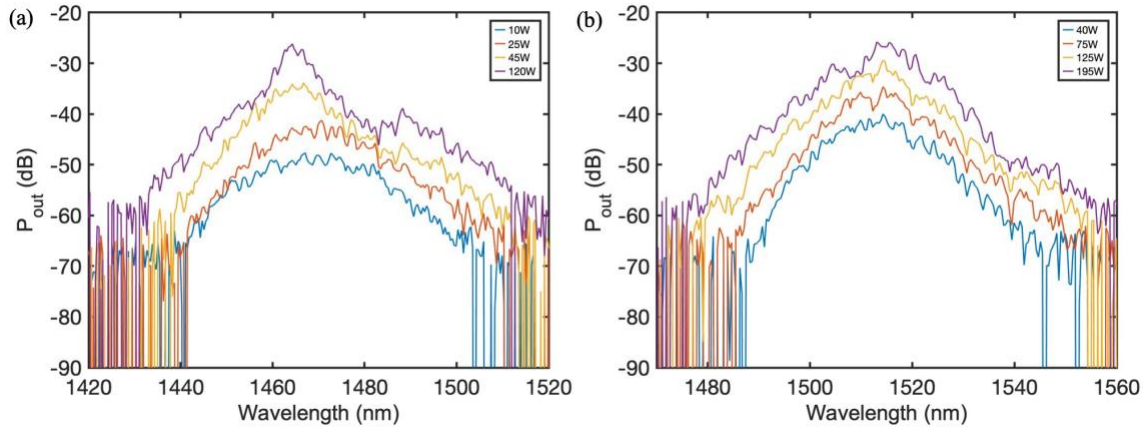


Fig.4.4. Spectra showing the broadening of the pulses at wavelengths near 1460 and 1510 nm. Light is incident into the central core of a 52-m long fiber piece.

#### 4.4 Mode coupling as a function of high power

The study of mode coupling done at low power in chapter 3 neglects the effect of fiber nonlinearity. We extend the work to consider the effects of fiber nonlinearity on the mode coupling by launching pulses with higher peak power. The experimental setup is same as described in Fig. 3.7. We inject light into a single core and observe the distribution of the output power among the 3 cores. We launch 8-ps pulses from a mode-locked Time Bandwidth Nd-Vanadate laser at a wavelength of 1064 nm into a 5-m long. Figure 4.5 shows the transfer of energy among the cores for light launched into one of the side cores, the central core, and the other side core, respectively. Since the cores are widely spaced and arranged in a line, there is only meaningful coupling between cores which are adjacent with one another. Again, we observe that the coupling between the central core and each of the side cores is not the same and so  $\kappa_{1,2} \neq \kappa_{2,3}$ . Moreover, we observe that the coupling between cores varies slightly as a function of pulse power. In figure 4.5(b), when central core is excited, we observed that the side cores are differently coupled to the central core and therefore, we observed that exciting one of the side cores (3<sup>rd</sup> core) makes the relative output power higher in the launched core while the significant amount of power transfers to the central core (core 2) compared to when another side core (core 1) is excited. We observed that almost 80% of energy emerges from one of the side cores when light is launched in that core while more than 80% of energy emerges from another side core. We also observed that launching light in central core can only yield around 70% light emergence from that core. These results obtained for input peak power ranging 0-100 W at a wavelength of 1064 nm contradicts with the similar power measurement at low power. The mode coupling seems to be slightly affected when input peak power is above 50 W indicating that it may be affected by higher input power.

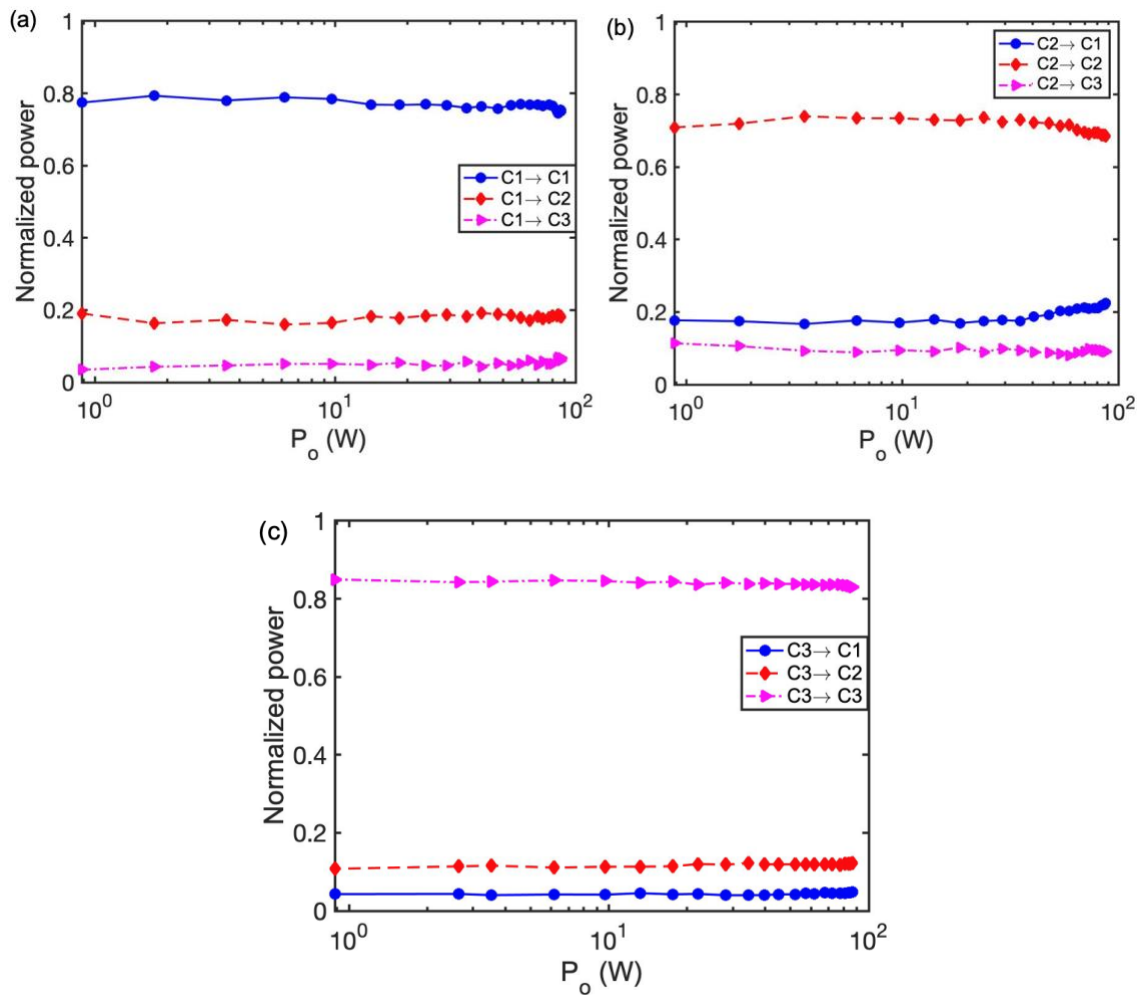


Fig. 4.5. Transfer of energy among cores in a 3-core fiber at intermediate power range when light is launched into (a) side core (core1) (b) central core (core2) and (c) another side core (core3) respectively.

To further observe if higher power affects the mode coupling, we increase the input peak power up to 600 W. Figure 4.6 is the output power measurement made for higher input power. The graphs show that the coupling of energy above a peak power of approx. 100 W is influenced by high power. Figure 4.6(b) shows plots of the normalized output power as a function of input power for coupling from the center core, C2, to each of the side cores, C1 and C3. In Fig. 4.6(b), we observe that the coupling coefficients between the central core and each of the side cores (as depicted in Fig. 3.6(d)) are not equivalent,  $\kappa_{12} \neq \kappa_{23}$ . For the 5-m long fiber, the coupling between the central core and the two side cores are about 10% and 20% with an average of 15% when measured at low powers. Assuming the coupling fraction to be  $T = \sin^2(\kappa L)$ , and the coupling length to be  $L_c = \frac{\pi}{2\kappa}$  we obtain an

average coupling length of  $L_c = 20\text{ m}$  for a wavelength of 1.064 nm. Observations of the coupling between cores for fiber lengths of 35 cm, 5 m, and 50 m are consistent with  $L_c = 20\text{ m}$ . Our observations of core-to-core coupling during low-power, linear propagation are consistent with those shown for in a similar triple-core PCF in [53]. In the case of [53], they also observed asymmetric coupling. We do, however, observe a different power-dependence than that observed in [53]. We find in our measurements that the coupling increases with power. We observed similar coupling of about 20% with the adjacent core when light is launched into side cores as in Fig. 4.6(a) and (c). Mode coupling due to two side cores excitation indicates that the coupling of light energy in lowly coupled cores is more influenced compared to the coupling in highly coupled cores. This can also be seen with the central core excitation that more energy is shared with the core 3 compared to core 1 which is highly coupled to central. However, the linear mode coupling may also significantly increase the nonlinear distortion as mentioned in [57].

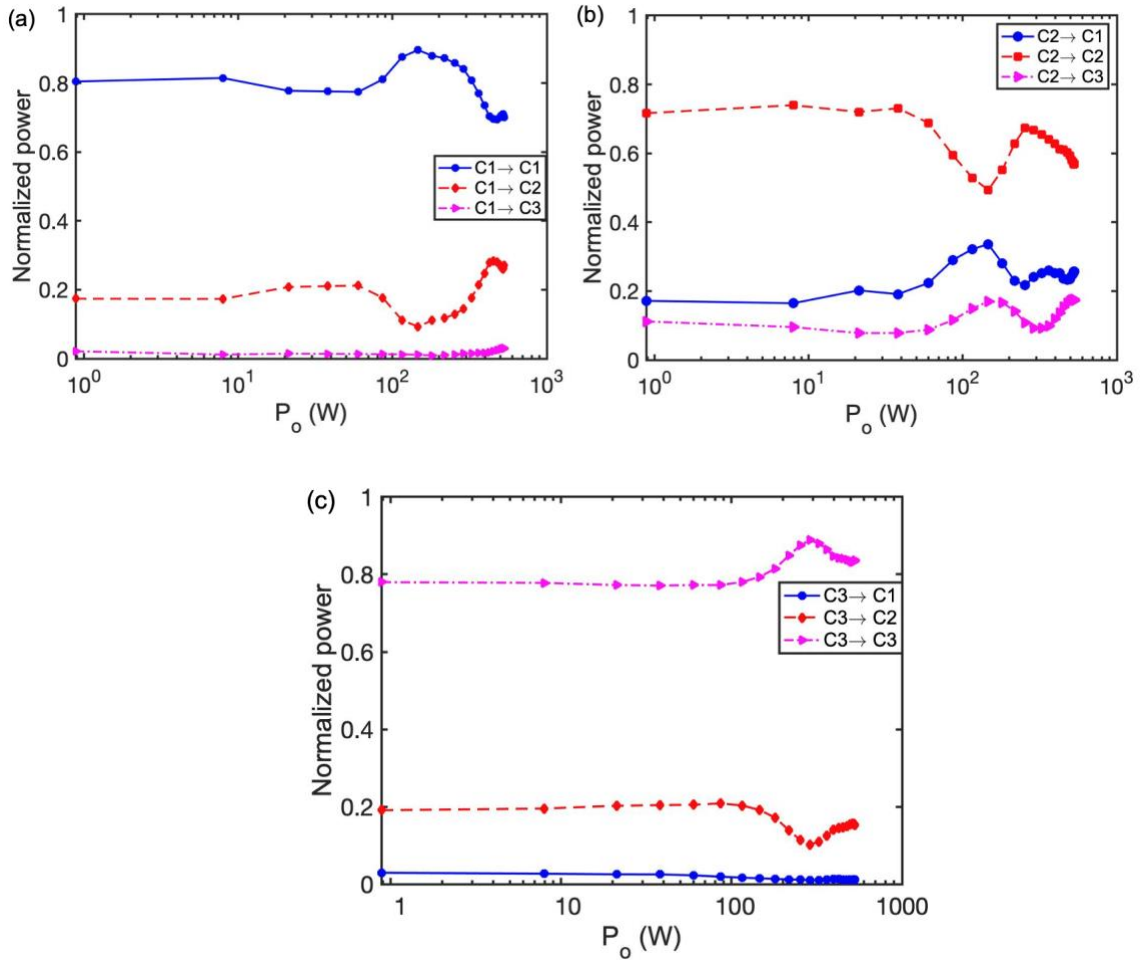


Fig. 4.6. Transfer of energy among cores in a 3-core fiber at high power upto 650 W of peak power when light is launched only into (a) side core (core1) (b) central core (core2) and (c) another side core (core3) respectively.

## 4.5 Estimation of fiber parameters from FWM curves

A detailed description of the four-wave mixing in a 3-core microstructure fiber is in chapter 6. The FWM gain curve depends on the chromatic dispersion, zero-dispersion wavelength and the nonlinear coefficient of an optical fiber. For the different fiber lengths, we can record the FWM curves and choose appropriate values for the dispersion and nonlinear coefficient of a fiber. We can then fit the experimentally observed gains with the numerical simulations to determine the group velocity dispersion (GVD) and SPM parameter of the 3-core fiber. In chapter 3, we have determined the value of GVD at different wavelengths. We determined the GVD to be  $+36 \text{ ps}/(\text{nm km})$ ,  $+41 \text{ ps}/(\text{nm km})$  and  $+9 \text{ ps}/(\text{nm km})$  at wavelengths of 1550 nm, 1315 nm and 1120 nm respectively. In a prior work as mentioned in section 4.2, we determined the fiber nonlinearity to be  $13 \pm 3 \text{ W}^{-1} \text{ km}^{-1}$ . Here, we will estimate them from the FWM gain curve at a wavelength of  $1064 \text{ nm}$  and compare with experimental results.

We observed four-wave mixing happening in two different fiber lengths at a wavelength  $1064 \text{ nm}$ . Figure 4.7 shows the measured optical spectrum (for constant  $P_0 L \sim 1 \text{ kW} \cdot \text{m}$ ) at the onset of spontaneous FWM plotted along with the calculated gain spectrum [6, 58]. In Fig. 4.7(a) the gain is calculated for the experimental pump power for reasonable choices of the group velocity dispersion,  $D$ , and nonlinear coefficient,  $\gamma$ . The peak of the gain matches with the peak of the FWM data. In Fig. 4.7(b), we choose  $D$  to remain the same because we do not expect the overall dispersion to change with core-to-core coupling. Since the fiber's physical length is now longer than  $L_c$ , we expect to be able to observe FWM for the case where the nonlinear length extends beyond  $L_c$ . We replace  $\gamma$  by  $\frac{\gamma}{3}$  and the calculated curve now produces narrow peaks which match the data well. The key hypothesis formed from the previous analysis is that when FWM occurs in multiple cores,  $\gamma$  is effectively reduced by a factor of 3. Note that since we have fixed  $P_0 L$  in Fig.4.7, we find that changing the power is not sufficient to explain the peak locations in the observed spectra. The effective nonlinearity,  $\gamma$ , must change as well.

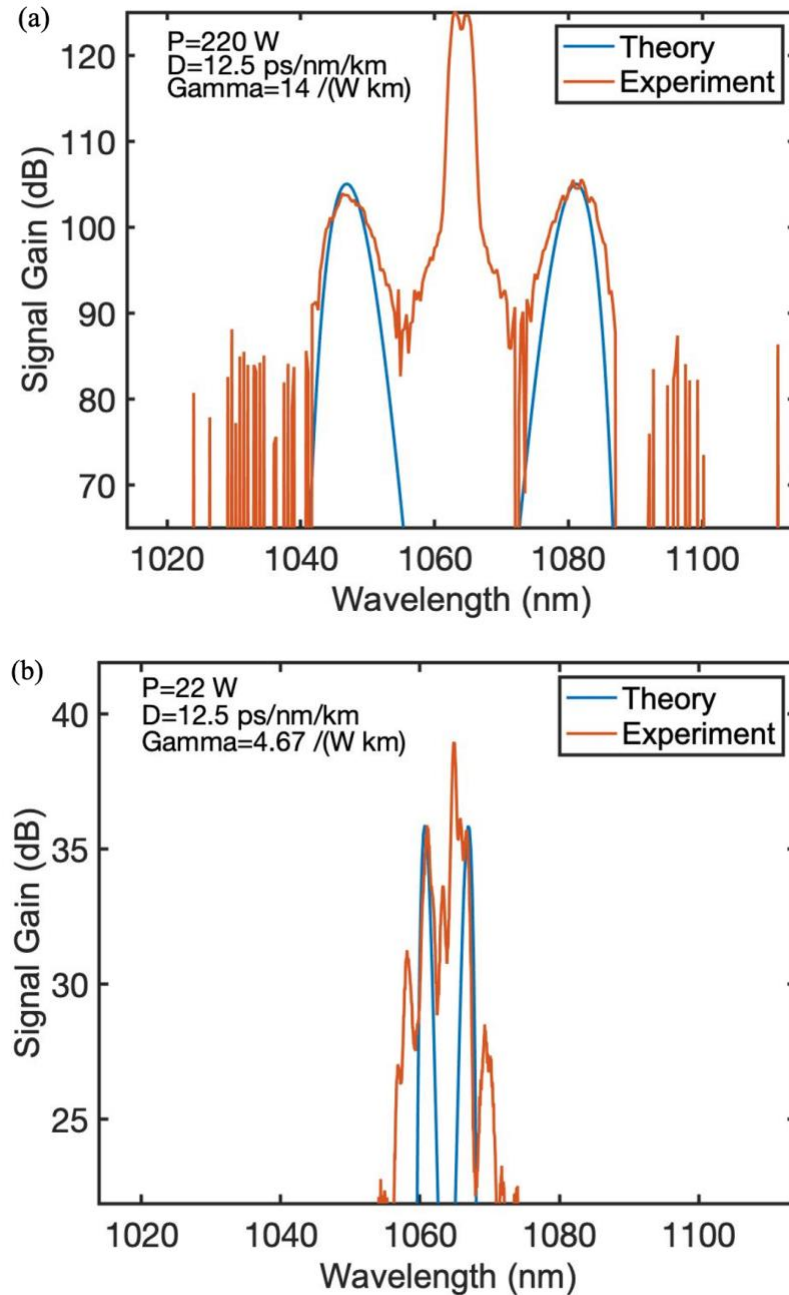


Fig. 4.7. FWM gain. (a) short fiber piece (4.9m) (b) long fiber piece (47m) [2]. The estimated values of  $\gamma$  are 14 and  $4.67$   $W^{-1}km^{-1}$  for short and long fiber pieces respectively [2].

We confirm our hypothesis about the interplay between  $\gamma$ ,  $P_0$  and  $L$  by measuring the spectral broadening due to self-phase modulation (SPM) of the pump pulses, as shown in Fig. 4.8. An estimate of  $\gamma$  is obtained [8] from the slope of width vs. power graph according to

$$\delta\omega_{max} = 0.86\Delta\omega_o\varphi_{max} \quad (6.9)$$

where,  $\delta\omega$  is the SPM-induced frequency broadening,  $\Delta\omega_o$  is the initial spectral width and  $\varphi_{max} = \gamma P_o L_{eff}$  is the maximum phase shift.

In terms of the wavelength and slope, the above equation is modified to estimate the value of SPM parameter as,

$$\gamma = 1.1628 \frac{slope}{\Delta\lambda_o L_{eff}} \quad (6.10)$$

where,  $\Delta\lambda_o$  is the spectral width of the unbroadened pump, and  $L_{eff}$  is the fiber's effective length. Slope and  $\Delta\lambda_o$  are measured with a linear fit in nonlinear and linear power regime respectively as mentioned in figure 4.8. Figure 4.8 shows an evaluation of the width of the central peak as a function of the peak power, wherein the 6-dB width was used to mitigate the effects of noise near the peak of the spectra.

The peak power  $P_o$  is calculated considering the fiber's efficiency as

$$P_o = 0.94 * \frac{P_{avg}}{R.R \times \Delta t} * fiber\ efficiency. \quad (6.11)$$

For short fiber and long fiber pieces, the fiber efficiency is measured to be 55% and 25% which are a little less than the maximum fiber efficiency we can achieve with fine alignment.

In Fig. 4.8(a) we see that the spectrum broadens in all 3 cores as expected in a linear fashion below about 100 W with the energy splitting to some extent among the cores. The rate of SPM induced broadening (the slope of the curve) increases in the central core when power exceeds about 100 W. Above 100 W,  $L_{NL} < L_c$  and the slope is determined by SPM arising from propagation in a single core leading to  $\gamma \approx 14 \pm 1 (W km)^{-1}$ . Below 100 W,  $L_c < L_{NL}$  and the result is  $\gamma \approx 5 \pm 1 (W km)^{-1}$ . Light emerging from the other two side cores also exhibit the relatively small  $\gamma$ .

Figure 4.8(b) illustrates the same SPM broadening experiment performed on a 47-m long fiber. In this case the physical fiber length is greater than the coupling length, and  $L_c < L_{NL}$  and we again obtain the result of  $\gamma \approx 5 \pm 1 (W km)^{-1}$ . As the peak power is increased from 6 W to 30 W, SPM combined with FWM leads to an increasing number of peaks in the spectrum. Specifying broadening due to SPM for powers larger than about 30W is obscured by FWM peaks which arise close to the pump's spectral envelope. The detail of finding slopes at linear and nonlinear regimes is illustrated in Fig.4.9.

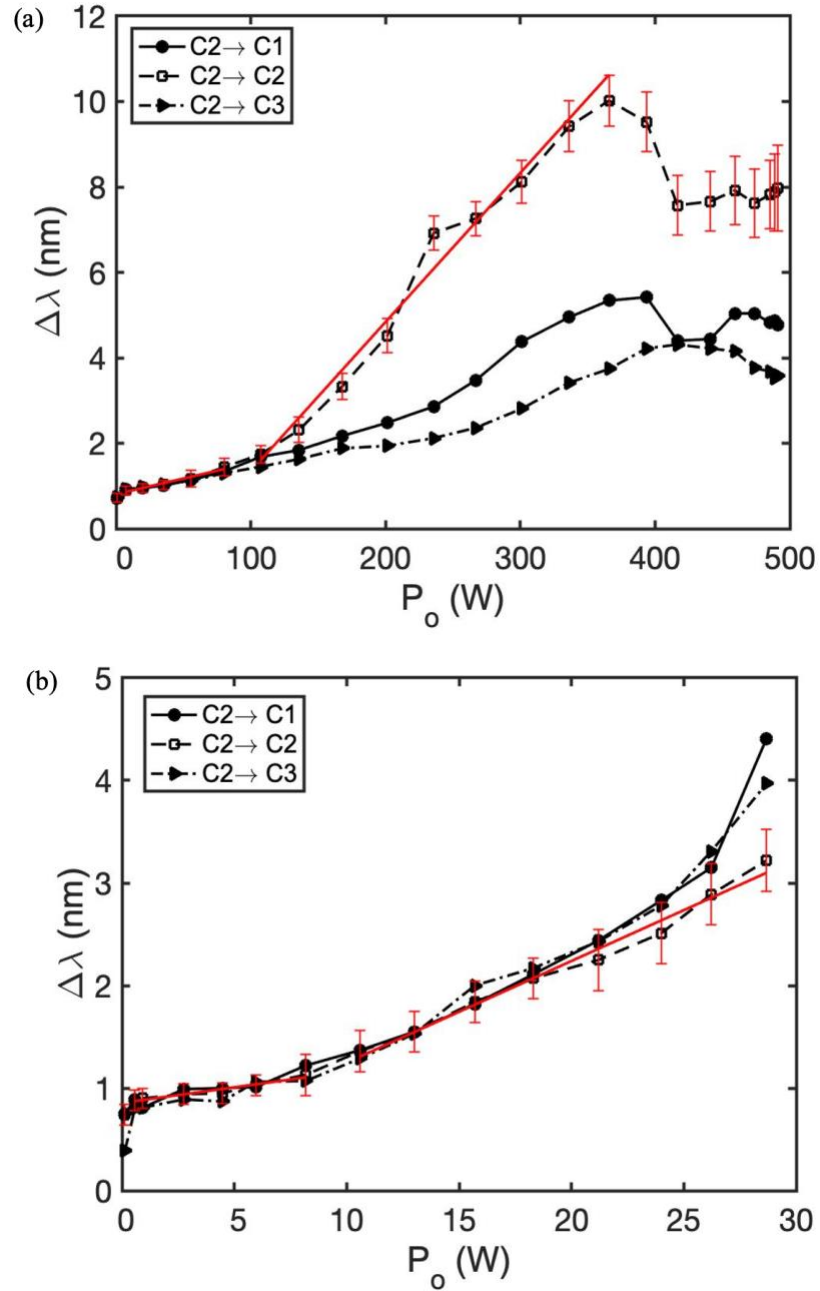


Fig. 4.8. Spectral broadening measurement as a function of input power when central core is excited. (a) for short fiber (4.9 m) and (b) for long fiber (47 m) [2]. Straight line (red) is the linear fit for linear and nonlinear power regimes in (a) and (b). The slope of the line in nonlinear power regime is 0.04 (for (a)) and 0.12 (for(b)). The value of  $\Delta\lambda_0$  is 0.80. We observed that the spectral broadening is solely due to the fiber SPM parameter and is significant above 100 W [2].



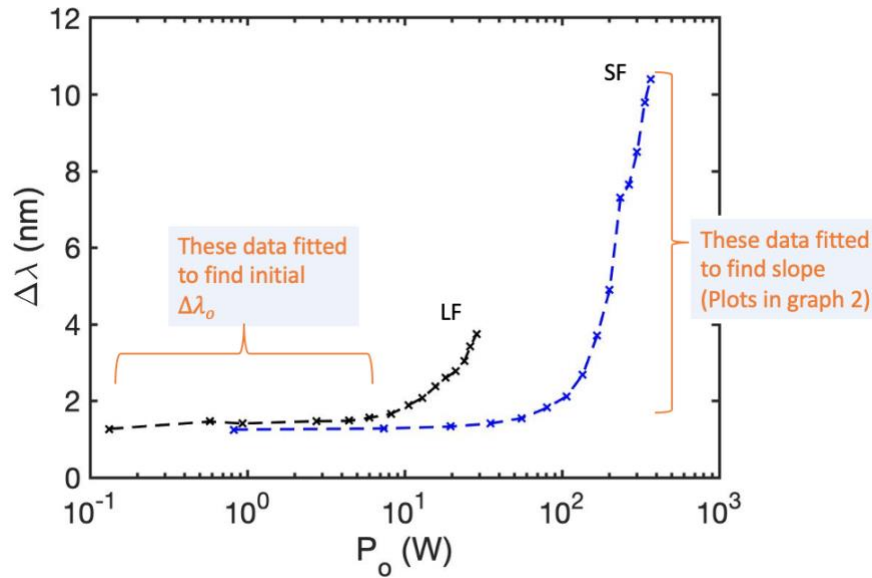


Fig. 4.9. Spectral broadening measurement as a function of power for long and short fiber pieces showing the data range (orange) for finding initial spectral width and slope. Data points in the linear regime are chosen and fitted to find  $\Delta\lambda$  corresponding to  $P_0 = 0$ . Data points in the nonlinear regime are chosen to find the slope.

**Table 4.1: Value of SPM parameter**

Parameter in equation (6.10)	Long fiber	Short fiber
slope	0.12	0.04
$\Delta\lambda_0$	0.80	0.80
Fiber length	47 m	4.9 m
Estimated $\gamma$	$3.70 \text{ W}^{-1}\text{km}^{-1}$	$11.9 \text{ W}^{-1}\text{km}^{-1}$

These are in good agreement with numerical simulation and experimental plot in figure 4.7.

## 4.6 Summary

In this chapter, we discussed the various spectra observed at high power beam propagation over a wide range of wavelengths. We presented the origin of nonlinear phenomenon associated with an optical fiber. We presented the various spectra showing the effect of GVD and nonlinear parameters at wide range of high power at different wavelength

ranging in  $1.064 \mu\text{m} - 1.60 \mu\text{m}$ . We also observed substantial pulse broadening as a function of power for wavelength ranging from 1064 nm up to 1550 nm. The linear relationship between broadening and the input power tells that the broadening is due to the SPM parameter of the fiber and may have no role in the mode coupling. We also found a significant difference in the pulse propagation for short and long pieces of fiber and described them in terms of the fiber's dispersion length and nonlinear length. We investigated the coupling characteristics of a 3-core fiber in a nonlinear approximation using mode locked pulsed light and found that mode coupling is significantly affected by an intense pulse. We utilized the four-wave mixing spectra observed at  $1.064 \mu\text{m}$  to validate our experimental measurements for dispersion and nonlinearity of optical fiber. The key point is that when FWM occurs in multiple cores, fiber's nonlinearity is effectively reduced by a factor of 3 (number of cores). By adjusting the pump power for a fiber whose physical length is slightly longer than the coupling length we observe the transition between single-core nonlinear effects and multi-core nonlinear effects. The critical design challenge is balancing the effective nonlinearity with the desired phase matching bandwidth. If the coupling length is short compared with the nonlinear length, then the effective nonlinearity,  $\gamma$ , is reduced by the number of cores present. While this increases the maximum power at which one can operate the FWM device, it reduces the phase matching bandwidth. A careful analysis of the spectra at wavelength range  $1.064 \mu\text{m} - 1.60 \mu\text{m}$  aids in understanding the combined effects of various linear and nonlinear effects allowing the fiber to be implemented in signal transmission in the telecommunication and medical field.

## CHAPTER 5

### OPTICAL PARAMETRIC OSCILLATOR USING NON-POLARIZATION MAINTAINING MICROSTRUCTURE FIBER

Fiber optical parametric oscillators (FOPOs) are attractive as they can provide a large gain over a large range of wavelengths. Key concerns with FOPOs are the tunability it offers and power limitations. Much research had been done to obtain higher gain and power in degenerate and nondegenerate modes. Xu *et al.* designed a tunable FOPO with multi-watt output power using a dispersion shifted fiber [59]. Murray *et al.* used a seed source to optimize the power from a tunable FOPO while Jin *et al.* optimized the output power from the FOPO with high output coupling ratio close to 1 [60, 61]. Fiber optical parametric oscillator design mostly involves the use of dispersion shifted fiber and tailoring pump wavelength. Since, FWM is a polarization dependent process, we utilized the effect of the field's polarization in the output coupling to optimize the FOPO performance. In this chapter, I extend the study of the polarization-based scheme for the FOPO power measurement carried out initially by Thomson Lu and Leily Kiani. Beforehand, we introduce FOPO and FWM necessary to understand the parametric amplification in a microstructure fiber.

#### 5.1 Historical review of FOPO

With the invention of the laser as a coherent and monochromatic source of light, researchers were interested in increasing the range of wavelengths available. The first broadly wavelength-tunable laser was the dye laser in 1967 [62]. Several types of tunable lasers were invented in the later decades, however the range of tunability was limited and there were gaps in the visible and near to mid IR region. Within five years of invention of laser, Joseph A Giordmaine and Bob Miller demonstrated the first ns-pulsed optical parametric oscillator in 1965 at Bell labs using LiNbO<sub>3</sub> crystal as an alternative and reliable source of coherent light with a wide range of tunability [63]. They observed parametric oscillation in the wavelength range of 0.97-1.15  $\mu\text{m}$  with optical pumping at a wavelength of 0.529  $\mu\text{m}$ . In the same year, Wang and Racette discovered that coherent light can be

generated at the difference frequency between two pump beams propagating through a non-linear crystal [64]. The standard optical parametric oscillator is based on the 2<sup>nd</sup> order susceptibility of the material of crystal. It provides an optical beam with relatively high spatial and temporal coherence and a wide range of wavelength tunability compared to a tunable laser. OPOs work well in most of the spectral regions like UV, visible, near infrared and mid-infrared regions some of which are inaccessible by any laser.

R H Stolen demonstrated the first optical parametric amplifier in a low loss fiber in 1975 [65]. The pulsed fiber based OPO was first demonstrated in late 1980s. The pump source was a CW color-center laser with a wavelength of 1.5  $\mu\text{m}$ . The pulse width and repetition rate were 13 ps and 100 MHz respectively. A FOPO with high gain and wide spectral bandwidth is a viable alternative source of light. In 2002, the first microstructure fiber based OPO was demonstrated by J.E. Sharping et al. using a Ti:Sapphire laser with a repetition rate of 75 MHz and pulse duration of  $630 \pm 10$  fs at FWHM [58]. Fiber optical parametric oscillation is a non-linear phenomenon based on the 3<sup>rd</sup> order susceptibility of the material. In a parametric amplification process, a signal wave is amplified using a pump wave and a parametric non-linearity. The gain bandwidth increases with the increase in pump power. FOPOs are widely used in optical signal processing, pulse generator, wavelength conversion, de-multiplexing, optical time division and others. Fiber parametric devices are also attractive in high-speed optical communication systems.

## 5.2 Four wave mixing process

FWM is a third order optical non-linear process that involves an interaction among three waves giving rise to fourth wave of different frequency. Two pump waves of frequencies  $\omega_{p_1}$  and  $\omega_{p_2}$  combine together and generate idler and signal waves of frequencies  $\omega_i$  and  $\omega_s$  respectively satisfying conservation of energy and momentum equations.

$$\begin{aligned}\omega_{p_1} + \omega_{p_1} &= \omega_i + \omega_s \\ \beta_{p_1} + \beta_{p_1} &= \beta_i + \beta_s\end{aligned}\tag{5.1}$$

For a degenerate four wave mixing process (the two pump waves being identical), the frequencies of the output waves are related to the pump frequency by the relation

$$2\omega_p = \omega_i + \omega_s\tag{5.2}$$

The new waves of lower and higher frequencies are also called Stokes and anti-Stokes waves. Fig. 5.1 illustrates the mixing of two pump waves for the degenerate case giving rise to two new waves satisfying energy and momentum conservation law. Signal and idler wave are generated from noise when a phase matched condition is satisfied. The

wavelengths of generated waves are determined by the pump wavelength and the dispersion profile of the fiber.

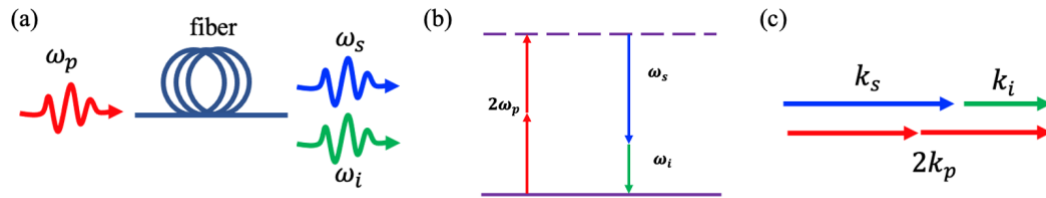


Fig. 5.1. Generation of two new frequencies in a degenerate FWM process from a pump frequency. (a) FWM process (b) Energy level diagram (c) Phase matching diagram

### 5.3 Polarization in a birefringent fiber

As mentioned in section 1.1 in chapter 1, a fiber can support a single mode depending on the fiber parameter under a perfect symmetry. But in reality, a fiber may have a small perturbation on its symmetry causing it to exhibit two polarization modes in orthogonal directions having a small difference in their effective refractive indices  $n_x$  and  $n_y$ . A fiber exhibits some modal birefringence due to a slight difference in the mode propagation constant for modes in  $x$ - and  $y$ - directions. The modal birefringence is determined by a dimensionless parameter

$$B_m = \frac{|\beta_x - \beta_y|}{k_o} = |n_x - n_y|. \quad (5.3)$$

The birefringence of the fiber modifies the polarization state of the input light. In case of a polarization maintaining fiber (fiber with high birefringence), the birefringence is uniform and linear while in a non-polarization maintaining fiber, it is random causing a random change in the SOP of the input light. The coupling between the two modes can be measured in terms of a beat length as

$$L_b = \frac{2\pi}{|\beta_x - \beta_y|} = \frac{\lambda}{B_m}. \quad (5.4)$$

The beat length is the fiber length over which the initial polarization state of light is recovered. The beat length is small for a high birefringence and vice-versa.

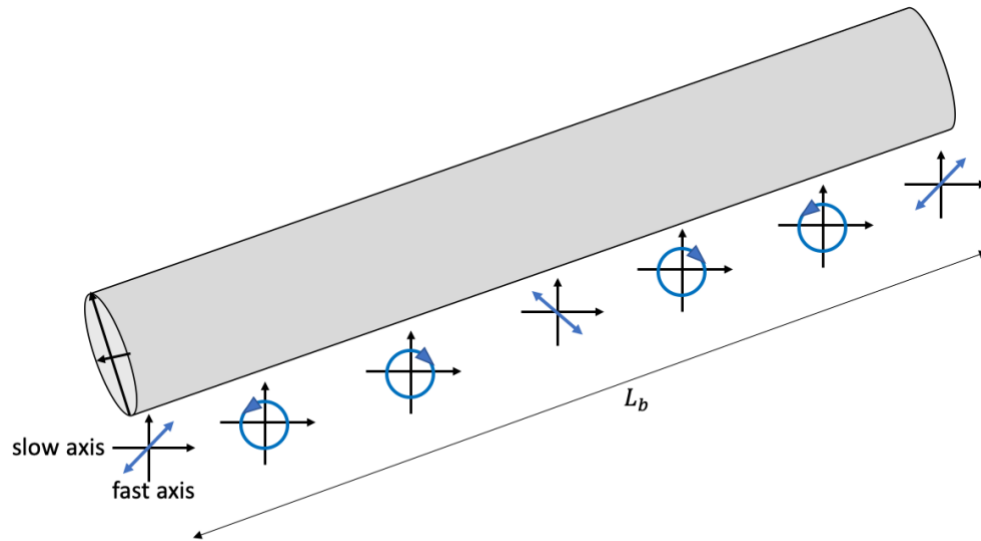


Fig. 5.2. Evolution of the polarization state of light along a uniform birefringence fiber for a linearly polarized light at  $45^\circ$  with the slow axis. Reprinted from [8].

In a non-polarization maintaining fiber, the modal birefringence changes randomly along its length inducing the pulse broadening which is also called polarization mode dispersion (PMD).

For a FOPO system, the PMD randomizes the polarization state of the fields in the cavity. This is due to the fact that the FWM process involved in a FOPO system is a polarization dependent. It has been observed that the states of polarization of fields rotate in the same direction on the Poincare sphere and state of polarization (SOP) of individual field varies depending on their frequency difference [8]. The change in the SOP of difference wavelengths (signal, pump and idler) is different due to PMD. It is assumed that the FOPO gain will be maximum when the fields polarization overlap. The PMD effect is small and can be neglected for a fiber length smaller than 100 m.

In addition to the modal birefringence, a fiber may have nonlinear birefringence induced by an intense pulse. While considering the polarization effect at high power, one must include both modal and nonlinear birefringence for an accurate description. The evolution of the state of polarization of light in an optical fiber can be described based on the Stokes vector rotation on the Poincare sphere.

## 5.4 Polarization-based scheme for FOPO

There are several designs and proposed models for the optimized performance of FOPOs [59-61]. Their methods do not consider the effect of the polarization in the output coupling. We study the polarization orientation of fields in the FOPO cavity and include its effect on the maximum gain. In this section, I will also discuss the prior work done in this experiment. In this experiment, at the output end of the fiber, we employ a polarization-based output coupling method in which a combination of half wave plate (HWP) and polarization beam splitting cube (PBS) is introduced in the cavity that helps in controlling the polarization state of the fields in the cavity.

We optimize the FOPO system by tuning either the signal in the range of 991-994 nm or the idler in the range of 1146 to 1150 nm. Amplification of the signal field and the generation of the idler field occur when the pump field interacts with the feedback field in the optical cavity of the system. The polarization state of the fields in the cavity is controlled with the HWP2 and HWP3 and a fiber polarization controller (FPC). HWP2 can be used to adjust the polarization state of the pump at the fiber input if needed. The polarization state of the output field can be controlled with HWP3 and the FPC. We also initially adjust HWP2 and FPC to maximize the coupling of the pump into the fiber.

The PBS reflects vertically polarized (s-polarized) light and transmits horizontally polarized (p-polarized) light. The transmitted light is fed back into the cavity with the help of adjustable end mirror M3 and its polarization can be change with HWP3. Thus, the coupled output power can be optimized by both the output coupling ratio and the polarization mode overlap of the counter propagating light in the optical cavity. As a result, the coupled output power obtained from the FOPO system can be optimized by controlling the polarization overlap and power coupled out of the system using FPC and HWP3.

### 5.4.1 Experimental set-up

A schematic of the experimental setup for the FOPO is shown in Fig. 5.3. It consists of a Fabry-Perot cavity with a fiber and free space in it. The fiber is 1.2-m long non-polarization maintaining microstructure fiber (NKT Photonics, NL-5.0-1065) and is pumped by a mode-locked Nd:Vanadate laser emitting pulses at a central wavelength of 1064 nm. The laser produces pulses with duration of 8 ps and with peak power of 1250 W at a repetition rate of 80 MHz. A maximum of 550 mW of average pump power was coupled into the fiber. The pulse emitted from the laser is assumed to be linearly polarized which is then coupled to the fiber using a lens with a suitable numerical aperture. An isolator is placed on the beam path to avoid a laser damage with the back reflection. A half wave plate when combined with the polarization beam splitter (PBS) works as an attenuator and controls the light intensity. Mirrors M1 and M2 help in efficient light beam coupling into fiber. The

front facet of the fiber and the end mirror M3 form a Fabry-Perot cavity which is synchronized with the repetition rate of the pump field. Wavelength tuning is done by the adjusting mirror M3. The FOPO is tunable from 960-1044 nm on the anti-Stokes side and 1084-1191 nm on the Stokes side with output pulse durations of 2.2 ps. To investigate the change in the coupled output power with the change in the polarization state of the overlapped fields in the cavity, we mounted a HWP3 on a motorized rotating stage and measured the output power. The output of all three fields were recorded on an oscilloscope for the waveform analysis.

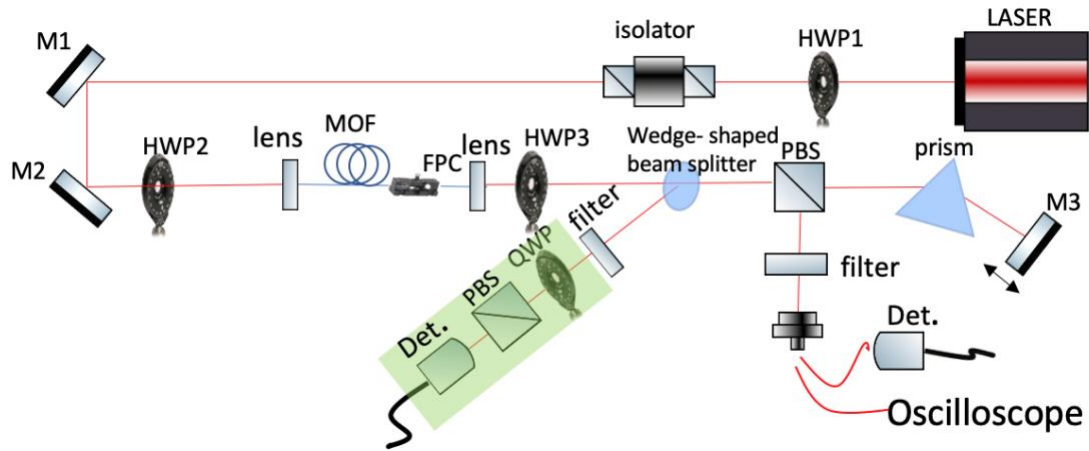


Fig 5.3. Schematic of experimental setup for polarization-based scheme for the output power measurement from a FOPO system.

### 5.4.2 Results and discussion

We measured the output power for the two different cases, low-loss and high-power cases. In the former case, we adjust FPC and HWP3 in such a way that we obtain minimum coupled output power provided that the FOPO is operational and in the latter case, we maximize the output power. Figure 5.4 is the measurement of the coupled output power when the HWP3 is rotated to change the polarization state of fields in the cavity (a) for low loss condition and (b) high power condition. We found that more power is extractable from the FOPO system at the latter case. In the figure 5.4, different labels correspond to the different stages of FOPO operating when the HWP3 is rotated.



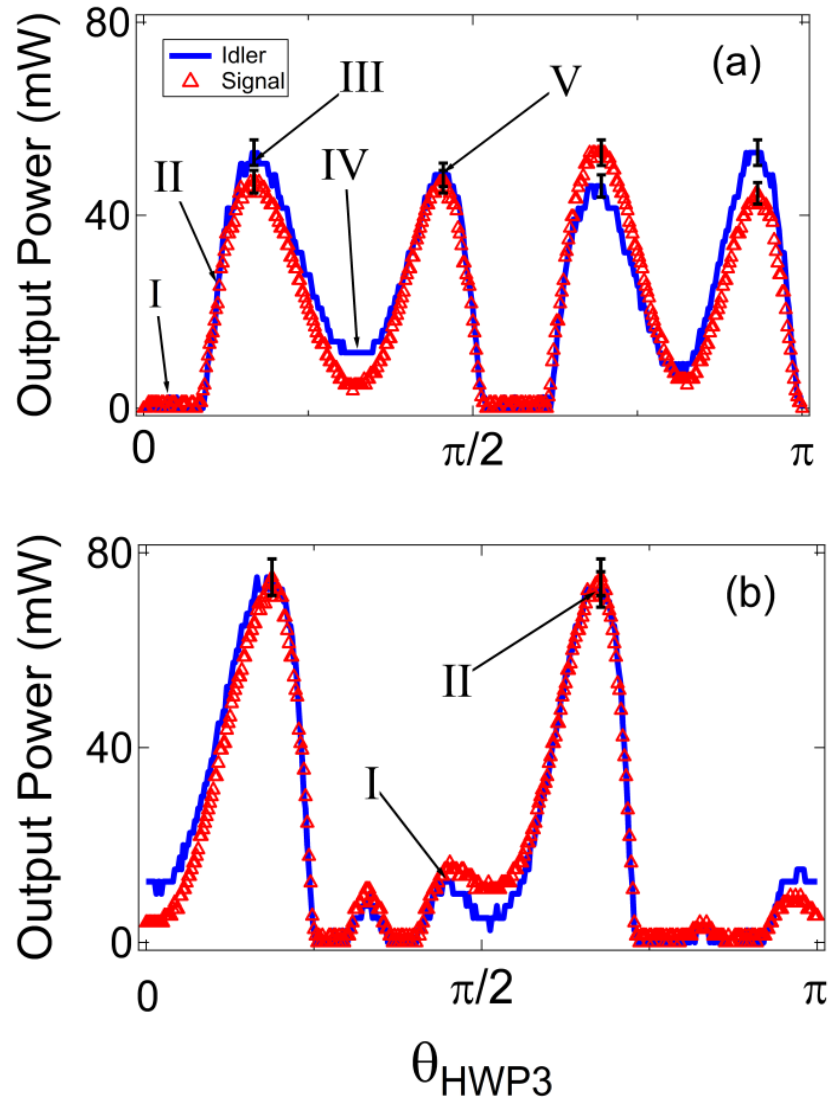


Fig. 5.4: Output power measurement in the FOPO cavity as a function of HWP angle (a) for low loss case (b) for high power case. Labels in the graph represents the different working condition of the FOPO system [66].

In Fig. 5.4 (a) labeled I region indicates that the FOPO is not operating as the power is below the threshold power due to high power loss in the cavity. As the HWP3 rotates, the threshold power is achieved at labelled section II and therefore, attains a maximum gain at III. The power then starts decreasing and reaches a minimum value at IV indicating that the power is still above the threshold with FOPO operational. With further rotation, the output power increases and attains another maximum value at V. In low loss condition, the maximum value of sideband (signal and idler) power extracted from the system is 50 mW. In Fig. 5.4 (b), the labelled regions have the similar meaning as explained in fig. 5.4(a) except the peaks are asymmetric. Label II peak is taller than the peak in fig. 5.4(a)

indicating that more is recorded in this high-power operation mode than in the low-loss mode. The output power extracted is 70 mW which is almost 30% higher than the power extracted from low loss operation mode.

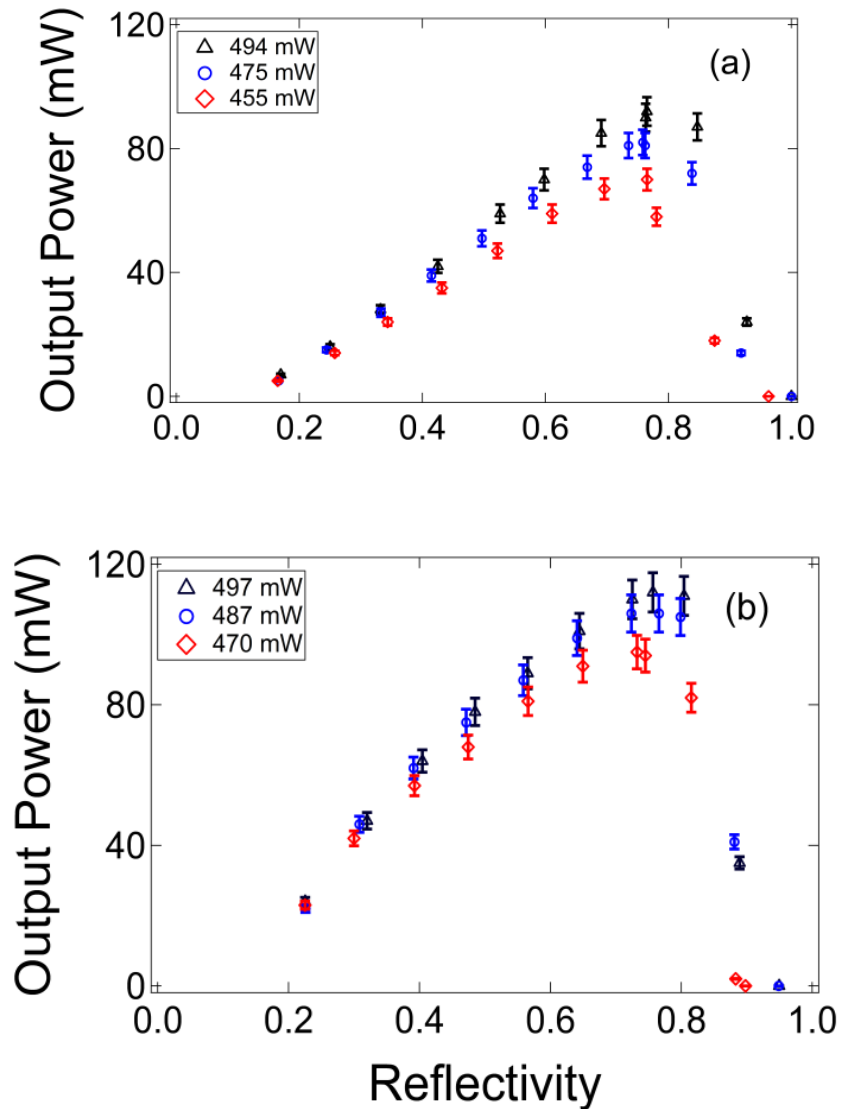


Fig. 5.5. Output power measurement as a function of output coupler reflectivity in the cavity for two different conditions (a) low loss condition and (b) high power condition at different pump power.

In figure 5.5, we see that the output power increases with an increase in the reflectivity and attains the highest value for the reflectivity of the range 0.7-0.8 and then decreases. The decrease is due to the very high coupling power causing the system to be below the

threshold. A clear distinction in figure 5.5 (a) and figure 5.5 (b) is that higher output power is obtained for the high-power condition than in the low loss condition. This illustrates that the polarization state of the field in the cavity plays an important role in optimizing the gain obtained from a FOPO system.

## 5.5 Measurement of polarization state of fields in the FOPO cavity

The experimental measurements of coupled output power at different conditions reveal that more power is extractable at high power condition. Since we implemented a polarization-based scheme for the power measurement, the increase in the power may be due to the effect of our scheme on the polarization state of light. To explain the behavior of light at both low-loss and high-power conditions with more power extraction at the latter case, it is important to investigate the polarization state of light at those schemes. We visualized the polarization dynamics in the FOPO cavity on the Poincare sphere. Stokes intensity parameters like  $S_0$ ,  $S_1$ ,  $S_2$ , and  $S_3$  are used to graphically represent the polarization state of light on the Poincare sphere.

We measured the Stokes polarization parameters for various settings of a rotating quarter wave plate (QWP) as shown in the highlighted part in figure (2) and develop the Poincare sphere to visualize the state of polarization of different fields. The QWP is placed on a motorized mount and is rotated through  $360^\circ$ , however, rotation through  $180^\circ$  is sufficient to obtain a complete set of Stokes polarization parameters. A detail of the technique used for the polarization measurement is in [67]. The intensity of the optical beam on the detector [67] is given by

$$I_n = \frac{1}{2}(A + B \sin 2\theta_n + C \cos 4\theta_n + D \sin 4\theta_n) \quad (5.5)$$

where,  $n = 1, 2, 3, \dots, N$  and  $N \geq 8$  and is even.

The coefficients A, B, C and D are determined using Fourier analysis method as

$$\begin{aligned} A &= \frac{2}{N} \sum_{n=1}^N I_n; & B &= \frac{4}{N} \sum_{n=1}^N I_n \sin 2\theta_n; & C &= \frac{4}{N} \sum_{n=1}^N I_n \cos 4\theta_n; \\ D &= \frac{4}{N} \sum_{n=1}^N I_n \sin 4\theta_n. \end{aligned} \quad (5.6)$$

The Stokes parameters are calculated by using following equations.

$$S_0=A-C \quad S_1=2C \quad S_2=2D \quad S_3=B \quad (5.7)$$

To understand the polarization behavior of the three fields in the FOPO cavity, we operated the FOPO under two polarization conditions. 1) when the loss in the cavity is minimum

(low-loss condition) which is achieved by minimizing the coupled output that is assumed to corresponding to minimum loss, 2) when the coupled output power for the sideband is maximum (high power condition). We measured the output power and polarization state of fields in both conditions. For a linearly polarized pump being launched into the fiber and if the polarization of the pump at the fiber output is completely p-polarized, then the coupled output power extracted from the system is independent of the polarization state. In Fig. 5.6 (a)-(c), we see that the pump is linearly polarized, and the output idler and signal are also linearly polarized indicating that there is no change in the polarization orientation. On the other hand, if the polarization of the pump at the fiber output is not completely p-polarized then the feedback polarization will not overlap with the fiber output polarization. We can re-orient the feedback polarization by adjusting HWP and PFC to extract more coupled output power. We extracted more power out of the system in case of the high-power condition and found that the polarization state emerging from the fiber is elliptical when the output power was maximized. These scenarios are depicted on the Poincare spheres in figure 5.6 (d)-(f) for a linearly polarized input field. We see that the polarization states of the pulses change when the adjustment was made to obtain highest coupled output power. The pulses in the cavity are either linearly polarized with  $\pm 45^\circ$  or elliptically polarized. This suggests that polarization states of pulses in the FOPO cavity must be taken into account while extracting maximum power from the system.

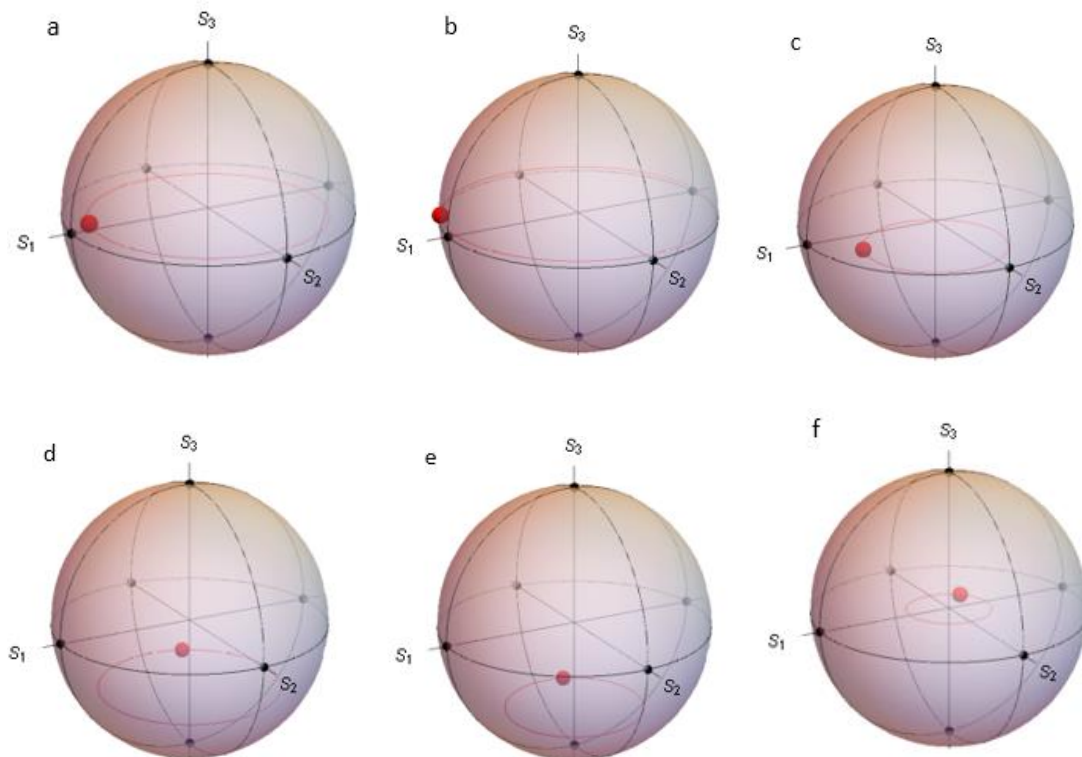
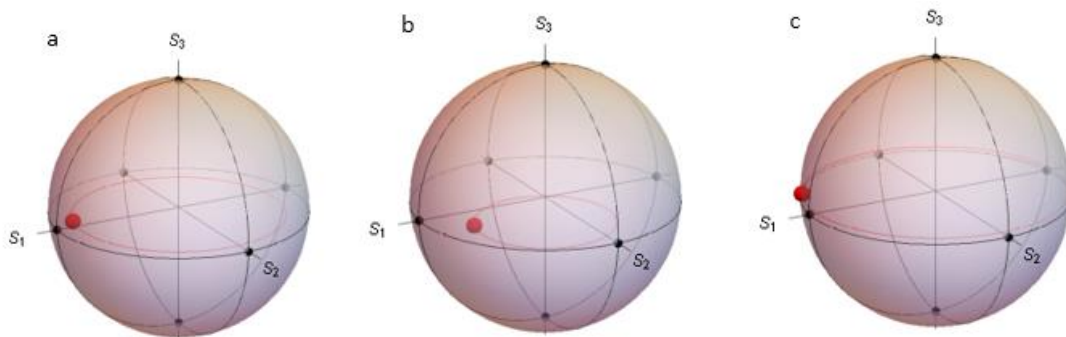


Fig. 5.6. Poincare spheres visualizing the polarization states of the fields in the Fabry-Perot cavity for two cases. (a)-(c) are for pump, idler and signal respectively when the coupled

output was minimized (low-loss case) for a linearly polarized input pulse. (d)-(f) are for the pump, idler and signal respectively when the coupled output was maximized to 45 mW (high-power case).

Further, to understand the dynamics of the polarization state of the pulses, we replaced the HWP2 with a QWP at the input of the fiber. This QWP will help in introducing an ellipticity in the input pump pulse i.e. the pump at the input of the fiber will be less linearly polarized. It is measured to have a degree of polarization of 91%. The polarization states of all fields in the FOPO cavity are measured at low-loss and high-power conditions. In figure 5, the polarization states for the different fields are depicted on the Poincare's sphere for both conditions. We see that the polarization states of signal and idler are similar to that of pump pulse at the output of fiber as shown in figure 5.7 (a-c). All are similar to the pump at the input of the fiber. However, the degree of polarization is low for the pump pulse at output compared to that at input of fiber. This affirms that the output power is independent of the polarization modes in the low-loss condition, where we minimize the coupled power to extract power from the system. In the high-power condition, the polarization states of the fields in the optical cavity are either linearly polarized with  $\pm 45^\circ$  or elliptical as shown in figure 5.7 (d-f). This is because the polarization states of the fields are reoriented with the adjustment made for the high-power condition. We repeatedly measured the polarization of fields several times by changing the ellipticity angle of the input pump for both cases and we found that fields are always either elliptically polarized or linearly polarized with  $\pm 45^\circ$  in the high-power case where more power is extractable. This suggests that in addition to the polarization state of input pulse as mentioned in [68], one needs to consider the polarization state of pulses in the cavity to obtain maximum output power from the system.



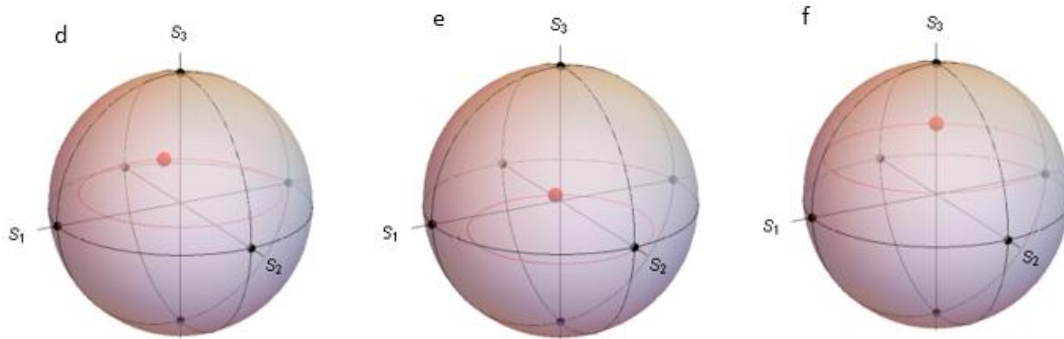


Fig. 5.7. Poincaré spheres depicting the polarization state of pump, idler and signal measured at the FOPO cavity when input is elliptically polarized for the low-loss case (a-c) and high-power case (d-f).

## 5.6 Degree of polarization as a function of wavelength

Polarization states of fields in the cavity in section 5.5 for the low loss and high-power modes are different. We observed the linear polarization of fields in the cavity at low loss mode while random polarization of the side bands in the high-power mode for which we extracted more gain. We then individually synchronized the sidebands (either signal or idler) from the fed back portion with the pump in the cavity at the low loss condition to observe if any difference occurs in the degree of polarization of the fields with respect to the input power. Figure 5.8 is the plot of the degree of polarization of the fields in the FOPO cavity as a function of the input power when either signal or idler wave in the fed back portion of the light is synchronized with the pump field. We observe that the DOP of the fields are similar in figure 5.8(a) and 5.8(b). The signal and pump are polarized while idler is unpolarized indicating that synchronizing either oscillating idler or signal wave does not produce any changes in the degree of polarization of the fields.

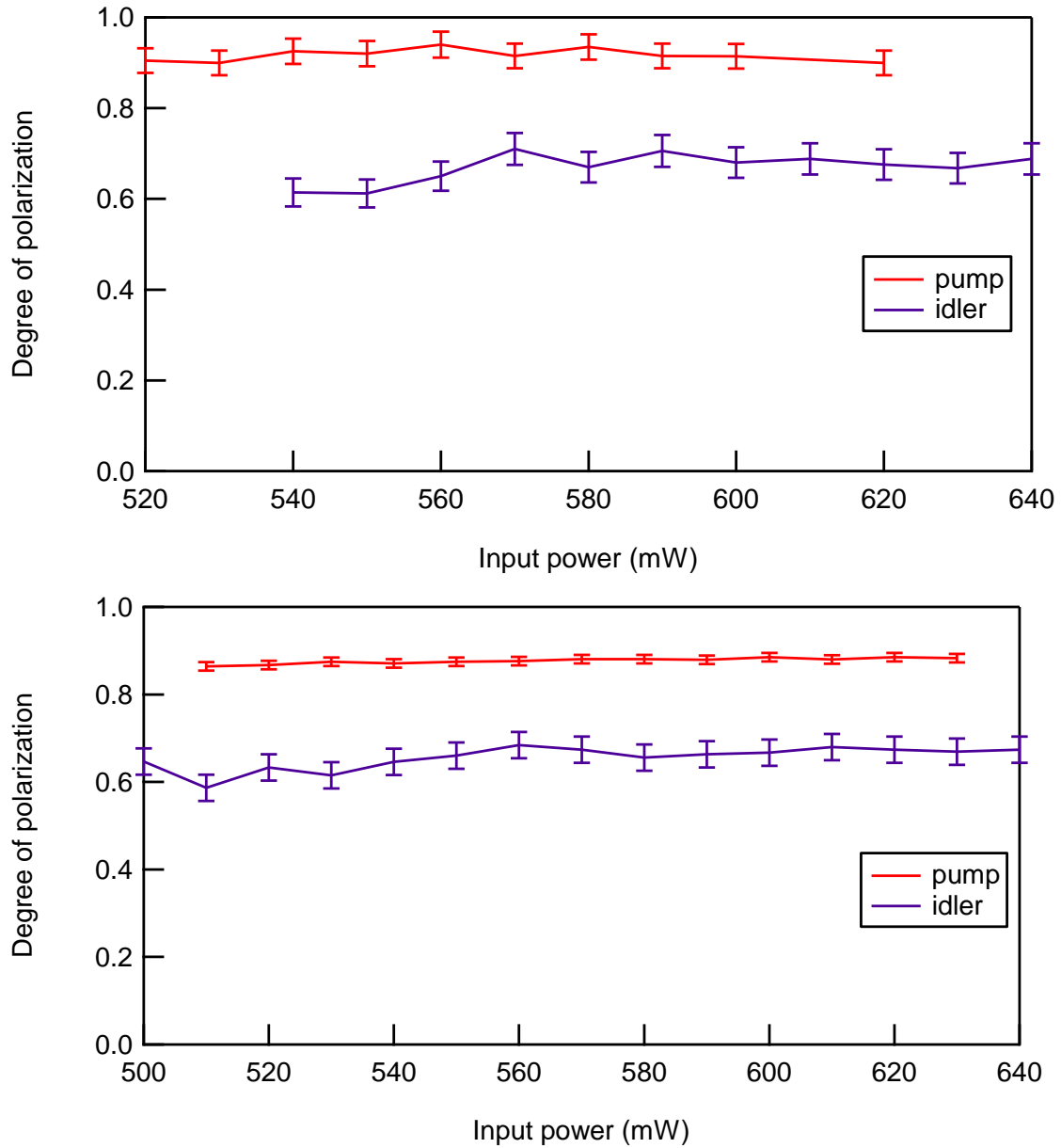


Fig. 5.8. Measurement of the DOP of the fields in the cavity at low loss condition when the feed-back mode is oscillating (a) idler wave and (b) signal wave. Due to limited number of data points, the DOP of signal not plotted however, it was over 0.9 for both.

## 5.7 Summary

We demonstrated the output measurement using a polarization-based output coupling in a FOPO leading to the higher output power. Our reflectivity studies suggest that the polarization state within the FOPO must be considered with the output coupling ratio. This scheme draws attention to the state of polarization of the pump and the feedback. It appears

promising as it allows a flexible control over the output power by controlling the polarization mode overlap with the output coupling ratio and it also allows flexibility in optical alignment. We found that the powers of the output waves of the FOPO depend on the polarization overlaps and we analyzed the polarization sensitivity of the waves using our scheme. Depending on the polarization modes, the FOPO can work at more oscillating conditions yielding lower output power (low-loss condition) and at reduced oscillating conditions yielding higher output power (high-power condition). Different polarization orientations for different fields on Poincare sphere indicate that the gain depends on the polarization state of the fields and adjusting optical components like HWP and FPC help in maximizing the coupled output power. We also observed an increase in coupled output power with the input pump. Finally, we can extract both sidebands which makes this source attractive for use in coherent multi-photon microscopy.



## CHAPTER 6

### OPTICAL PARAMETRIC OSCILLATOR USING A TRIPLE CORE FIBER

A fiber optical parametric oscillator (FOPO) is a coherent source of light based on four-wave mixing in an optical fiber. The four-wave mixing process occurs only when the phase matched conditions are satisfied. It is considered as a promising alternative to the solid-state lasers for its robustness and compactness. FOPOs can offer high gain and low noise figure simultaneously with large bandwidth [69-71]. It was first demonstrated in 1975 by R. H. Stolen in a multimode fiber using a doubled Q-switched Nd: YAG laser of wavelength 532 nm [65]. It has been experimentally realized using both degenerate (single pump FOPO) and non-degenerate (dual pump FOPO) four wave mixing process in a single mode single core fiber [72]. Compared to single pump FOPO, dual pump FOPO provides a high and flat gain over a broad bandwidth [8]. But dual pump FOPO requires two sources which makes it immobile due to complex alignment. To overcome this drawback, recently, fiber optical parametric amplification has been theoretically studied using a dual core fiber showing a flat gain over a large bandwidth similar to that of dual pump FOPA which can potentially be applied to novel applications [73]. In this chapter, we focus on the development of the FOPO using a multicore fiber based on the degenerate-FWM. We develop the modified coupled mode theory for the wave propagating in a triple core fiber and its application in constructing optical parametric oscillator using four photon mixing process. To our knowledge, this is the first demonstration of the fiber optical parametric oscillator using 3-core microstructure fiber.

#### 6.1 Modified coupled mode theory

In a multicore fiber, the neighboring cores are sufficiently close for the overlap of evanescent fields of each core. This leads to the power transfer between the modes of cores and its neighbor periodically. In the triple core PCF of interest, we consider the overlap of the wavefunction between only the nearest neighbor cores. For the linear configuration of cores, we neglect the mode coupling between core 1 and 3 as the wave decays exponentially

in the cladding region. The coupled mode theory is based on the mode of individual cores. The study of mode coupling in an optical fiber is crucial for the control of the power transmission. The wave propagation in a triple core fiber for a high-power beam can be described with coupled nonlinear Schrodinger equations [74] as

$$\begin{aligned}\frac{dA_1}{dz} &= j\kappa_1 A_2 + j\gamma |A_1|^2 A_1 \\ \frac{dA_2}{dz} &= j(A_1 + \kappa_2 A_3) + j\gamma |A_2|^2 A_2 \\ \frac{dA_3}{dz} &= j\kappa_2 A_2 + j\gamma |A_3|^2 A_3\end{aligned}\tag{6.1}$$

where  $A_1$ ,  $A_2$  and  $A_3$  are the amplitudes of the electric fields in core 1, 2 and 3 respectively at position  $z$  along the fiber length;  $\kappa_1$  and  $\kappa_2$  are the coupling coefficient between the cores between modes in core 1-2, and 2-3 respectively; and  $\gamma$  is the nonlinear parameter. The coupling coefficient depends on the area of overlap of the individual core modes. Small mode overlap leads a small  $\kappa$  and vice-versa. It also varies along the length of fiber due to imperfections in the fiber, which we neglect assuming that the degree of imperfection is very low. For the linear characteristics, we assume the propagation in a low intensity field and one may set  $\gamma = 0$  in above coupled mode equations.

There are nine fields propagating along the fiber length at 3 different frequencies, assuming all idlers have frequency  $\omega_i$  and all signals have frequency  $\omega_s$ . The evolutions of the 9 fields propagating inside the 3 cores of a fiber are governed by the following coupled mode equations [8, 73, 75].

$$\begin{aligned}\frac{dA_{p1}}{dz} &= j\beta_{p1} A_{p1} + j\gamma \left\{ |A_{p1}|^2 + 2(|A_{s1}|^2 + |A_{i1}|^2) \right\} A_{p1} \\ &\quad + 2j\gamma A_{p1}^* A_{s1} A_{i1} e^{j\Delta\beta z} + j\kappa_1 A_{p2} \\ \frac{dA_{s1}}{dz} &= j\beta_{s1} A_{s1} + j\gamma \left\{ |A_{s1}|^2 + 2(|A_{p1}|^2 + |A_{i1}|^2) \right\} A_{s1} \\ &\quad + 2j\gamma A_{p1}^2 A_{i1}^* e^{-j\Delta\beta z} + j\kappa_1 A_{s2} \\ \frac{dA_{i1}}{dz} &= j\beta_{i1} A_{i1} + j\gamma \left\{ |A_{i1}|^2 + 2(|A_{p1}|^2 + |A_{s1}|^2) \right\} A_{i1} \\ &\quad + 2j\gamma A_{p1}^2 A_{s1}^* e^{-j\Delta\beta z} + j\kappa_1 A_{i2}\end{aligned}$$

$$\begin{aligned}
\frac{dA_{p2}}{dz} &= j\beta_{p2}A_{p2} + j\gamma \left\{ |A_{p2}|^2 + 2(|A_{s2}|^2 + |A_{i2}|^2) \right\} A_{p2} \\
&\quad + 2j\gamma A_{p2}^* A_{s2} A_{i2} e^{j\Delta\beta z} + j(\kappa_1 A_{p1} + \kappa_2 A_{p3}) \\
\frac{dA_{s2}}{dz} &= j\beta_{s2}A_{s2} + j\gamma \left\{ |A_{s2}|^2 + 2(|A_{p2}|^2 + |A_{i2}|^2) \right\} A_{s2} \\
&\quad + 2j\gamma A_{p2}^2 A_{i2}^* e^{-j\Delta\beta z} + j(\kappa_1 A_{s1} + \kappa_2 A_{s3}) \\
\frac{dA_{i2}}{dz} &= j\beta_{i2}A_{i2} + j\gamma \left\{ |A_{i2}|^2 + 2(|A_{p2}|^2 + |A_{s2}|^2) \right\} A_{i2} \\
&\quad + 2j\gamma A_{p2}^2 A_{s2}^* e^{-j\Delta\beta z} + j(\kappa_1 A_{i1} + \kappa_2 A_{i3}) \\
\frac{dA_{p3}}{dz} &= j\beta_{p3}A_{p3} + j\gamma \left\{ |A_{p3}|^2 + 2(|A_{s3}|^2 + |A_{i3}|^2) \right\} A_{p3} \\
&\quad + 2j\gamma A_{p3}^* A_{s3} A_{i3} e^{j\Delta\beta z} + j\kappa_2 A_{p2} \\
\frac{dA_{s3}}{dz} &= j\beta_{s3}A_{s3} + j\gamma \left\{ |A_{s3}|^2 + 2(|A_{p3}|^2 + |A_{i3}|^2) \right\} A_{s3} \\
&\quad + 2j\gamma A_{p3}^2 A_{i3}^* e^{-j\Delta\beta z} + j\kappa_2 A_{s2} \\
\frac{dA_{i3}}{dz} &= j\beta_{i3}A_{i3} + j\gamma \left\{ |A_{i3}|^2 + 2(|A_{p3}|^2 + |A_{s3}|^2) \right\} A_{i3} \\
&\quad + 2j\gamma A_{p3}^2 A_{s3}^* e^{-j\Delta\beta z} + j\kappa_2 A_{i2}
\end{aligned} \tag{6.2}$$

We assumed that the input fields are parallel polarized. Assuming all pumps have the similar propagation constant,  $\beta_{p1} = \beta_{p2} = \beta_{p3} = \beta_p$ ; all pumps are initially in same phases, the equations representing the evolution of the pump waves along the length of the fiber are,

$$A_{pm} = \sqrt{P_{pm}} e^{j(\gamma P_m + \beta_p + \kappa_1 + \kappa_2)z} \tag{6.3}$$

where  $m = 1, 2, 3$  represents the core.  $\kappa_2 = 0$  for  $m = 1$  and  $\kappa_1 = 0$  for  $m = 3$ .  $P_{pm}$  represents the pump power in  $m^{th}$  core.

Similarly, for the signal and idler waves generated, the propagation along the fiber length is governed by the following equations.

$$A_{s(i)m} = e_{s(i)m} e^{j(2\gamma P_p m - \Delta\beta + \beta_{s(i)} + \kappa_1 + \kappa_2)z} \quad (6.4)$$

where  $e_{s(i)m}$  is the initial signal (idler) amplitude in  $m^{\text{th}}$  core and  $\Delta\beta$  is the linear phase-mismatch. It can also be obtained by expanding  $\beta(\omega)$  in Taylor series at the zero-dispersion frequency  $\omega_0$  given by

$$\Delta\beta = \beta_s + \beta_i - 2\beta_p = \beta_3(\omega_p - \omega_0)(\omega_s - \omega_p)^2 \quad (6.5)$$

Substituting equations (6.3) and (6.4) into equations (6.2) with an assumption of equal power distribution;  $P_{p1} = P_{p2} = P_{p3} = P_{pm}$ , we obtain six equations which are expressed in the matrix form in a system

$$\frac{d\mathbf{E}(z)}{dz} = i\mathbf{M}\mathbf{E}(z) \quad \text{with}$$

$$\mathbf{M} = \begin{pmatrix} -\Delta\beta - \kappa & \gamma P_p & \kappa & 0 & 0 & 0 \\ -\gamma P_p & \Delta\beta + \kappa & 0 & -\kappa & 0 & 0 \\ \kappa & 0 & -\Delta\beta - 2\kappa & \gamma P_p & \kappa & 0 \\ 0 & -\kappa & -\gamma P_p & \Delta\beta + 2\kappa & 0 & -\kappa \\ 0 & 0 & \kappa & 0 & -\Delta\beta - \kappa & \gamma P_p \\ 0 & 0 & 0 & -\kappa & -\gamma P_p & \Delta\beta + \kappa \end{pmatrix} \quad (6.6)$$

Eigenvalues of this 6X6 matrix are

$$g_1 = \sqrt{\gamma^2 P_p^2 - \Delta\beta^2}$$

$$g_2 = \sqrt{\gamma^2 P_p^2 - (\Delta\beta + \kappa)^2}$$

$$g_3 = \sqrt{\gamma^2 P_p^2 - (\Delta\beta + 3\kappa)^2} \quad (6.7)$$

These eigenvalues give the gain coefficients for the FOPO. Figure 6.1(a) is the plot of these gain coefficients as a function of linear phase mismatch ( $\Delta\beta$ ) as nonlinear phase mismatch remains fixed for a certain input power.  $g_1$ ,  $g_2$  and  $g_3$  represent the gain coefficient for optic fiber with single core, dual core and triple core respectively. From figure 6.1(a), we see that maximum gain can be obtained from a fiber at a larger phase mismatch if the fiber has more cores.

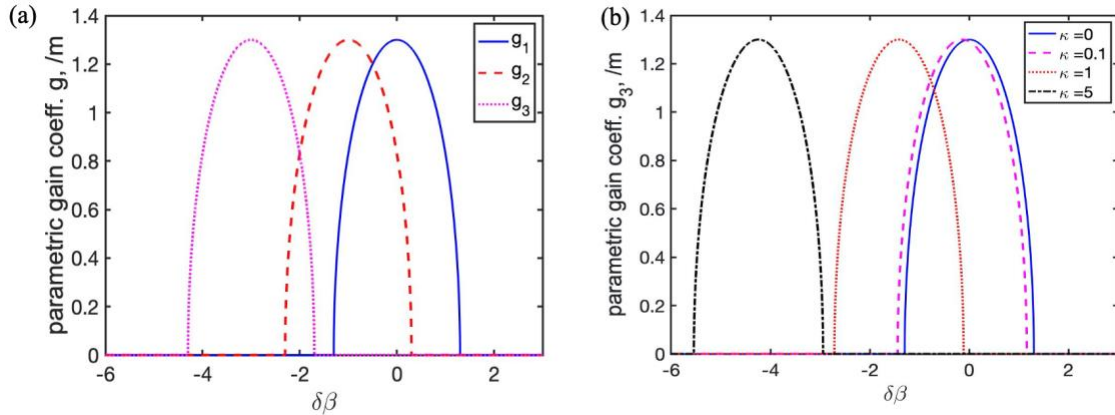


Fig. 6.1. Parametric gain curves as a function of linear phase mismatch ( $\Delta\beta$ ) at  $\gamma = 14 W^{-1}km^{-1}$  and  $P_p = 100W$  (a) For gain coefficient  $g_1$ ,  $g_2$  and  $g_3$  at coupling coefficient  $\kappa = 1$ , (b) For gain coefficient  $g_3$  at different value of coupling coefficient  $\kappa$  ( $1/m$ ).

Figure 6.1(b) is the plot of the gain coefficient for a triple core fiber as a function of linear phase mismatch for different values of coupling coefficient. It shows that the gain peak shifts away from  $\Delta\beta = 0$  with the increase in  $\kappa$  suggesting that the maximum gain can be achieved even if there is the presence of some phase mismatch by raising the value of coupling coefficient which is an advantage for a long fiber as it is difficult to maintain phase matching over a long fiber length.

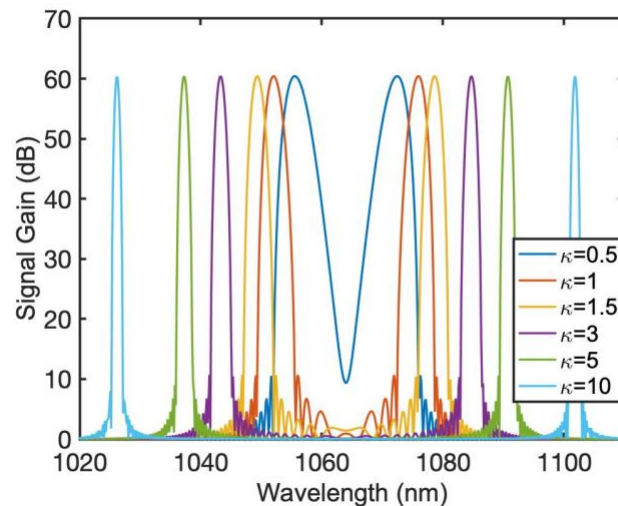


Fig. 6.2. Parametric signal gain at various values of linear coupling coefficient at  $\gamma = 14 W^{-1}km^{-1}$  and  $P_p = 220 W$ .

The signal gain obtained at the fiber output end is given by [76]

$$G = 1 + \left\{ \frac{\gamma P_p}{g} \sinh(gL) \right\}^2. \quad (6.8)$$

where, symbols have their usual meanings. The numerical plot of Eq. 6.8 for different values of coupling coefficient is in fig. 6.2. In Fig. 6.2, we see that the detuning between the signal/idler and the pump becomes larger with increase in the coupling coefficient value. Therefore, we can utilize mode coupling in a multicore fiber to generate tunable parametric gain bands. Mode-coupling can be controlled with the input pump power and the wavelength.

## 6.2 Degenerate four wave mixing in 3-core fiber

Four wave mixing (FWM) is an important nonlinear process for the parametric amplification in an optical fiber. For a strong pump field launched into the fiber, signal and idler waves are generated by FWM process as shown in Fig. 6.3 and obey the coupled mode equations given by Eq. 6.2. A general description of FWM process is presented in chapter 5. To generate an efficient FWM, the pump wavelength should lie at or close to the zero-dispersion wavelength of the fiber. The frequency and phase matching conditions are

$$\begin{aligned} 2\omega_p &= \omega_i + \omega_s \\ \beta_p &= \beta_i + \beta_s \end{aligned} \quad (6.9)$$

For the FWM process to occur, the effective phase mismatch factor must be reduced. Both linear and nonlinear properties contribute to the effective phase mismatch factor as given by

$$K = \Delta\beta + 2\gamma P_0 \quad (6.10)$$

where, the linear phase mismatch factor  $\Delta\beta$  is contributed by both material and waveguide dispersions and is given by eq. 5.1. For an efficient FWM, we choose a pump wavelength that coincides or lies very close to the zero dispersion of the fiber.

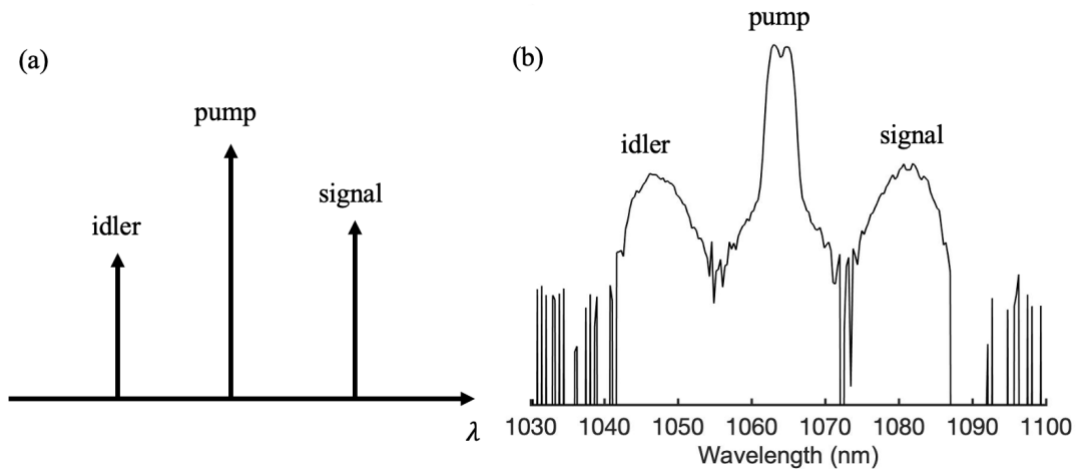
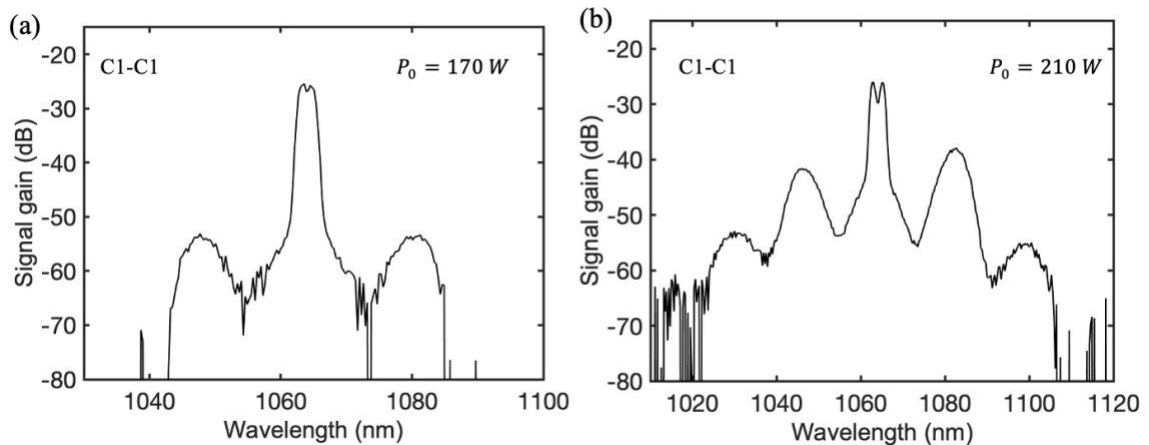


Fig. 6.3. (a) Schematic of degenerate four wave mixing process. (b) Experimentally observed degenerate FWM in a 3-core fiber when central core is excited.

We demonstrate a clear evidence of FWM at 1064 nm in the anomalous dispersion regime in a 3-core PCF as shown in Fig. 6.4. Figure 6.4 (a,c,e) are the FWM happening in the launched core at a relatively low input power while figure 6.4 (b,d,f) are the cascaded FWM observed at launched cores for relatively high input powers. The characteristics of FWM spectrum strongly depends on the pump wavelength. Observance of FWM offered a great opportunity to configure a parametric oscillator using this multicore fiber.



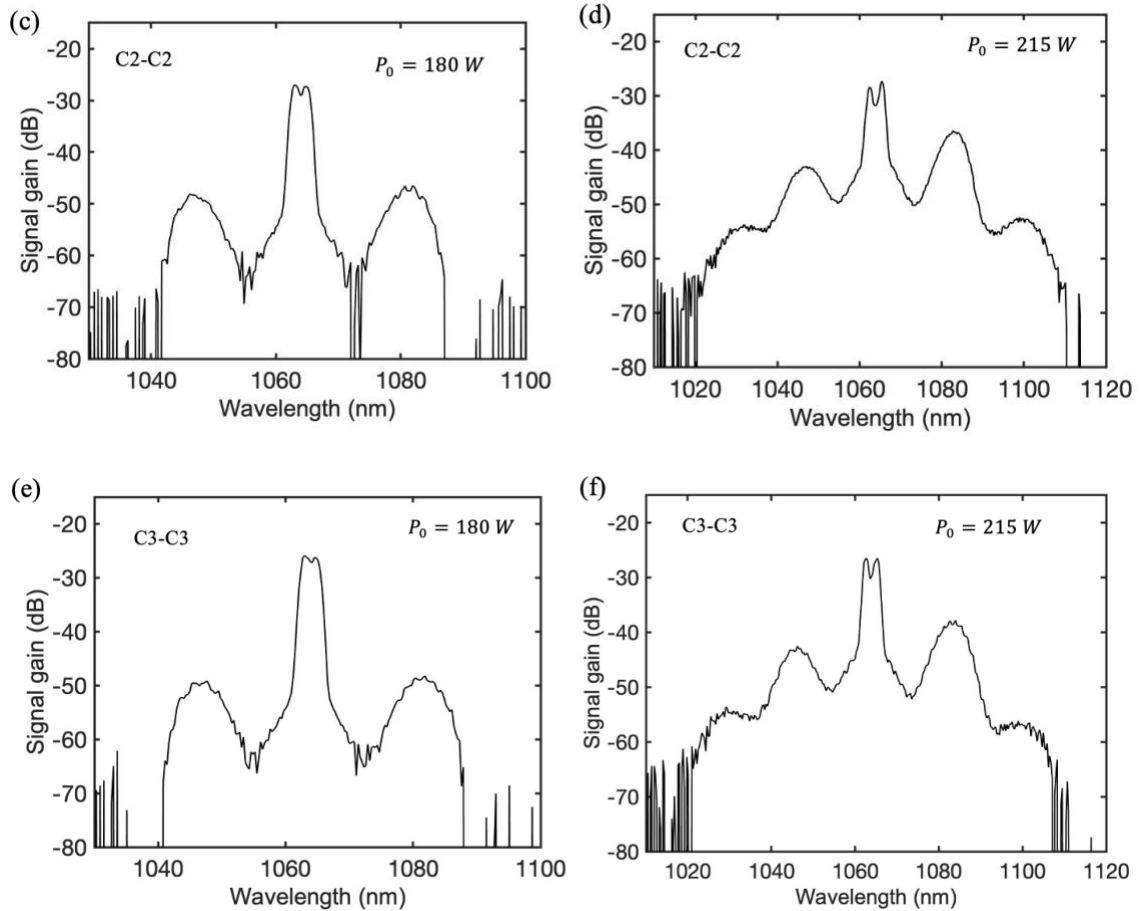


Fig. 6.4. Four wave mixing happening in all cores when they are individually excited almost at the same power. Figures on the right side show the cascaded FWM.

### 6.3 Polarization dependence of FWM gain

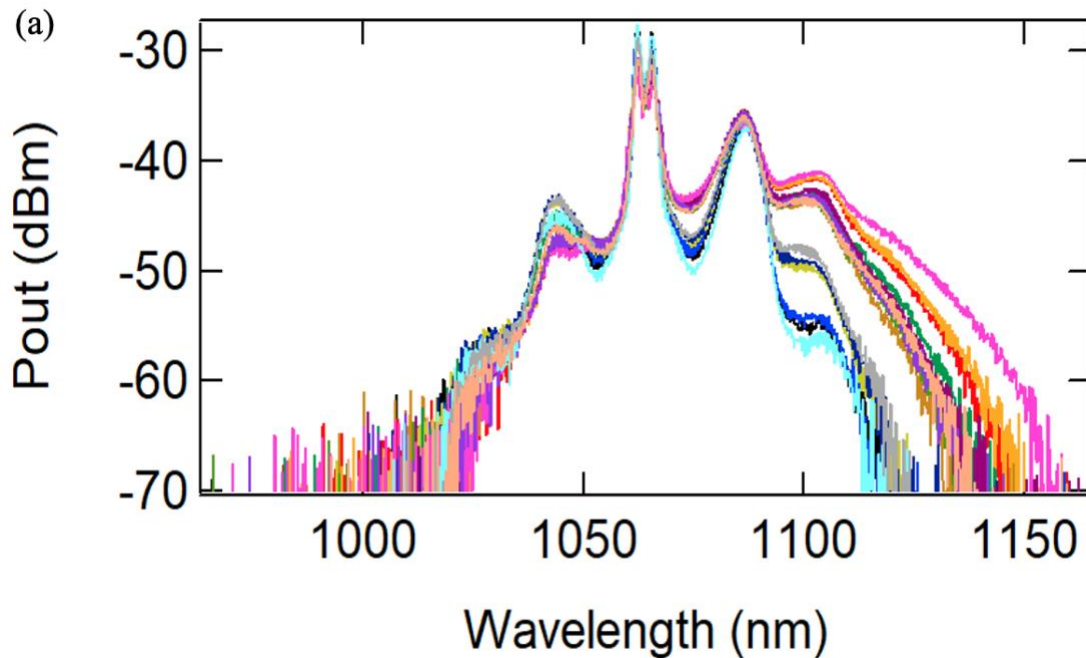
The efficiency of the FWM process depends on the polarization state of the input pump [68]. If the input state of polarization (SOP) of pump is kept fixed, the signal and idler, generated in the fiber due to FWM, may have different polarization states due to the presence of random birefringence in the fiber. So, it is crucial to understand the polarization state of the interacting fields to optimize the gain.

The fiber birefringence can be neglected for a short fiber and therefore, we may assume all fields to be co-polarized with the input pump. However, one may need to consider the nonlinear polarization rotation of the pump SOP due to the fiber nonlinearity [76]. In general, the FWM efficiency is maximized when all fields are parallel regardless of their



individual SOP for a linearly polarized input pump. In case of long fiber, one cannot ignore the effect of randomly varying residual birefringence.

To observe the effect of the polarization on the FWM gain, we rotated the wave plate and recorded the FWM gain. The plot in Fig. 6.5 (a) is measuring the output from the same core as the one into which the light was launched. With the change in the polarizing angle, we observe significant amount of spectral broadening. The plot in Fig. 6.5 (b) is measuring the output from the adjacent core when low-powered light is launched in central core. This also shows that the measurement also depends on the polarization. We observed that both output pump and sidebands spectra change with the polarization. However, we do not study polarization effects in details. The variation observed in the output power with the polarization may be because the mode coupling is polarization dependent. Moreover, we know that the FWM is the polarization dependent. It is therefore, important to consider the effect of the input polarization on the output power measurement.



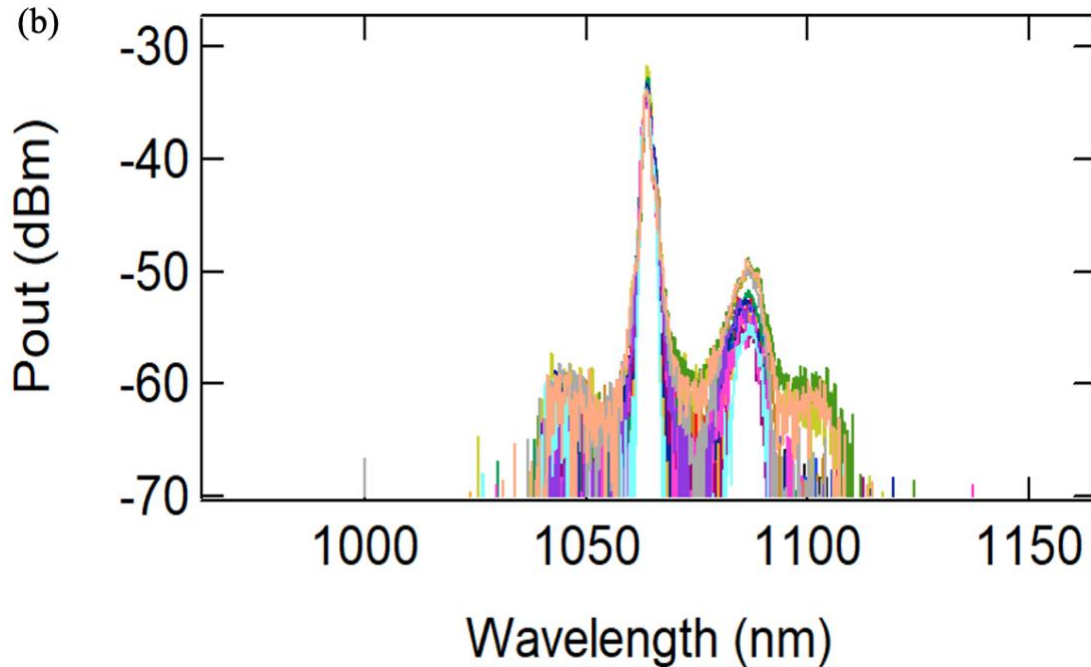


Fig. 6.5. FWM gain spectra including pump when polarizing angle is changed at the fiber input. Light is launched in 2<sup>nd</sup> core and output are measured at (a) 2<sup>nd</sup> core (b) an adjacent core.

#### 6.4 Three-core fiber optical parametric oscillator

The experimental setup is schematically shown in Fig. 6.6, similar to that described in chapter 5. The pump source is a mode locked Nd:Vanadate laser operating at a wavelength of 1064 nm with 8 ps pulses at a repetition rate of 80 MHz. A 5-m long 3-core microstructure fiber is placed in the cavity formed by the high reflector M3 and the front end of the fiber. Mirrors M1 and M2 are placed before the input end of the fiber and a combination of half wave plate and polarizing beam splitting cube works as an attenuator controlling the input light. An iris can be placed in the cavity after the lens to block to block some of light modes allowing the desired modes to feedback into the cavity from the end mirror. Light launched into one of the cores of a coupled-multicore fiber emerges out of all cores due to the sharing of energy between the adjacent cores.

A dichroic mirror (short-wave pass (SWP) or long-wave pass (LWP)) can also be placed in the cavity after the lens at an angular position of  $45^{\circ}$  so that the longer wavelength or shorter wavelength is reflected while other is oscillating in the cavity and can be recorded at the output port. The signal or idler average power can be measured by stopping pump using a notch filter at 1064 nm. The fields are oscillating in the cavity with adjusted cavity length.

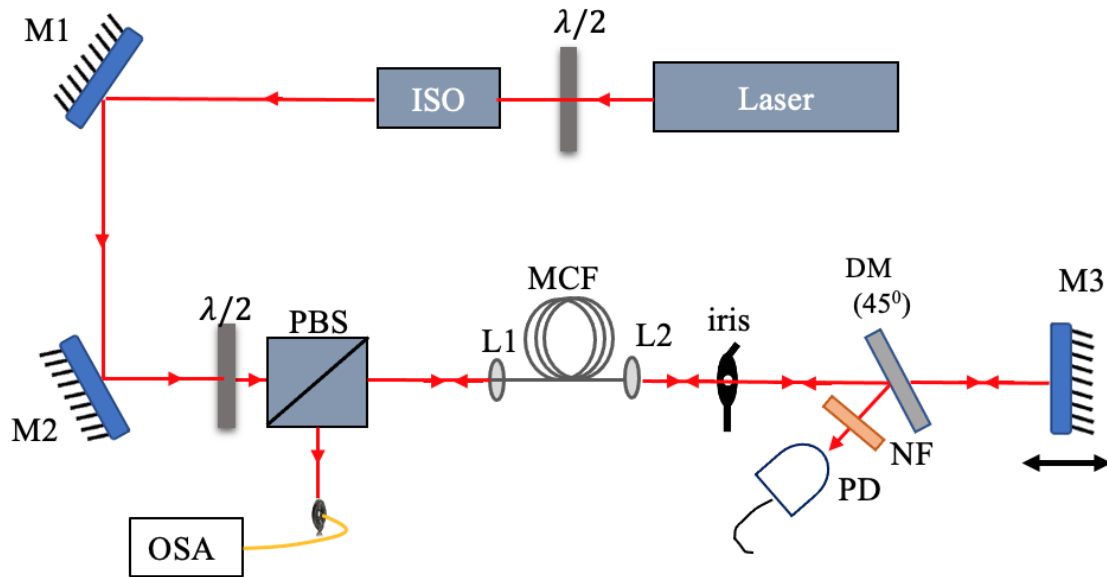


Fig. 6.6: Schematic of experimental setup for the triple core fiber optical parametric oscillator

For the measurement in Fig. 6.7, light is launched into the central core. Fig. 6.7 (a) are the plots when all light from all cores is present in the cavity and only light from C3, C2 and C1 are individually feedback into core 2 at the fiber output end. It is observed that the feedback of the light from C3 into C2 gives the highest power. This may arise due to the different coupling coefficient values. Fig. 6.7 (b) is the similar power measurement for the case when the lights from C1 and C3 are blocked in the cavity using an iris and the light is fed back to C2. It seems that the presence of light from all cores gives more output compared to the blocking of two of the core's modes.

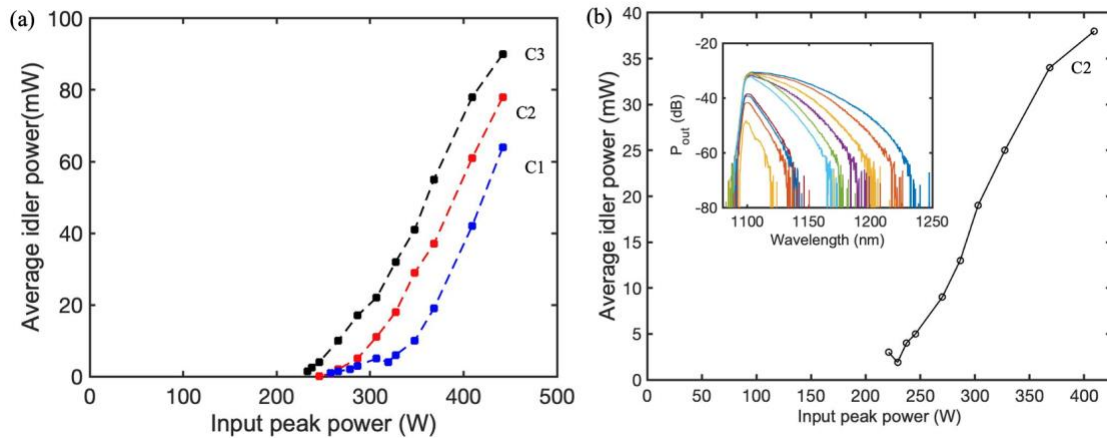


Fig. 6.7: Longer sideband power measurement when the input is at C2. (a) Removing iris in Fig. 6.6 and feeding light from C2 back to C1, C2 and C3 individually. (b) Using iris in Fig. 6.6 to block modes from C1 and C2 so that modes from C2 is feedback to C2.

FWM is power dependent. For an input peak power between 170-300 W, FWM happens in our fiber. But when the power exceeds 300 W, there occur other nonlinear processes in the fiber including the continuum. We observe the rise in measured output power in the oscillating mode with increase in the input power as shown in Fig. 6.8 (red curve). We measured the power in the cavity when the field is not oscillatory (represented by the blue curve in Fig. 6.8) which is due to other non-linear effects in the fiber at high power causing broadening of the pulse. Fig. 6.9 are the output power measurement as a function of the input peak power when different modes are coupled back to the fiber at output end in the cavity. At a certain fiber length, different cores have different amount of nonlinearity depending on the pump power and the fiber's nonlinear length which is shown by black curves in figure 6.9.

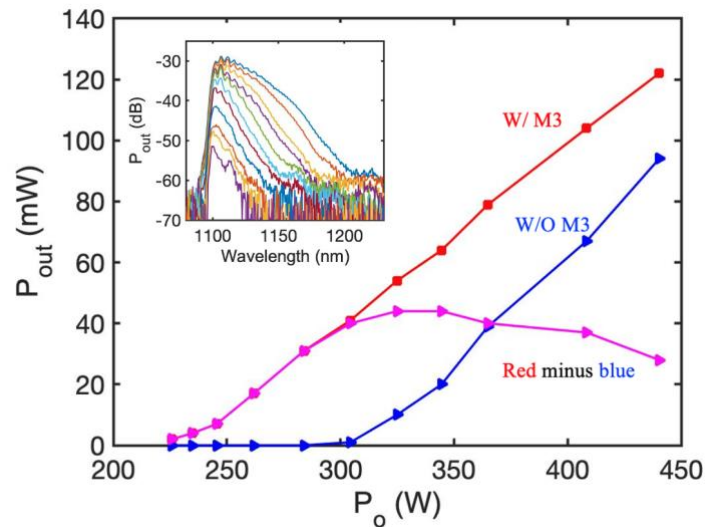


Fig.6.8: Longer sideband power measurement when the light is launched at core C3 and the light is fed back into the same core. Red curve represents the output power when field is oscillatory in the cavity. Blue curve represents the power measurement when mirror M3 is blocked. Magenta curve the actual power extracted from the FOPO cavity. Inset is the output spectra corresponding to power measurement for the red curve.

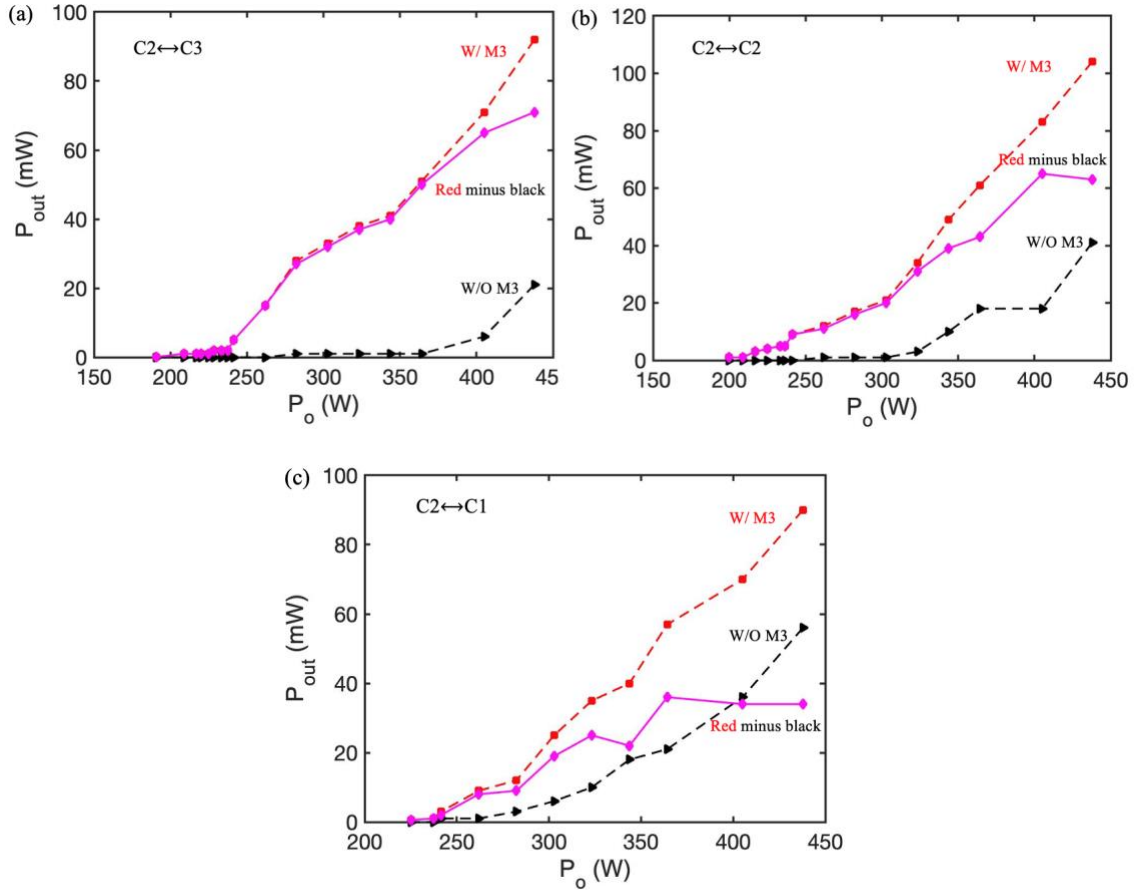


Fig. 6.9: Longer wavelength sideband power measurement when the light is launched in core C2 and light is fed back in the cavity in (a) core C3 (b) core C2 and (c) core C1.

## 6.5 Summary

Producing FWM in a 3-core fiber near 1064 nm offered an opportunity to configure a parametric oscillator using this fiber. Distributed FWM happens in a 3-core fiber due to interplay between coupling length and the fiber's nonlinear length as explained in chapter 4. We demonstrated a fiber optical parametric oscillator using a triple core microstructure fiber for the first time to our knowledge. We studied the effect of mode coupling in the output power obtained from the FOPO. We measured the signal power for different mode coupling cases in the cavity and found that the presence of more modes allows more power extraction from the system. Using multicore fiber is advantageous not only because of the mode-coupling between modes from different cores but it is important as the fields in the cavity can be controlled by controlling the light from different cores. We modified the couple mode theory governing the pulse propagation in an optical fiber of our type and established a gain relationship with the coupling coefficient. We also observed that the

FWM is polarization dependent and therefore, it is crucial to consider the input polarization for a maximum output power.

## CHAPTER 7

### FUTURE DIRECTIONS

While optical fiber has been a research subject of experimental investigation for more than 3 decades, it still shows promise for its future applications in telecommunication and other fields. In recent days, the research in optical fiber is more focused onto multimode and multicore fibers for their potential applications in ultrahigh-speed transmission and ultrahigh system capacity. In the thesis, we studied some of linear and nonlinear properties of a triple core microstructure fiber and its use in parametric devices. Mode coupling in multicore fiber can be disadvantageous as it may degrade the signal transmission. At the same time, mode coupling can be utilized to reduce the GVD spread and transfer of energy to the adjacent cores. Its application in parametric oscillator has been investigated experimentally however, we have not yet fully understood the complex nature of mode coupling which is elaborated in Fig. 7.1. Further works like understanding the effects of mode coupling on the signal transmission, and gains from each core can be explored further. MCF has several applications in building sensors, nonlinear imaging, squeezed light generation, entangled photon pairs generation etc. We may require a special fiber tailored to a particular application. But we can use the fiber we have to study how the gain can be optimized with wavelength, power, polarization and cavity design. Below are some of the examples of the future works that can be done using this fiber to understand the working mechanism and tailorable parameters for gain optimization and efficient performance.

#### 7.1 Power measurement with different alignments

The experimental setup for the power measurement is similar to that described in chapter 6. Figure 7.1 is a schematic of a section of the experimental setup for the output power measurement of the FOPO. The pump source is a mode locked Nd:Vanadate laser operating at a wavelength of 1064 nm with 8 ps pulses at a repetition rate of 80 MHz. A 5-m long 3-core microstructure fiber is placed in the cavity formed by the high reflector M3 and the front end of the fiber. Mirrors M1 and M2 are placed before the input end of the

fiber to increase the light coupling into the fiber and a combination of half wave plate and polarizing beam splitting cube works as an attenuator controlling the input light. Light launched into one of the cores of a coupled-multicore fiber emerges out of all cores due to the sharing of energy between the adjacent cores. At the fiber output end, the position of the lens can be adjusted in such a way that the end mirror M3 will lie inside or outside of the focal length of the lens as shown in diagram 7.1 (a) and (b). An iris can be placed in the cavity after the lens to block two of the modes so that only one of the light modes will be feedback in the cavity with the end mirror M3 as in figure 7.1 (c). A short-wave pass (SWP) or long-wave pass (LWP) for the wavelength of 1064 nm can also be placed in the cavity after the lens at an angular position of  $45^\circ$  so that the longer wavelength or shorter wavelength is reflected and can be recorded at the output port. The signal or idler average power can be measured by stopping pump using a notch filter at 1064 nm. The fields are oscillating in the cavity with adjusted cavity length.

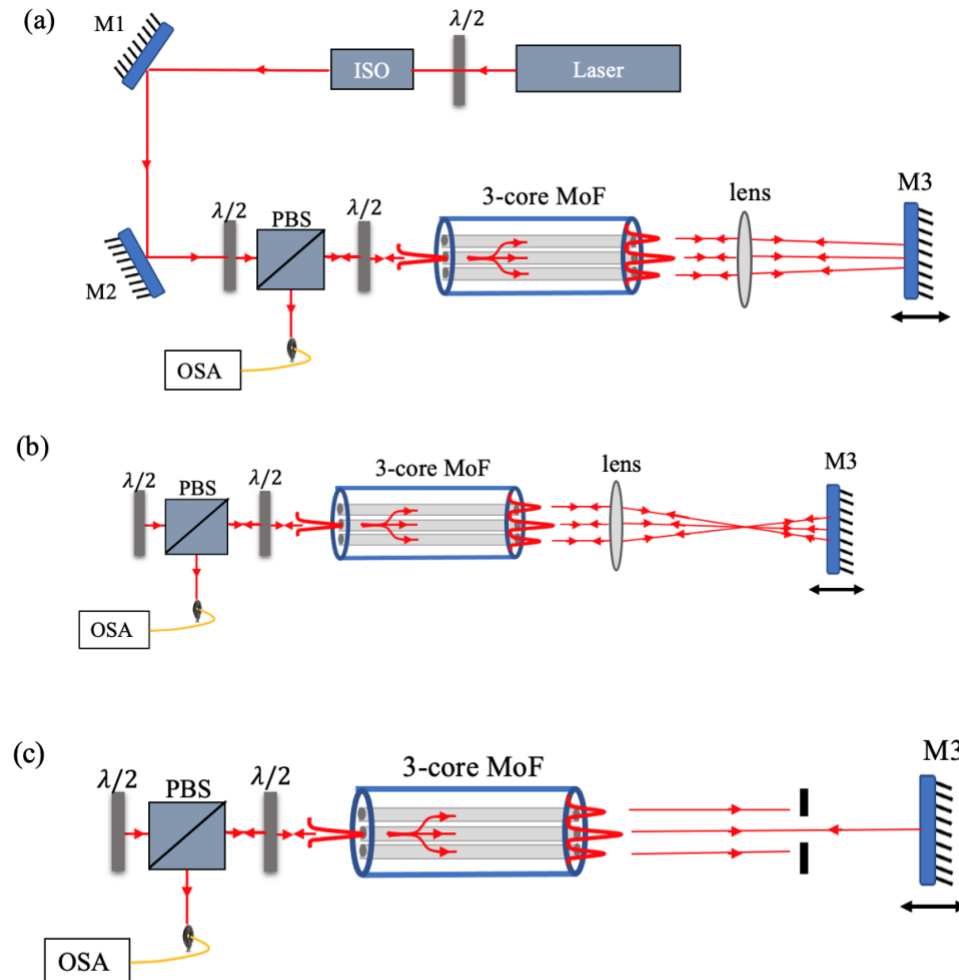


Fig. 7.1: Schematic of experimental setup of 3-core FOPO with different arrangements for inter-mode coupling in the optical cavity. (a) mirror M3 placed



within the focal length of the lens (b) mirror M3 placed outside of the focal length of the lens (c) two of the modes blocked in the cavity.

## 7.2 Entangled photon pair generation for quantum optics applications

The standard method to generate entangled photons pairs is a parametric down conversion in a nonlinear crystal in which a pump light is converted into two new photons. In recent years, spontaneous four wave mixing in an optical fiber has gained much attention for the entangled photon pair generation [77]. This is because of easier integration and networking with the quantum networks using optic fiber. Moreover, manipulation of fiber parameters and shifting of fiber dispersion can be done to generate photon pairs in desired spectral region. Mode coupling in multicore fiber, which is a beam splitter operation when considered quantum-optically, may provide interesting photon pair generation compared with single-core systems. There are now three cores in which the entangled photons may be born and three cores from which they might emerge. Diagram 7.2 is the schematic of detection of photons generated by the spontaneous FWM in an optical fiber. The signal or idler generated can be connected in a homodyne method in which signal interferes with a coherent beam from external local oscillator (strong) at 50:50 beam splitter and generates photo current at photodetector. These photo currents can be analyzed for the squeezed state generation.

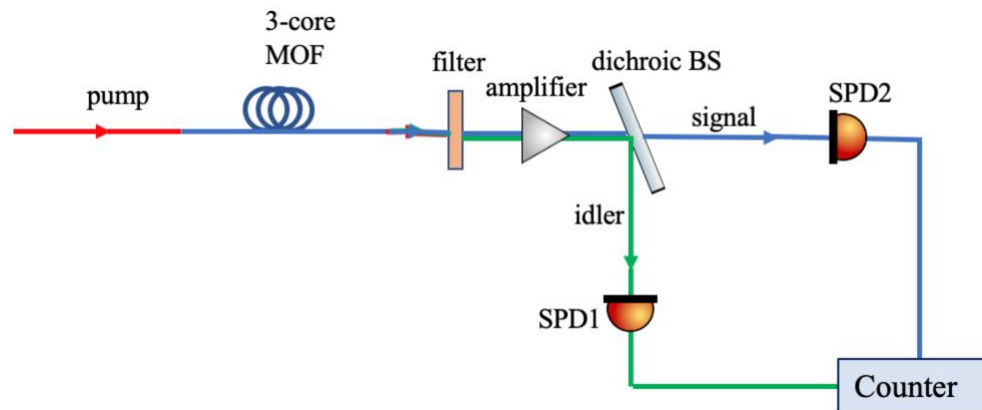


Fig. 7.2. Schematic of the counting of photons generated by the SFWM in an optical fiber. Dichroic beam splitter (dichroic BS) transmits signal and reflects idler. SPD: single photon detector.

### 7.3 Triple core fiber sensors

Because of the unique features like small cross section, tailorable dispersion, high sensitivity, and adjustable physical parameters, a multicore photonic crystal fiber is widely used in sensors that monitor temperature [78], pressure, curvature [79, 80], bends, liquid flow, vibration and strain. The working of fiber sensors is based on principles such as fiber Bragg grating (FBG), Brillouin scattering and interferometers (like Mach-Zehnder, Fabry-Perot etc.). Multicore fiber *shape sensors* have also become an interesting research area for shape sensing for medical applications due to its flexibility, and lightweight and MCF offers more safety [81]. Use of spun multicore fiber in shape sensors helps in maintaining an elastic behavior even at high twisting deformation resulting in efficient performance with more accurate response [81]. The mode coupling in multicore fiber has been utilized to realize fiber sensors with improved performance. Fengze Tan *et al.* demonstrated a robust and stable torsion sensor based on the mode coupling among cores in a tapered seven-core fiber with larger measurement range ( $160^{\circ} - 940^{\circ}$ ) than other devices [82]. There is much opportunity to use MCF in sensors and to understand the role of mode coupling on their performance.

## Bibliography

- [1] T. Hayashi, Y. Tamura, T. Hasegawa, and T. Taru, "Record-Low Spatial Mode Dispersion and Ultra-Low Loss Coupled Multi-Core Fiber for Ultra-Long-Haul Transmission," *Journal of Lightwave Technology*, **35**(3), 450-457 (2017)
- [2] D. Sapkota and J. E. Sharping, "Four-wave mixing in a triple-core microstructure fiber," *Optics Express*, **29**(9) 13715-13721 (2021)
- [3] G. P. Agrawal, "Nonlinear fiber optics: its history and recent progress [Invited]," *Journal of the Optical Society of America B*, **28**(12), p. A1-A10 (2011)
- [4] W. Contributors. "List of laser applications." *Wikipedia, The Free Encyclopedia*.
- [5] T. Miya, Y. Terunuma, T. Hosaka, and T. Miyashita, "Ultimate low-loss single-mode fibre at 1.55  $\mu$ m," *Electronics Letters*, **15**, 106-108 (1979).
- [6] J. H. a. P. A. A. a. M. W. a. J. L. a. P. O. Hedekvist, "Fiber-based optical parametric amplifiers and their applications," *IEEE Journal of Selected Topics in Quantum Electronics*, **8**(3), 506-520 (2002)
- [7] G. P. Agrawal, *Fiber-Optic Communication Systems* (Third ed., John Wiley and Sons, Inc., 2002).
- [8] G. P. Agrawal, *Nonlinear quantum optics* (4th ed., Academic press, 2007).
- [9] I. Fang, *A History of Mass Communication*, Newton, MA 255-267 (Focal Press, 1997).
- [10] J. Hecht, *City of light: The Story of Fiber Optics* (New York: Oxford University Press Inc., 1999).
- [11] M. Bellis. "How Fiber Optics Was Invented." ThoughtCo. ([thoughtco.com/birth-of-fiber-optics-4091837](https://www.thoughtco.com/birth-of-fiber-optics-4091837)) (accessed Feb. 18, 2021).
- [12] T. H. Maiman, *The Laser Odyssey* (Laser Press, 2000).
- [13] A. Javan, W. R. Bennett, and D. R. Herriott, "Population Inversion and Continuous Optical Maser Oscillation in a Gas Discharge Containing a He-Ne Mixture," *Physical Review Letters*, **6**(3), 106-110 (1961)
- [14] K. C. Kao and G. A. Hockham, "Dielectric-fibre surface waveguides for optical frequencies," *Proceedings of the Institution of Electrical Engineers*, **113**(7), 1151-1158 (1966).

- [15] F. P. Kapron, D. B. Keck, and R. D. Maurer, "RADIATION LOSSES IN GLASS OPTICAL WAVEGUIDES," *Applied Physics Letters*, **17**(10), 423-425 (1970).
- [16] B. L. Kasper *et al.*, "130 KM TRANSMISSION EXPERIMENT AT 2 GB/S USING SILICA-CORE FIBER AND A VAPOR PHASE TRANSPORTED DFB LASER," 342-343 (1984).
- [17] R. J. Mears, L. Reekie, I. M. Jauncey, and D. N. Payne, "Low-noise erbium-doped fibre amplifier operating at 1.54 $\mu$ m," *Electronics Letters*, **23**(19), 1026-1028 (1987).
- [18] P. Russell, "Photonic Crystal Fibers," *Science*, **299**(5605), 358, (2003).
- [19] E. S. a. J. W. Hicks, "Optical Wave-Guide Modes in Small Glass Fibers, I Theoretical," in "Program of the 1959 Annual Meeting of the Optical Society of America," Optical Society of America, **49**, 1128 (1959).
- [20] E. S. H. Osterberg, M. Polanyi, R. Hilberg, "Optical Wave-Guide Modes in Small Glass Fibers,II Experimental," in "Program of the 1959 Annual Meeting of the Optical Society of America," Optical Society of America, **49**, 1128 (1959).
- [21] E. Snitzer, "Optical Maser Action of Nd<sup>3+</sup> in a Barium Crown Glass," *Physical Review Letters*, **7**(12), 444-446 (1961).
- [22] C. J. Koester and E. Snitzer, "Amplification in a Fiber Laser," *Applied Optics*, **3** (10), 1182-1186, (1964).
- [23] S. Inao, T. Sato, S. Sentsui, T. Kuroha, and Y. Nishimura, "Multicore optical fiber," in *Optical Fiber Communication*, Washington, D.C., Optical Society of America, p.WB1 (1979).
- [24] T. Miya, Y. Terunuma, T. Hosaka, and T. Miyashita, "Ultimate low-loss single-mode fibre at 1.55  $\mu$ m," *Electronics Letters*, **15**(4), 106-108 (1979).
- [25] S. B. Poole, D. N. Payne, and M. E. Fermann, "Fabrication of low-loss optical fibres containing rare-earth ions," *Electronics Letters*, **21**(17), 737-738 (1985).
- [26] E. M. Dianov, A. I. Karasik, P. V. Mamyshev, A. M. Prokhorov, and V. N. Serkin, "Stimulated-Raman conversion of multisoliton pulses in quartz optical fibers," *JETP Letters*, **41**(6), 294-297 (1985).
- [27] D. Pysz *et al.*, "Stack and draw fabrication of soft glass microstructured fiber optics," *Bulletin of The Polish Academy of Sciences-technical Sciences*, **62**, 667-682 (2014).

- [28] J.-C. Kim, H.-K. Kim, U.-C. Paek, B.-H. Lee, and J.-B. Eom, "The Fabrication of a Photonic Crystal Fiber and Measurement of its Properties," *Journal of the Optical Society of Korea*, **7**(2), 79-83 (2003).
- [29] "Fundamentals of Optical Fibers," *Fundamentals of Optical Fiber Sensors*, Ch2, 10-75 (2012).
- [30] A. Al-Azzawi, *Advanced Manufacturing for Optical Fibers and Integrated Photonics Devices*, 220 (First ed. CRC Press, 2016).
- [31] P. A. Franken, A. E. Hill, C. W. Peters, and G. Weinreich, "Generation of Optical Harmonics," *Physical Review Letters*, **7**(4), 118-119 (1961).
- [32] W. R. Bosenberg and R. C. Eckardt, "Introduction," *Journal of the Optical Society of America B*, **12**(11), 2084-2084 (1995).
- [33] R. Ryf *et al.*, "Long-Distance Transmission over Coupled-Core Multicore Fiber," in *ECOC 2016 - Post Deadline Paper; 42nd European Conference on Optical Communication*, 1-3 (2016).
- [34] B. J. Puttnam *et al.*, "0.715 Pb/s Transmission over 2,009.6 km in 19-core cladding pumped EDFA amplified MCF link," in *Optical Fiber Communication Conference Postdeadline Papers 2019*, San Diego, California, Optical Society of America, p. Th4B.1 (2019).
- [35] G. Rademacher *et al.*, "172 Tb/s C+L Band Transmission over 2040 km Strongly Coupled 3-Core Fiber," in *Optical Fiber Communication Conference Postdeadline Papers 2020*, San Diego, California, Optical Society of America, p. Th4C.5 (2020)
- [36] K. Saitoh and S. Matsuo, "Multicore fibers for large capacity transmission," *Nanophotonics*, **2**(5-6), 441-454 (2013).
- [37] S. K. S. a. P. Sethi, "Review on Optical Waveguides," in *Emerging Waveguide Technology*, K. Y. You Ed.: IntechOpen, ch. 6 (2018).
- [38] P. S. J. Russell, "Photonic-Crystal Fibers," *Journal of Lightwave Technology*, **24**(12), 4729-4749 (2006).
- [39] R. Lorenzo, M. Seyyedhossein, V. Luca, P. Federica, S. Stefano, and C. Annamaria, "Thermo-optic effects in multicore fibers for high-power lasers," in *Proc.SPIE*, **11357** (2020).

- [40] J. Ji *et al.*, "115 W Large-mode-area Multi-core Fiber Laser with All Solid Structure," in *Conference on Lasers and Electro-Optics*, San Jose, California, Optical Society of America, Technical Digest (2018).
- [41] J. E. Antonio-Lopez, Z. S. Eznavesh, P. LiKamWa, A. Schülzgen, and R. Amezcua-Correa, *Optics Letters*, **39**(15), 4309-4312 (2014).
- [42] C. Xia, N. Bai, I. Ozdur, X. Zhou, and G. Li, "Supermodes for optical transmission," *Optics Express*, **19**(17), 16653-16664 (2011).
- [43] C. Xia *et al.*, "Supermodes in Coupled Multi-Core Waveguide Structures," *IEEE Journal of Selected Topics in Quantum Electronics*, **22**(2), 196-207 (2016).
- [44] M. Marazuela and M. Moreno-Bondi, "Fiber-optic biosensors – an overview," *Analytical and Bioanalytical Chemistry*, **372**(5), 664-682 (2002).
- [45] A. Méndez, "Optics in Medicine," in *Optics in Our Time*, M. D. Al-Amri, M. El-Gomati, and M. S. Zubairy Eds. Cham: Springer International Publishing, 299-333 (2016).
- [46] L. N. Binh, *Optical Fiber Communication Systems with MATLAB<sup>R</sup> and Simulink<sup>R</sup> Models* (Second ed. (Optics and Photonics). CRC Press, Taylor and Francis Group LLC, 2015).
- [47] S. Jensen, "The nonlinear coherent coupler," *IEEE Journal of Quantum Electronics*, **18**(10), 1580-1583 (1982).
- [48] N. Finlayson and G. I. Stegeman, "Spatial switching, instabilities, and chaos in a three-waveguide nonlinear directional coupler," *Applied Physics Letters*, **56**(23), 2276-2278 (1990).
- [49] D. J. Richardson, J. M. Fini, and L. E. Nelson, "Space-division multiplexing in optical fibres," *Nature Photonics*, Review Article **7**, p. 354 (2013).
- [50] M. K. a. N. A. M. K. Saitoh, "Nonlinear photonic crystal fibre: pushing the zero-dispersion towards the visible," *New Journal of Physics*, **8** (2006).
- [51] R. Gumenyuk and O. G. Okhotnikov, "Multiple solitons grouping in fiber lasers by dispersion management and nonlinearity control," *Journal of the Optical Society of America B*, **30**(4), 776-781 (2013).
- [52] S. Mumtaz, R. Essiambre, and G. P. Agrawal, "Reduction of Nonlinear Penalties Due to Linear Coupling in Multicore Optical Fibers," *IEEE Photonics Technology Letters*, **24**(18), 1574-1576 (2012).

- [53] Y. Yan, J. Toulouse, I. Velchev, and S. V. Rotkin, "Decoupling and asymmetric coupling in triple-core photonic crystal fibers," *Journal of the Optical Society of America B*, **25**(9), 1488-1495 (2008).
- [54] R. T. a. K. Thyagarajan, "Analysis of Tunable Single-Mode Fiber Directional Couplers Using Simple and Accurate Relations," *Journal of Lightwave Technology*, **LT-4**(4), 386-390 (1986).
- [55] I. A. Sukhoivanov, O. V. Shulika, S. O. Iakushev, J. A. Andrade Lucio, G. R. Ortiz, and I. V. Guryev, "Nonlinear Pulse Reshaping in Optical Fibers," in *Latin America Optics and Photonics Conference*, Cancun, Optical Society of America, OSA Technical Digest, p. LM3C.4 (2014).
- [56] S. Boscolo and C. Finot, "Nonlinear Pulse Shaping in Fibres for Pulse Generation and Optical Processing," *International Journal of Optics*, **2012**, 159057 (2012).
- [57] R. V. Kutluyarov, V. K. Bagmanov, V. V. Antonov, A. K. Sultanov, and V. S. Lyubopytov, "Increase of nonlinear signal distortions due to linear mode coupling in space division multiplexed systems," in *2017 International Multi-Conference on Engineering, Computer and Information Sciences (SIBIRCON)*, 282-286 (2017).
- [58] J. E. Sharping, M. Fiorentino, P. Kumar, and R. S. Windeler, "Optical parametric oscillator based on four-wave mixing in microstructure fiber," *Optics Letters*, vol. **27**(19), 1675-1677 (2002).
- [59] Y. Q. Xu, K. F. Mak, and S. G. Murdoch, "Multiwatt level output powers from a tunable fiber optical parametric oscillator," *Optics Letters*, **36**(11), 1966-1968 (2011).
- [60] R. T. Murray, E. J. R. Kelleher, S. V. Popov, A. Mussot, A. Kudlinski, and J. R. Taylor, "Synchronously pumped photonic crystal fiber-based optical parametric oscillator," *Optics Letters*, vol. **37**(15), 3156-3158 (2012).
- [61] L. Jin, A. Martinez, and S. Yamashita, "Optimization of output power in a fiber optical parametric oscillator," *Optics Express*, **21**(19), 22617-22627 (2013).
- [62] B. H. Soffer and B. B. McFarland, "CONTINUOUSLY TUNABLE, NARROW-BAND ORGANIC DYE LASERS," *Applied Physics Letters*, **10**(10), 266-267, (1967).
- [63] J. A. Giordmaine and R. C. Miller, "Tunable Coherent Parametric Oscillation in LiNbO<sub>3</sub> at Optical Frequencies," *Physical Review Letters*, **14**(24), 973-976 (1965).

- [64] C. C. Wang and G. W. Racette, "MEASUREMENT OF PARAMETRIC GAIN ACCOMPANYING OPTICAL DIFFERENCE FREQUENCY GENERATION," *Applied Physics Letters*, **6**(8), 169-171 (1965).
- [65] R. Stolen, "Phase-matched-stimulated four-photon mixing in silica-fiber waveguides," *IEEE Journal of Quantum Electronics*, **11**(3), 100-103 (1975).
- [66] T. Lu, L. S. Kiani, and J. E. Sharping, "Polarization and Reflectivity Effects on Fiber Optical Parametric Oscillator Output Power," in *CLEO: 2013*, San Jose, California, Optical Society of America, in OSA Technical Digest, p. CTh3M.4 (2013).
- [67] B. Schaefer, E. Collett, R. Smyth, D. Barrett, and B. Fraher, "Measuring the Stokes polarization parameters," *American Journal of Physics*, **75**(2), 163-168 (2007).
- [68] Q. Lin and G. P. Agrawal, "Vector theory of four-wave mixing: polarization effects in fiber-optic parametric amplifiers," *Journal of the Optical Society of America B*, **21**(6), 1216-1224 (2004).
- [69] V. Gordienko, M. F. C. Stephens, A. E. El-Taher, and N. J. Doran, "Ultra-flat wideband single-pump Raman-enhanced parametric amplification," *Optics Express*, **25**(5), 4810-4818 (2017).
- [70] V. Ribeiro, A. Lorences-Riesgo, P. Andrekson, and M. Karlsson, "Noise in phase-(in)sensitive dual-core fiber parametric amplification," *Optics Express*, **26**(4), 4050-4059 (2018).
- [71] M. E. Marhic, P. A. Andrekson, P. Petropoulos, S. Radic, C. Peucheret, and M. Jazayerifar, "Fiber optical parametric amplifiers in optical communication systems," (in eng), *Laser & photonics reviews*, **9**(1), 50-74 (2015).
- [72] Z. M. L. Sandar Myint, Hla Myo Tun, "Performance Analysis of Single-Pumped And Dual-Pumped Parametric Optical Amplifier," *International Journal of Scientific & Technology Research*, **4**(6), p. 6 (2015).
- [73] M. K. Vitor Ribeiro, and Peter Andrekson, "Parametric amplification with a dual-core fiber," - *Optics Express J2 - Opt. Express*, **25**(6), 6234-6243 (2017).
- [74] Y. Yan and J. Toulouse, "Nonlinear inter-core coupling in triple-core photonic crystal fibers," *Optics Express*, **17**(22), 20272-20281 (2009).
- [75] H. Steffensen, J. R. Ott, K. Rottwitt, and C. J. McKinstrie, "Full and semi-analytic analyses of two-pump parametric amplification with pump depletion," *Optics Express*, **19**(7), 6648-6656, (2011).



- [76] F. Yaman, "Fiber-Optics Parametric Amplifiers: Their Advantages and Limitations," Doctor of Philosophy, The Institute of Optics, University of Rochester, 2006.
- [77] B. J. Smith, P. Mahou, O. Cohen, J. S. Lundeen, and I. A. Walmsley, "Photon pair generation in birefringent optical fibers," *Optics Express*, **17**(26), 23589-23602, (2009).
- [78] J. E. Antonio-Lopez, Z. S. Eznaveh, P. LiKamWa, A. Schülzgen, and R. Amezcua-Correa, "Multicore fiber sensor for high-temperature applications up to 1000°C," *Optics Letters*, **39**(15), 4309-4312 (2014).
- [79] P. M. Blanchard *et al.*, "Two-dimensional bend sensing with a single, multi-core optical fibre," *Smart Materials and Structures*, **9**(2), 132-140 (2000).
- [80] H. Martins, M. B. Marques, P. Jorge, C. M. B. Cordeiro, and O. Frazão, "Intensity curvature sensor based on photonic crystal fiber with three coupled cores," *Optics Communications*, **285**(24), 5128-5131 (2012).
- [81] F. Ignazio, M. Javier, S. Salvador, A. C. Pedro, and M. A. Jose, "Twisting compensation of optical multicore fiber shape sensors for flexible medical instruments," in *Proc.SPIE*, **11233** (2020).
- [82] F. Tan, Z. Liu, J. Tu, C. Yu, C. Lu, and H.-Y. Tam, "Torsion sensor based on inter-core mode coupling in seven-core fiber," *Optics Express*, **26**(16), 19835-19844 (2018).